NREL/TP-451-5355 • UC Category: 270 • DE93000097

New III-V Cell Design Approaches for Very High Efficiency

Annual Subcontract Report
1 August 1991 – 31 July 1992

NREL/TP--451-5355

DE93 000097

M. S. Lundstrom, M. R. Melloch,
G. B. Lush, M. P. Patkar, M. P. Young
Purdue University
West Lafayette, Indiana

NREL technical monitor: J. Benner

National Renewable Energy Laboratory
1617 Cole Boulevard
Golden, Colorado 80401-3393
Operated by Midwest Research Institute
for the U.S. Department of Energy
under Contract No. DE-AC02-83CH10093

Prepared under Subcontract No. XM-0-19142-1

April 1993

MASTER

This publication was reproduced from the best available camera-ready copy
submitted by the subcontractor and received no editorial review at NREL.

NOTICE

This report was prepared as an account of work sponsored by an agency of the United States government. Neither the United States government nor any agency thereof, nor any of their employees, makes any warranty, express or implied, or assumes any legal liability or responsibility for the accuracy, completeness, or usefulness of any information, apparatus, product, or process disclosed, or represents that its use would not infringe privately owned rights. Reference herein to any specific commercial product, process, or service by trade name, trademark, manufacturer, or otherwise does not necessarily constitute or imply its endorsement, recommendation, or favoring by the United States government or any agency thereof. The views and opinions of authors expressed herein do not necessarily state or reflect those of the United States government or any agency thereof.

Printed in the United States of America
Available from:
National Technical Information Service
U.S. Department of Commerce
5285 Port Royal Road
Springfield, VA 22161

Price: Microfiche A01
Printed Copy A06

Codes are used for pricing all publications. The code is determined by the number of pages in the publication. Information pertaining to the pricing codes can be found in the current issue of the following publications which are generally available in most libraries: *Energy Research Abstracts (ERA)*; *Government Reports Announcements* and Index (*GRA* and I); *Scientific and Technical Abstract Reports (STAR)*; and publication NTIS-PR-360 available from NTIS at the above address.

DISCLAIMER

PREFACE

To realize cost-effective solar cells with efficiencies exceeding 35% is an important objective of the national photovoltaics program. Cell efficiencies are progressing rapidly, but it seems unlikely that the present design approach will produce efficiencies very much above 30% under concentration. Multi-junction cells, both monolithic and mechanically-stacked, have already achieved efficiencies well above 30%, but substantial cost reductions are still required. The objective of our research is to examine new *design* approaches for achieving very high conversion efficiencies.

The research program consists of two thrusts with the first centering on exploring new thin-film approaches specifically designed for III-V semiconductors. By employing light trapping techniques to confine the incident photons as well as the photons emitted by radiative recombination, substantial efficiency gains may be possible. The thin-film approach is a promising route for achieving substantial performance improvements in the already high-efficiency, single-junction, III-V cell. The second thrust of our group's work involves exploring design approaches for achieving high conversion efficiencies without requiring extremely high-quality material. This work has applications to multiple-junction cells for which the selection of a component cell often involves a compromise between optimum bandgap and optimum material quality. It could also be a benefit in a manufacturing environment by making the cell's efficiency less dependent on material quality.

SUMMARY

Project Overview

Our group's past work on basic studies of GaAs solar cells helped us to understand the losses that dominate in present-day cells, and it serves as the foundation for the device design research now underway. The unconventional design approaches we are exploring also require new basic research on radiative recombination, photon recycling, and AlGaAs loss mechanisms. The research program is, therefore, balanced to increase our basic understanding of III-V cell device physics and to explore the potential of unconventional cell designs.

To enhance the already high efficiency of GaAs cells, we are exploring new, thin-film approaches designed to trap incident light and to take advantage of so-called photon recycling effects. It has long been realized that radiative recombination is not necessarily a loss mechanism; *if* the cell is thick enough and *if* the emitted photons are confined within the cell. By adopting a thin-film cell approach, designed to optically confine the photons emitted by radiative recombination within the cell, lifetimes could be enhanced by an order of magnitude — or even more. Thin-film cells might also benefit from conventional, incident light trapping, which is used with great success for silicon cells.

The second research thrust centers on developing cell designs to maximize conversion efficiencies without requiring extremely high material quality. By using MBE film growth, we plan to investigate a variety of cell design options. A sound understanding of recombination losses in AlGaAs cells is a prerequisite for selecting an appropriate design, so basic work to quantify losses in AlGaAs cells is an important part of the research program.

Scientific and Technical Activities: 1991 - 1992

During the past year, we concentrated on basic studies and made progress in understanding radiative recombination and photon recycling in GaAs. At the same time, we have developed some proficiency at producing thin-film structures and devices. Finally, our cell fabrication capabilities have been improved.

For the basic studies of radiative recombination, optical absorption, and photon recycling, the key results of last year's work are:

1) *Minority Carrier Recombination in n-GaAs*
We completed a comprehensive study of recombination lifetimes in n-GaAs doped from ~ $10^{17}/\text{cm}^3$ to $10^{18}/\text{cm}^3$ and found that τ_p always exceeded the expected radiative lifetime. We tentatively attributed these results to photon recycling.

2) *Minority Carrier Recombination in n-GaAs Membranes*
To enhance photon recycling, we removed the substrates from the double heterostructures by chemically etching a hole through the substrate. We found enhancements in the lifetimes of 3-10 times (depending on the thickness of the double heterostructure) which we attribute to improved optical confinements of the emitted photons. For $n_o \sim 10^{17}/cm^3$, we measured a lifetime greater than 1 μsec, which is unusually long for moderately-doped n-type GaAs.

3) *Optical Absorption in n-GaAs*
We completed a series of measurements of $\alpha(h\nu)$ for n-GaAs doped from $10^{17}/cm^3$ to mid-$10^{18}/cm^3$. The results are qualitatively similar to those reported by Casey in the 1970's, but we found important quantitative differences.

4) *Numerical Modeling of Photon Recycling*
Working with Professor Jeff Gray and his student, Steve Durbin, we developed a preliminary numerical solar cell model which treats photon recycling. We find that the model generally accounts for our experimental observations.

5) *Computation of the B-Coefficient for n-GaAs*
The radiative lifetime is given by $\tau_r = 1/Bn_o$, where the B coefficient describes the radiative transition rate. Previous estimates of B have varied by more than one order of magnitude. Using our measured results for minority carrier lifetimes and for the optical absorption and photoluminescence spectra, we evaluated B for n-type GaAs. Over a range of doping from 10^{17} to mid-10^{18} cm^{-3}, we find that B varies from greater than 3 to less than 2×10^{-10} cm^3/s. These self-consistent results should prove useful in solar cell design.

More details about these basic studies can be found in the body of the report. In addition to these basic studies, we have also worked on thin-film cell fabrication. Mahesh Patkar has became proficient at the epitaxial lift-off (ELO) technique. For example, he has successfully lifted off a double heterostructure, mounted it on a glass slide, and measured a minority carrier lifetime of 1 μsec, which is thirty times the radiative limit at this doping density of $\sim 10^{17}/cm^3$. We have also found that the I-V characteristics of p-n junctions are not degraded after lift-off.

Work on thrust two of the project also continued. During the course of the past two year's work we have fabricated a number of $Al_{0.2}Ga_{0.8}As$ and $Al_{0.4}Ga_{0.7}As$ cells. The internal quantum efficiencies of the cells proved to be low, which indicates that the lifetimes are low. This year we also fabricated a graded gap cell in an attempt to improve the collection efficiency. Surprisingly, we found that the internal quantum efficiency remained low. The cause for this unexpected result has still not been ascertained.

Overview of the Report

Our group's work on basic studies is now nearly complete; next year's efforts will be devoted to exploring novel device structures. This year's report is a summary of the findings thast resulted from the past two year's work on optical absorption and recombination in GaAs. The chapters were taken from the Ph.D thesis of Dr. Gregory B. Lush, which was completed in July 1992. Chapter 1 is an introduction to recombination in semiconductors and defines some important terms and concepts. Chapter 2 describes photoluminescence decay measurements of minority carrier recombination in n-type GaAs. The films for this study were grown by Hugh MacMillan at the Varian Research Center, and the measurements were performed in Richard Ahrenkiel's laboratory at NREL. In Chapter 3, we present measurments of the doping-dependent optical absorption coefficient for n-type GaAs. The possibilities for engineering device structures to exploit photon recycling to enhance minority carrier lifetimes are demonstrated in Chapter 4, and we examine the relation between optical absorption and recombination and estimate the B-coefficient in Chapter 5. The report concludes with a brief summary and recommendations for future work.

TABLE OF CONTENTS

CHAPTER 1

RECOMBINATION IN SEMICONDUCTORS

1.1 Introduction

Recombination of electron-hole pairs is one of the most fundamental mechanisms in semiconductors. Knowledge of the dominant recombination mechanisms and their rate constants is vital to the understanding and modeling of semiconductor devices. In direct-gap semiconductors such as gallium arsenide (GaAs), radiative recombination can dominate. Because absorption and emission of photons are so intimately related, one must fully understand absorption in order to completely understand the emissive properties of GaAs optical devices such as light emitting diodes, lasers, and solar cells. This work is the account of a comprehensive study of recombination and absorption in n-type GaAs. Reported herein are the observed minority carrier lifetimes (and the mechanisms responsible) and the absorption constants of moderately doped n-GaAs with electron concentrations of certain interest to device physicists. These results should fill what has been a void of data for minority hole recombination in n-GaAs, and eliminate any confusion regarding the relationship between absorption and emission of light near the band edge for GaAs in general.

1.2 Recombination

Mechanisms of recombination can be divided into two categories:

1) recombination intrinsic to the semiconductor (radiative and Auger recombination) which are independent of crystal growth methods but are strongly dependent on doping concentration,

2) recombination through defect levels, or Shockley-Read-Hall (SRH) recombination [1, 2], which is strongly dependent on crystal growth methods and growth conditions. SRH recombination has no explicit doping dependence, but in practice the concentration of defect levels increases with increasing doping concentration.

Recombination in an n-type semiconductor can be written as [3]

$$R = \frac{pn - n_i^2}{\tau_n(p + p_1) + \tau_p(n + n_1)} + B(pn - n_i^2) + C_n n(pn - n_i^2), \qquad (1.1)$$

where the three terms describe the SRH, radiative, and two-electron Auger recombination rates, respectively. The SRH hole and electron lifetimes are τ_p and τ_n, respectively, B is the probability coefficient for a radiative transition, and C_n is the probability coefficient for an Auger transition involving two electrons. All other parameters have their familiar definitions. It is instructive to rewrite Eq. (1.1) for conditions of low injection.

$$R = \frac{\Delta p}{\tau_{eff}} = \frac{\Delta p}{\tau_{SRH}} + \frac{\Delta p}{\tau_r} + \frac{\Delta p}{\tau_{Auger}}, \qquad (1.2)$$

where τ_{eff} is the effective lifetime from all mechanisms, Δp is the excess hole density, and

$$\tau_{SRH} = \tau_p \qquad \tau_r = \frac{1}{B(N_D - N_A)} \qquad \tau_{Auger} = \frac{1}{C_n(N_D - N_A)^2} \qquad (1.3)$$

represent the lifetimes for the SRH, radiative, and Auger mechanisms respectively. Equation (1.3) allows a clearer picture of the expected doping dependence of the respective lifetimes. Though there is no explicit doping dependence for SRH recombination, previous work in GaAs cited below and also work in silicon indicate that SRH lifetimes decrease significantly with increasing impurity concentration. This is important because if SRH recombination dominates in a semiconductor, as was the case in previous studies of n-GaAs, it is much more difficult to quantify the contribution from intrinsic mechanisms. This has left an incomplete understanding of radiative recombination which dominates the high-quality GaAs crystals grown by modern techniques.

1.3 Theory of Radiative Recombination

1.3.1 Introduction

Because radiative recombination is so important in the high-quality material studied in this work, it is helpful to briefly discuss radiative transitions and the relationship between absorption of photons and radiative

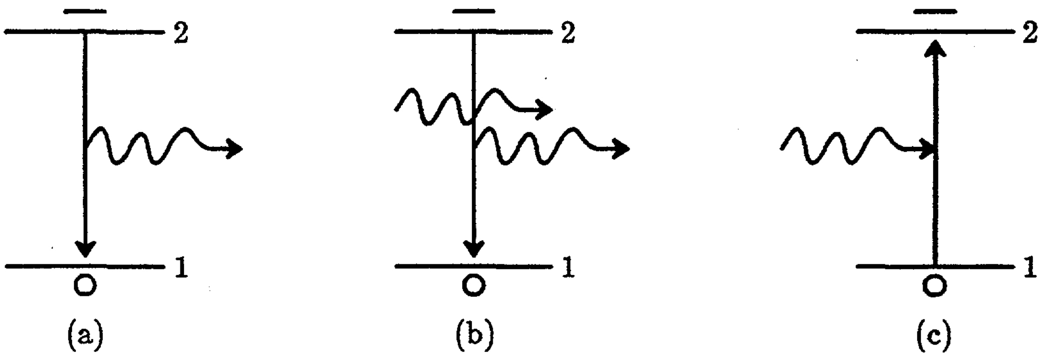

Figure 1.1 Diagram of the three possible radiative band-to-band transitions: (a) spontaneous emission, (b) stimulated emission, and (c) stimulated absorption.

recombination. In this section we quantify this relationship by first using a two-level system to illustrate the law of detailed balance in equilibrium. By extending this to a multi-level system, an equation for the equilibrium B-coefficient is derived. Finally, it is shown that the B-coefficient does not change under low injection conditions proving that it is valid to use B in Eqs. 1.1 and 1.3.

Figure 1.1 depicts the three possible radiative transitions in a simple two-level system:

(a) spontaneous emission from 2 to 1 (with transition rate defined as R_{spon21}),

(b) stimulated emission from 2 to 1 (R_{stim21}),

(c) stimulated absorption from 1 to 2 (R_{stim12}).

These transition rates are described by [4]

$$R_{spon21} = A_{21} f_2 (1-f_1), \tag{1.4a}$$

$$R_{stim21} = B_{21} f_2 (1-f_1) \gamma_{bb}(E_{21}), \tag{1.4b}$$

$$R_{stim12} = B_{12} f_1 (1-f_2) \gamma_{bb}(E_{21}), \tag{1.4c}$$

where $f_{1(2)}$ is the Fermi-Dirac occupation probability function for electrons in state 1 (state 2), and $\gamma_{bb}(E_{21})$ is the density of photons with energy E_{21} in the black-body spectrum. In weakly dispersive media, $\gamma_{bb}(E_{21})$ is written as [4-6]

$$\gamma_{bb}(E_{21}) = \frac{8\pi n^3 E^2}{h^3 c^3} \frac{1}{e^{E_{21}/kT} - 1}. \tag{1.5}$$

1.3.2 Consequences of Detailed Balance

The law of detailed balance says that in equilibrium the rate of transitions from 1 to 2 is equal to the rate of transitions from 2 to 1; combining Eqs. (1.4), we obtain

$$B_{12} f_1 (1-f_2) \gamma_{bb}(E_{21}) = B_{21} f_2 (1-f_1) \gamma_{bb}(E_{21}) + A_{21} f_2 (1-f_1). \tag{1.6}$$

Equation (1.6) is simplified to

$$B_{12} \gamma_{bb}(E_{21}) e^{\frac{E_{21}-E_F}{kT}} = B_{21} \gamma_{bb}(E_{21}) e^{-E_F/kT} + A_{21}\, e^{-E_F/kT}, \tag{1.7}$$

where E_F is the Fermi level, k is Boltzmann's constant, and T is the absolute temperature. Solving for $\gamma_{bb}(E_{21})$ in Eq. 1.7,

$$\gamma_{bb}(E_{21}) = \frac{A_{21}}{B_{21}} \frac{1}{(B_{12}/B_{21}) e^{E_{21}/kT} - 1}. \tag{1.8}$$

Comparing Eqs. (1.8) and (1.5), we find

$$B_{12} = B_{21} \tag{1.9}$$

$$A_{21} = \left[\frac{8\pi n^3 E_{21}^2}{h^3 c^3}\right] B_{12} \tag{1.10}$$

Equation (1.10) shows the direct relationship between absorption and emission of photons, which manifests itself on a macroscopic basis as a relationship between the band-to-band absorption coefficient and the radiative lifetime.

Absorption is described macroscopically by the absorption coefficient, α. The net absorption rate, $R_{stim12} - R_{stim21}$ is simply equal to the photon flux, Φ, times α. Because $B_{12} = B_{21}$,

$$R_{net12} = B_{12}\,[f_1 - f_2]\gamma_{bb}(E_{21}) = \Phi\alpha. \tag{1.11}$$

The photon flux is simply $\Phi = \gamma_{bb}(E_{21})v_g(E_{21})$ where $v_g(E_{21})$, the photon group velocity, is the speed of light in the material. Combining Eqs. (1.10) and (1.11), we can write

$$A_{21}\left[\frac{h^3 c^3}{8\pi n^3 E_{21}^2}\right][f_1 - f_2]\gamma_{bb}(E_{21}) = \alpha(E_{21})\gamma_{bb}(E_{21})v_g(E_{21}), \tag{1.12}$$

which reduces to

$$A_{21} = \alpha(E_{21})\frac{1}{(f_1 - f_2)}\left[\frac{8\pi n^3 E_{21}^2}{h^3 c^3}\right] v_g(E_{21}). \tag{1.13}$$

Equation (1.13) relates the probability of spontaneous recombination to α, which can be measured experimentally. Inserting Eq. (1.13) into the spontaneous emission rate given by Eq. (1.4a) gives

$$R_{spon21} = A_{21} f_2 (1 - f_1) = \alpha(E_{21})\gamma_{bb}(E_{21})v_g(E_{21}). \tag{1.14}$$

This same relationship was deduced by van Roosbroeck and Shockley [5] using similar detailed balance arguments. To generalize to a continuous set of states such as for the band structure of a semiconductor, Eq. (1.14) becomes

$$R_{spon} = A^o_{cv} f^o_c g^o_c (1 - f^o_v) g^o_v = \alpha(E_{cv}) \gamma_{bb}(E_{cv}) v_g(E_{cv}), \tag{1.15}$$

where g^o_v (g^o_c) is the equilibrium density of states for the valence (conduction) band. Integrating over all energies, we obtain

$$R^o_{spon} = \langle A^o \rangle p_o n_o = \int_0^\infty \gamma_{bb}(E) \alpha(E) v_g(E) dE, \tag{1.16}$$

where $\langle A^o \rangle$ is now the average value of A^o_{cv}, weighted according to the densities of electrons and holes in states separated by energy E_{cv}, and

$$\langle A^o \rangle = \frac{\int_o^\infty A^o_{cv} f^o_c g^o_c (1 - f^o_v) g^o_v dE}{p_o n_o}. \tag{1.17}$$

1.3.3 The Radiative Lifetime

The total spontaneous recombination rate is therefore a rate constant times the density of holes times the density of electrons. Does this hold out of equilibrium so that $R_{spon} = \langle A \rangle pn$, where $\langle A \rangle$ is the non-equilibrium representation of $\langle A^o \rangle$? In other words, is $\langle A^o \rangle = \langle A \rangle$? Inspection of the left hand side of Eq. (1.15) shows that $\langle A^o \rangle = \langle A \rangle$ if $A^o_{cv} = A_{cv}$ and if the weighting function, $g_v g_c f_c (1 - f_v)$, does not change its energy dependence out of equilibrium. Assuming the densities of states, g_v and g_c, do not change under low excitation, we need only consider the Fermi functions. Under low injection in an n-type semiconductor,

$$f_c(1 - f_v) = \frac{1}{1 + e^{E_c - E_f/kT}} \times e^{-(F_h - E_v)/kT} \tag{1.18}$$

$$f_c(1 - f_v) = \frac{1}{1 + e^{E_c - E_f/kT}} \times e^{-(E_f + F_h - E_f - E_v)/kT} \tag{1.19}$$

$$f_c(1 - f_v) = \frac{1}{1 + e^{E_c - E_f/kT}} \times e^{-(E_f - E_v)/kT} \times e^{-(F_h - E_f)/kT} \tag{1.20}$$

$$f_c(1 - f_v) = f_c^o(1 - f_v^o) \times \frac{p}{p_o}. \tag{1.21}$$

Thus <A> = <A°>, it is valid to write R_{spon} = <A>pn out of equilibrium, and <A> can be computed from Eq. (1.16). The radiative lifetime is found from $R_{spon} = \Delta p/\tau_r$ so that

$$\frac{1}{\tau_r} = \frac{1}{p_o}\int_0^\infty \gamma_{bb}(E)\alpha(E)v_g(E)dE. \tag{1.22}$$

1.3.4 Photoluminescence Spectra

The validity of using Eq. (1.22) to compute τ_r can be verified by observing PL spectra, the energy dependence of R_{spon}. Equation (1.15) gives the expected energy dependence of R_{spon}. Chapter 3 discusses α(E), and Chapter 5 shows that Eq. (1.15) accurately models the PL spectra in the double heterostructures (DH's) used for this study. This consistency validates both the α(E) data and the approach of computing <A> from equilibrium relationships. (The rate of radiative recombination is typically written as R_{spon} = Bpn, as in Eqs. (1.1) and (1.3), so B will be used instead of <A> through the rest of this document.)

1.4 Previous Work in N-type GaAs

Early studies of recombination and absorption in n-type GaAs were done on melt-grown material [7-11] and on material grown by liquid phase epitaxy (LPE) [12-14], and were made using a wide variety of techniques. Casey *et al.* used short-circuit photo-current measurements [12], Puhlmann *et al.* measured the electron beam induced current [13], and Hwang observed the PL decay of melt-grown, unpassivated wafers [8]. All these yield diffusion length rather than lifetime, and the first two do not distinguish between bulk and interface recombination. Ahrenkiel *et al.* observed the PL decay of DH's [15]. Because DH's have low interface recombination velocities, allow one to separate bulk and interface recombination, and measure the lifetime directly, eliminating diffusion under most conditions, observing the PL decay of DH's has become

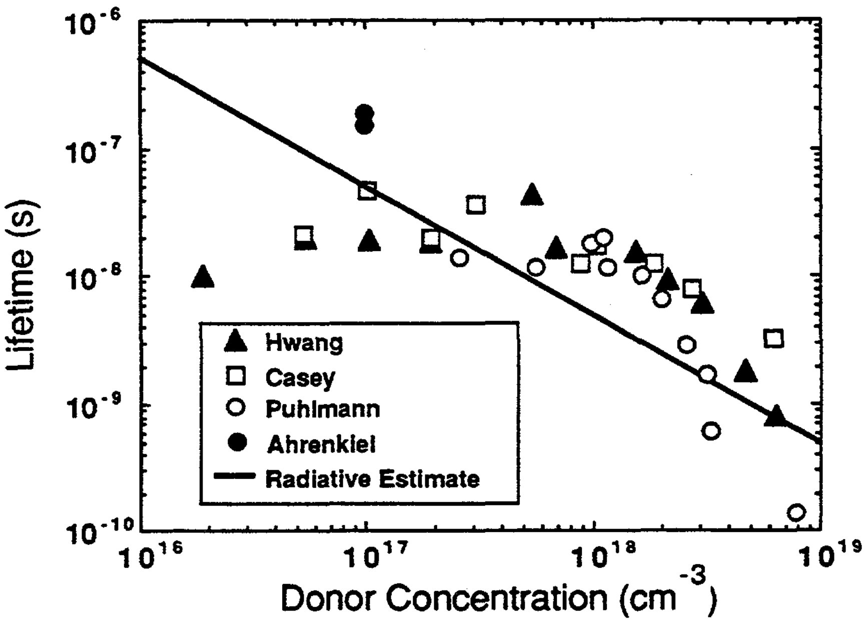

Figure 1.2 Observed lifetime versus electron concentration from previous work.

the most popular method of deducing the lifetimes of materials [15-20]. Figure 1.2 shows a plot of observed lifetime versus electron concentration for these studies. The solid line is the supposed radiative limit assuming $B = 2.0 \times 10^{-10}$ cm^3/s [20, 21] and using Eq. (1.3) above. One can see that the lifetime seems to "saturate" around 20 nanoseconds for low electron concentrations; this is believed to be caused by background impurities incorporated during growth [8]. Beginning near $n_o = 10^{18}$ cm^{-3}, the lifetime then decreases approximately linearly with increasing electron concentration before it drops more rapidly at the highest concentrations. The initial decrease in lifetime occurs as radiative recombination becomes competitive with SRH. At the highest electron concentrations it was found that SRH begins to dominate once again; no evidence for Auger recombination has been found in n-type GaAs [9, 16]. The predominance of SRH recombination in these films has made estimation of the intrinsic recombination parameters difficult as deduced values of the radiative lifetime vary by an order of magnitude [9,14]. The intrinsic recombination mechanisms are expected to be more important in the higher-quality material grown by molecular beam epitaxy (MBE) or by metalorganic chemical vapor deposition (MOCVD). Understanding intrinsic mechanisms is therefore even more important today. Finally, note in Fig 1.2 that around $n_o \simeq 10^{18}$ cm^{-3} the observed lifetimes are longer than the supposed radiative limit using the most commonly employed value of B. This means that either the choice of B was inappropriate or photon recycling effects were being observed.

Photon recycling is the reabsorption of photons emitted during a radiative recombination event, which creates a new electron-hole pair [15,20,22-24]. Photon recycling increases the observed minority carrier lifetime of GaAs when radiative recombination is important because a recombination event is no longer necessarily a loss. There have been many models proposed to describe photon recycling, especially in DH's, but no two models have produced the same results. Recycling models are strongly dependent on knowledge of the near band edge absorption coefficient, $\alpha(h\nu)$, and one problem with previous recycling models is that they have all used the $\alpha(h\nu)$ data of Casey *et al.* [10] Casey and Stern [25] expressed concern about that data because it was not consistent with previous measurements [7,11], may have been influenced by precipitates, and because their theoretical model could not describe that data. Thus, there is a need to measure $\alpha(h\nu)$ near the band edge of n-GaAs in order to fully understand photon recycling and therefore understand completely recombination in n-type GaAs.

1.5 Overview of the Thesis

This work is the account of a comprehensive study of recombination and absorption in high-quality, n-type GaAs grown by MOCVD. Chapter 2 reviews the observed decay constants or device lifetimes of the DH's, and the first evidences of photon recycling effects are noted. The techniques used to grow the material by MOCVD for a large matrix of device thicknesses and electron concentrations are also discussed. Chapter 3 shows the near band-edge α deduced from transmission measurements on the DH's. Chapter 4 conclusively demonstrates the enormous effect of photon recycling in GaAs as a nearly ten-fold increase in effective lifetime was observed by simply removing the supporting substrate. Optical absorption and radiative recombination are related in Chapter 5 it is shown that PL spectra can be modeled by using Eq. (1.15) and the deduced values of α. Equation (1.17) is then used to compute the B-coefficient, and this compares favorably with calculations of B from lifetime measurements after accounting for photon recycling. Chapter 6 summarizes the findings, reviews their significance for optical and electronic devices, and proposes areas of future work.

CHAPTER 2

PHOTOLUMINESCENCE DECAY OF N-TYPE GaAs DOUBLE HETEROSTRUCTURES

2.1 Introduction

An understanding of how the minority carrier lifetime varies with electron concentration is essential for designing bipolar devices such as solar cells, transistors, and lasers. In particular, it is important to understand how the radiative, Shockley-Read-Hall (SRH), and Auger lifetimes vary with electron concentration. Because the available data for n-GaAs is strongly influenced by SRH recombination, intrinsic processes such as radiative and Auger recombination, are difficult to study. For instance, both Garbuzov [14] and Hwang [9] deduced the radiative lifetimes in their samples, but their estimates differ by more than one order of magnitude. Also, theoretical estimates of the Auger coefficients vary widely [26-28], and little data is available to test these estimates [13, 14, 29]. Neither Hwang nor Garbuzov found evidence of Auger recombination in n-type GaAs, but Puhlmann deduced an unexpectedly high Auger coefficient. It seems clear that the understanding of intrinsic recombination processes in n-type GaAs is unsatisfactory. Comprehensive studies using high-quality epitaxial material grown by modern epitaxial techniques should permit the estimation of intrinsic recombination processes without being dominated by defect-related, SRH recombination.

This chapter is the first phase of the comprehensive study of the concentration-dependent minority carrier lifetime in n-type AlGaAs/GaAs/AlGaAs double heterostructures (DH's) grown by metalorganic chemical vapor deposition (MOCVD). The selenium-doped films were n-type with carrier concentrations from 1.3×10^{17} cm^{-3} to 3.8×10^{18} cm^{-3}. For each electron density, films with five different active layer thicknesses were grown. Unlike the earlier work cited above, no evidence for SRH recombination is found for $n_o < 10^{18}$ cm^{-3}. For $n_o > 10^{18}$ cm^{-3}, there is evidence of SRH recombination, but even for the most heavily doped films, radiative recombination is important. These comprehensive results for 30 different films with various electron densities and thicknesses provide data that is directly useful for device design, and they are the first step in developing a detailed understanding of minority carrier recombination in n-type GaAs.

The chapter is organized as follows. Section 2.2 discusses the procedures used to analyze the photoluminescence (PL) decay characteristics of the DH's. MOCVD growth techniques are described in Sec. 2.3, and the specific DH's grown for the study are shown. The experimental apparatus and techniques for measuring the time-resolved photoluminescence decay are also described in Sec. 2.3. Section 2.4 presents the measured results for both low- and high-intensity laser excitation. Evidence for photon recycling in these films is discussed in Sec. 2.4, and further evidence is given in Sec. 2.5. Finally, in Sec. 2.6 the results and conclusions are summarized and lingering issues are identified.

2.2 Procedure for Double Heterostructure Analysis

Observing the time-resolved PL decay of DH's is a well-developed technique for examining interface and bulk recombination [15,18,19]. The DH is especially valuable as a tool for characterizing material quality because its PL decay can be made to be independent of diffusion. If $0 < \mathrm{Sw}/\mathrm{D} < 1$, one can express the low-injection decay constant of a DH as [30-32]

$$\frac{1}{\tau_{\mathrm{DH}}} = \frac{1}{\tau_{\mathrm{bulk}}} + \frac{2\mathrm{S}}{\mathrm{w}}, \tag{2.1}$$

where S is the average of the front and back interface recombination velocities, w is the active layer thickness for the DH, D is the minority carrier diffusivity, and τ_{bulk} is made up of contributions from the radiative, SRH, and Auger mechanisms. Equation (2.1) clearly shows contributions to τ_{DH} from both the interfaces and from the combination of the various bulk mechanisms.

To separate interface and bulk recombination, the decay constants of several DH's with identical electron densities but varying thicknesses are measured, and a plot of $1/\tau_{\mathrm{DH}}$ vs. $2/\mathrm{w}$ is constructed [18,33]. According to Eq. (2.1), the intercept of this line is $1/\tau_{\mathrm{bulk}}$ and the slope is the average of $\mathrm{S_f}$ and $\mathrm{S_b}$, the front and back interface recombination velocities, respectively. Such a plot, using the data reported by Nelson [31] for p-type GaAs with a hole concentration of $\mathrm{p_o} = 5.0 \times 10^{15}\ \mathrm{cm}^{-3}$, is shown in Fig. 2.1. Despite the scatter in their data, one can clearly deduce a slope and an intercept. The data presented in this chapter show much less scatter, and, interestingly, all plots of $1/\tau_{\mathrm{DH}}$ vs. $2/\mathrm{w}$ are decidedly nonlinear. For such data, it is not immediately clear how to deduce the bulk lifetime or the interface recombination velocity.

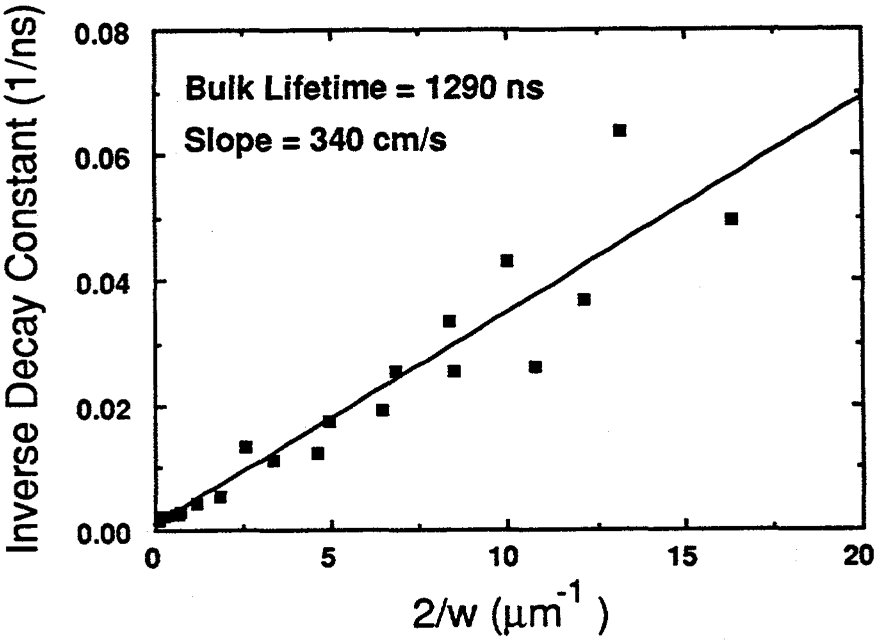

Figure 2.1 Inverse photoluminescence decay rate, $1/\tau_{DH}$ vs. $2/w$ for the p-type data with $p_o = 5.0 \times 10^{15}$ cm^{-3} reported by Nelson [30].

The nonlinearity of $1/\tau_{DH}$ vs. $2/w$ implies that either S or τ_{bulk} depends on the active layer thickness of the DH. However, the values of S deduced for these samples are too small to account for the changes observed in τ_{DH} versus DH thickness. Wolford *et al.* also observed nonlinearity in their plots of $1/\tau_{DH}$ vs. $1/w$, but they attributed it to a change in the bulk lifetime due to modulation doping in their P-n-P double heterojunctions with thin n-active layers [18]. Since these samples are isotype N-n-N DH's, this explanation does not apply.

A thickness dependent bulk lifetime caused by photon recycling could also explain the nonlinear $1/\tau_{DH}$ vs. $2/w$ characteristic. Photon recycling, the reabsorption of photons emitted during radiative recombination events, increases the observed minority carrier lifetime when radiative recombination is important [15, 20, 22, 23]. When including photon recycling, the bulk lifetime is expressed as

$$\frac{1}{\tau_{\text{bulk}}} = \frac{1}{\phi_r \tau_r} + \frac{1}{\tau_{\text{SRH}}} + \frac{1}{\tau_{\text{Auger}}}, \tag{2.2}$$

where ϕ_r, Asbeck's recycling cofactor, is the inverse of the probability that an isotropically emitted photon escapes from the active layer of the DH [22], and the lifetimes have their usual meanings. DH's with thick active layers will exhibit longer lifetimes because the emitted photons are more likely to be reabsorbed before escaping through the interfaces. Because τ_{bulk} increases with w, the plot of $1/\tau_{\text{DH}}$ vs. 2/w is nonlinear, so τ_{bulk} and S cannot be determined from its slope and intercept. An upper limit for S can, however, be estimated from the slope at large 2/w, and, as explained in Sec. 2.4, the importance of non-radiative recombination can be gauged from a plot of τ_{DH} vs. w, and from the intensity dependence of the decay constant.

Table 2.1 Targeted thicknesses and measured electron densities for each of the 30 double heterostructures used for this study.

Double Heterostructure Parameters					
n_o (cm^{-3})	Targeted Thicknesses (μm)				
1.3×10^{17}	0.25	1.25	2.5	5.0	10.
3.7×10^{17}	0.25	1.25	2.5	5.0	10.
1.0×10^{18}	0.5	1.0	2.0	4.0	8.
2.2×10^{18}	0.25	1.25	2.5	5.0	10.
2.4×10^{18}	0.25	0.5	1.25	2.5	10.
3.8×10^{18}	0.25	0.5	1.25	2.5	10.

2.3 Film Growth Methods and Measurement Techniques

The double heterostructures for these studies were grown at 740 ° C under atmospheric pressure by MOCVD in a horizontal reactor at the Varian Research Center. The material quality produced by this reactor has been consistently high, as evidenced by production of record efficiency solar cells [34]. Film growth took place on Zinc-doped, horizontal-Bridgman substrates, which were heated by radio frequency induction. The susceptor was molybdenum, coated with GaAs. The growth rate was maintained at six microns per hour, except for the films with $n_o = 2.4 \times 10^{18}$ cm^{-3}, for which the growth rate was four microns per hour. The doping agent was hydrogen selenide (from Scott Specialty Gases) diluted to 55 p.p.m. with hydrogen, and the sources were trimethyl aluminum, trimethyl gallium, and 100% Arsine. The V/III ratio was maintained at 30, with the exception of the films with $n_o = 2.4 \times 10^{18}$ cm^{-3}, for which the V/III ratio was 45. Hydrogen was purified by diffusion through palladium to provide a background flow rate of 12 liters/min.

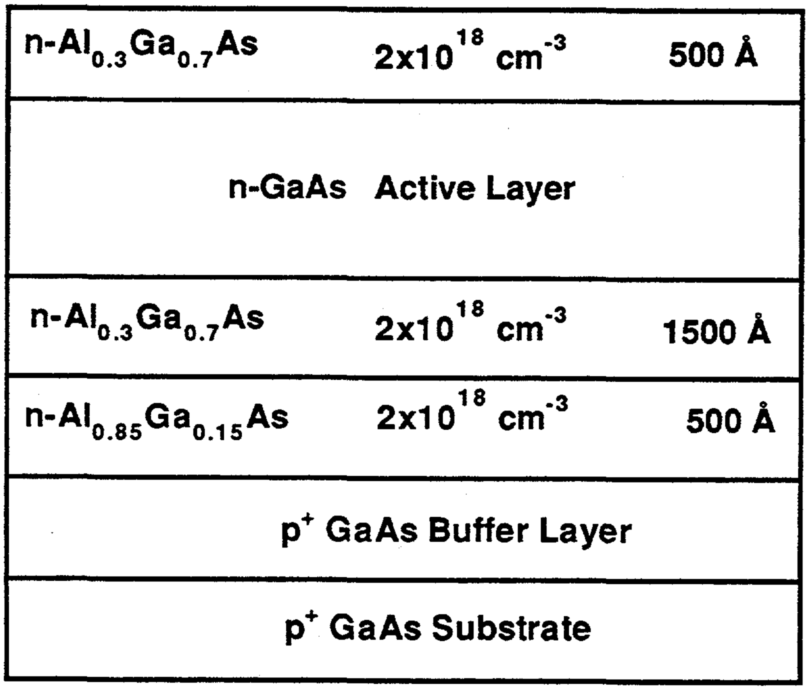

Figure 2.2 The structure of the double heterostructure samples used for the photoluminescence decay studies.

The basic structure of the DH's is shown in Fig. 2.2, and Table 2.1 lists the specific DH's grown for this study. All electron concentrations were measured by the van der Pauw technique. The $Al_{0.3}Ga_{0.7}As$ layers provide passivation and carrier confinement. The back two AlGaAs layers serve these purposes and serve as etch stop or etch release layers as well [35, 36]. (All results presented in this chapter are for DH's attached to the GaAs substrate; the etch stop/release layers permitted the studies of thin-film DH's which are separated from the substrate, discussed in Chapter 4.)

Photoluminescence decay was observed by the time-correlated, single photon counting technique described previously [37,38]. The exciting source was a Spectra Physics 375B cavity-dumped dye laser pumped by a frequency-doubled, Spectra Physics 3400 Nd^{3+}:YAG laser. Using Rhodamine 6G dye, pulses with a 10 ps full width at half maximum (FWHM) tuned to 600 nm wavelength were produced. The diameter of the unfocused beam was $\simeq 0.75$ cm, and when focused, the beam diameter was $\simeq 0.05$ cm. The laser repetition rate was 800 kHz. To examine intensity-dependent effects, a continuous gradient neutral density filter was used to vary the average laser power from a maximum of 40 mW to less than 0.1 mW. The corresponding energy per pulse varied from 50 to 0.1 nanojoules, respectively.

The emitted luminescence was collected in a backscattering geometry and focused on the slits of a 0.22 m scanning double monochrometer tuned to 870 nm, the peak of GaAs band edge emission. The resolution of the monochromator was 3.6 nm/mm, and the slit width was varied from 50 to 400 μm, according to the intensity of the luminescence observed. Single-photon detection is by an S1 photomultiplier tube with a 300 ps transit-time dispersion. The single-photon induced voltage pulses are amplified and fed to a multi-channel pulse height analyzer.

For an active layer thickness of 10 μm, an excitation wavelength of 600 nm, and a repetition rate of 800 kHz, the average injected electron-hole concentration is $\simeq 6\times10^{14}$ cm^{-3} when using a 20 mW, average power, unfocused beam. When the beam is focused to 0.05 cm, the average injected carrier concentration increases to over 10^{17} cm^{-3}. For a 1 μm thick active layer, the 20 mW focused beam produces an average injected carrier density of greater than 10^{18} cm^{-3}. For thin samples, some of the incident light is not absorbed in the DH, so to estimate the injection level, published data for the absorption coefficient is used [39].

2.4 Results

Table 2.2 lists the low intensity decay constants and their uncertainties for each of the films examined. Uncertainty in the decay constant is a result of noise in the PL decay data or, in a few cases, occurs because the PL decay was slightly non-exponential. Also listed is the expected low injection radiative lifetime at each electron concentration, obtained from [20, 21]

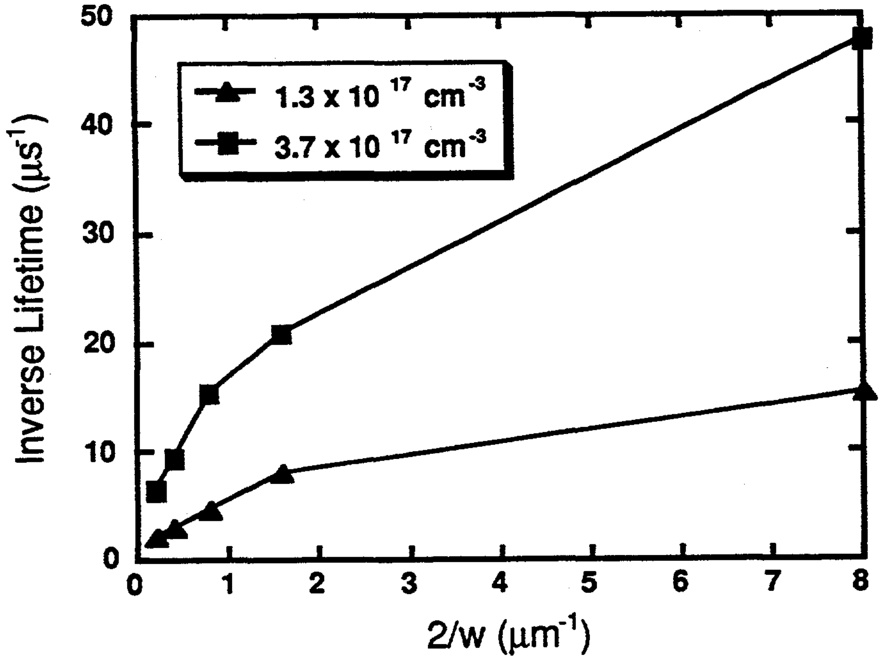

Figure 2.3 The inverse decay rate versus 2/w for the DH samples with $n_o = 1.3$ and 3.7×10^{17} cm^{-3}. The curvature is evidence for photon recycling.

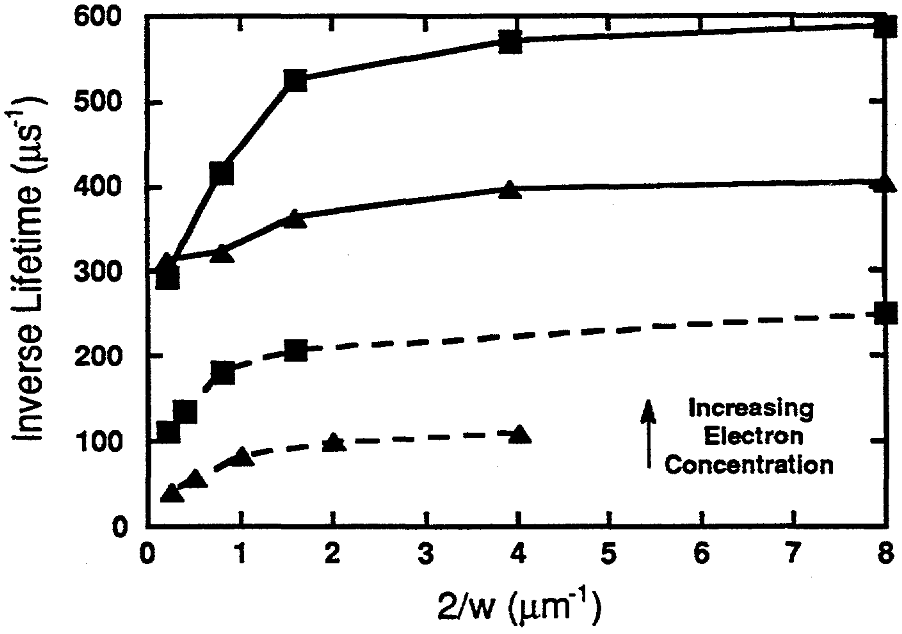

Figure 2.4 The inverse decay rate versus 2/w for the DH samples with $n_o \geq 1.0 \times 10^{18}$ cm^{-3}. The curvature is evidence for photon recycling.

Table 2.2 Measured room temperature decay constants and their uncertainties for each of the DH samples. In each case, the values reported are those at low laser intensity. The targeted thicknesses are given in brackets for clarity. Shown in the last column are the lifetimes expected theoretically by Eq. (2.3).

n_o (cm^{-3})	[Targeted DH Thicknesses (μm)] Measured DH Decay Constants (nsec)					$1/Bn_o$ (nsec)
1.3×10^{17}	[0.25] 65+−5	[1.25] 145+−5	[2.5] 210+−5	[5.0] 330+−10	[10.] 465+−5	38.5
3.7×10^{17}	[0.25] 21+−2	[1.25] 48+−2	[2.5] 65+−3	[5.0] 106+−2	[10.] 154+−4	13.5
1.0×10^{18}	[0.5] 9+−2	[1.0] 10+−1	[2.0] 12+−0.5	[4.0] 17.5+−1	[8.] 24+−2	5.0
2.2×10^{18}	[0.25] 4+−0.5	[1.25] 4.8+−0.5	[2.5] 5.5+−0.5	[5.0] 7.2+−0.2	[10.] 8.8+−0.2	2.3
2.4×10^{18}	[0.25] 2.48+−0.1	[0.5] 2.52+−0.1	[1.25] 2.75+−0.5	[2.5] 3.1+−0.1	[10.] 3.2+−0.1	2.1
3.8×10^{18}	[0.25] 1.7+−0.2	[0.5] 1.75+−0.25	[1.25] 1.9+−0.1	[2.5] 2.4+−0.2	[10.] 3.4+−0.2	1.3

$$\tau_r = \frac{1}{Bn_o}, \tag{2.3}$$

where $B = 2.0 \times 10^{-10}\ cm^3/s$. All films show a decay constant above this radiative estimate and for the thickest films, τ_{DH} is as much as twelve times the radiative lifetime expected theoretically.

Figures 2.3 and 2.4 show plots of $1/\tau_{DH}$ vs. $2/w$ for each of the six electron densities investigated. When compared to the data of Nelson [31], these results are remarkably smooth, and each characteristic is distinctly nonlinear with a characteristic shape similar to that expected for photon recycling (as will be demonstrated in Sec. 2.5). This curvature makes

Table 2.3 Estimates for the interface recombination velocity for each electron concentration and the "surface lifetime," defined as w/2S, computed for the thinnest DH for each electron concentration.

n_o (cm^{-3})	S (cm/s)	τ_S (ns)
1.3×10^{17}	115	109
3.7×10^{17}	417	30
1.0×10^{18}	454	55
2.2×10^{18}	648	19
2.4×10^{18}	157	80
3.8×10^{18}	412	30

determination of a unique S impossible, so S is estimated from the slope of the characteristic between the two thinnest DH's since those DH's are the most sensitive to interface recombination and the least sensitive to photon recycling. From Eq. (2.1) with the assumption that τ_{bulk} is either negligible or independent of w, S is

$$S \leq \frac{1}{2}\frac{1/\tau_{DH1} - 1/\tau_{DH2}}{1/w_1 - 1/w_2}, \tag{2.4}$$

where the subscripts one and two refer to the thinnest DH and the second most thin DH, respectively. Equation (2.4) over-estimates S because it ignores the thickness-dependence of τ_{bulk}. The resulting upper limits for S at each electron density are listed in Table 2.3. Also shown are the corresponding "surface lifetimes," defined as $\tau_S = w/2S$, computed for the thinnest DH at each electron concentration. These values of τ_S are quite long so it is concluded that interface recombination is at most a small component of the decay rate for all DH's (with the possible exception of the thinnest films with $n_o \leq 3.7 \times 10^{17}$ cm^{-3}). For the most part, therefore, the DH's may be regarded as "surface-free" since the observed decay constants are controlled by bulk recombination processes. (The results shown in Chapter 4 show that $S \leq 11$ cm/s for the films with $n_o = 1.3 \times 10^{17}$ cm^{-3}.)

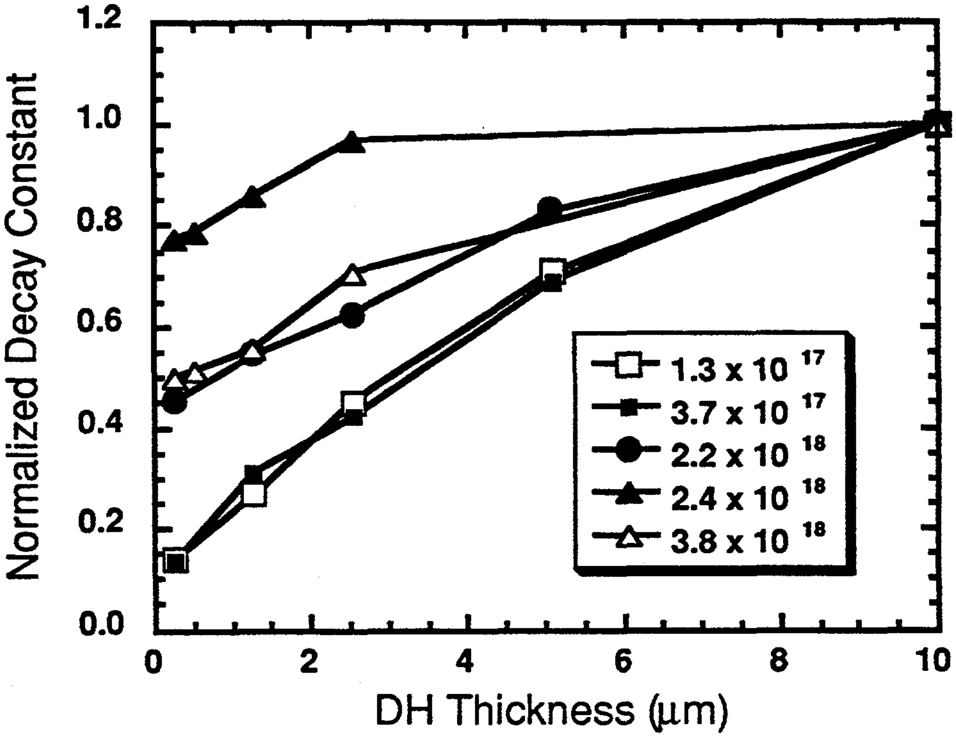

Figure 2.5 Normalized decay constants versus DH thickness, w, for each of the six different electron densities. In each case, τ_{DH} is normalized to the value at w = 10 μm. The films with $n_o = 2.4 \times 10^{18}$ cm^{-3}, which were grown more slowly, show the least variation with DH thickness.

Because plots of $1/\tau_{\mathrm{DH}}$ vs. $2/\mathrm{w}$ tell the observer nothing about τ_{bulk}, τ_{DH} vs. w is plotted for further insight. In these "surface free" DH's it is reasonable to neglect the 2S/w term in Eqs. (2.1) and (2.2) and write

$$\tau_{\mathrm{DH}} = \tau_{\mathrm{bulk}} = \frac{\phi_r \tau_r \tau_{nr}}{\phi_r \tau_r + \tau_{nr}}, \tag{2.5}$$

where τ_{nr} is a combination of the SRH and Auger lifetimes. Previous calculations of ϕ_r show that it increases seven-fold or more as w increases from 0.25 μm to 10 μm [15]. If $\tau_{nr} \gg \tau_r$, then $\tau_{\mathrm{DH}} \simeq \phi_r \tau_r$, and the change in τ_{DH} should be comparable to the expected change in ϕ_r. If τ_{nr} and τ_r are comparable, τ_{DH} will change less as w increases because τ_{DH} will approach τ_{nr}

for large w. Figure 2.5 plots the normalized decay constants versus w for five of the electron densities. (DH's with $n_o = 10^{18}$ cm^{-3} were left out since the thickest DH is 8 μm rather than 10 μm as with other electron concentrations.) The decay constants were normalized by dividing each τ_{DH} of a specific electron density by the value of τ_{DH} for the thickest sample at the same electron density. For $n_o \leq 3.7 \times 10^{17}$ cm^{-3}, τ_{DH} varies most significantly (nearly seven-fold) with w, which suggests that these films are controlled by radiative recombination and photon recycling ($\tau_{nr} \gg \tau_r$). As the electron concentration increases, the variation in τ_{DH} with DH thickness decreases. The τ_{DH} of the films grown at a reduced rate ($n_o = 2.4 \times 10^{18}$ cm^{-3}) vary the least with DH thickness, indicating that non-radiative recombination dominates for the thickest DH's with $n_o = 2.4 \times 10^{18}$ cm^{-3}. It is now of interest to determine which non-radiative mechanism is dominant in these DH's.

The effect on the PL decays of varying the laser intensity is now observed to show that the dominant non-radiative mechanism is SRH recombination. Figure 2.6 shows PL decays under various levels of laser excitation for the 10 μm DH with $n_o = 1.3 \times 10^{17}$ cm^{-3}. At the highest intensity (curve 1), the photoluminescence decay shows a non-exponential characteristic with the initial decay being most rapid. This behavior is typical of bimolecular radiative recombination when the majority carrier concentration is perturbed. After the initial, fast transient, the PL decay is exponential, and τ_{DH} is readily extracted by a least-squares fit. For each of the lower intensity decays (curves 2-3), the characteristic is exponential with the same time constant, and those time constants are similar to that deduced from the high-intensity curve in the region following the rapid, initial decay.

For DH's with higher electron concentrations, the intensity-dependent decays are more complex. Results for the 10 μm DH with $n_o = 3.8 \times 10^{18}$ cm^{-3} are displayed in Fig. 2.7 for three different laser intensities. (These detailed studies were performed on the films with $n_o = 3.8 \times 10^{18}$ cm^{-3} rather than on those with $n_o = 2.4 \times 10^{18}$ cm^{-3} because the former were more representative of the majority of the DH's.) At low laser excitation there is an exponential decay (curve 3) characterized by a single decay constant. As the excitation intensity is increased (curve 2), the PL decay becomes non-exponential with an initial decay rate that is slower than that observed under the lowest injection level. Under the highest laser excitation (curve 1), the initial decay rate is slower still. The decay rate of curve 3 is similar to the decay rates at the end of curves 1-2. The arrows in Fig. 2.7 point to these regions of similar decay constants. The fact that the initial, rapid decay characteristic of bimolecular, radiative recombination is not observed shows that low-level injection conditions are maintained. The

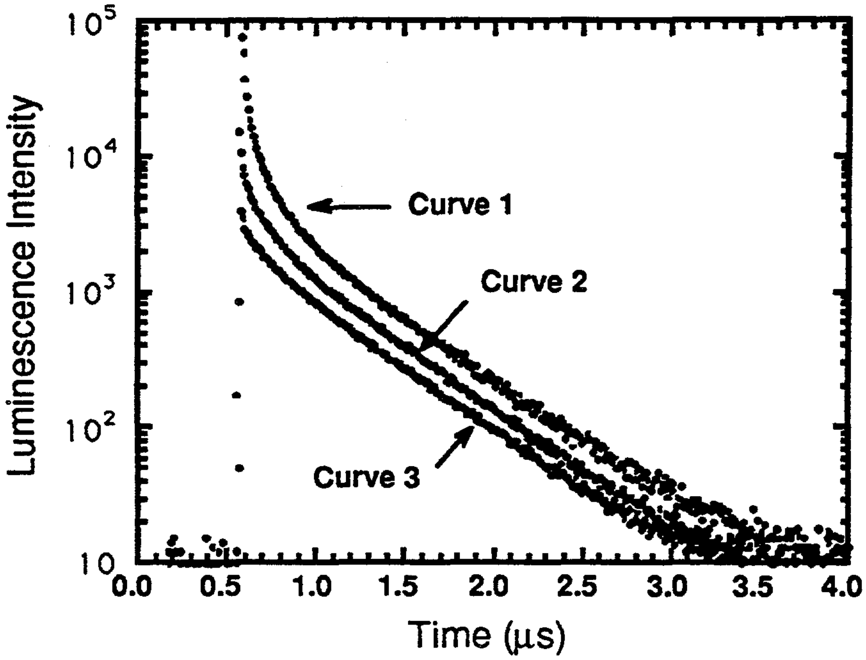

Figure 2.6 Measured PL decays for the $n_o = 1.3 \times 10^{17}$ cm^{-3}, 10 μm thick DH at three laser intensities.

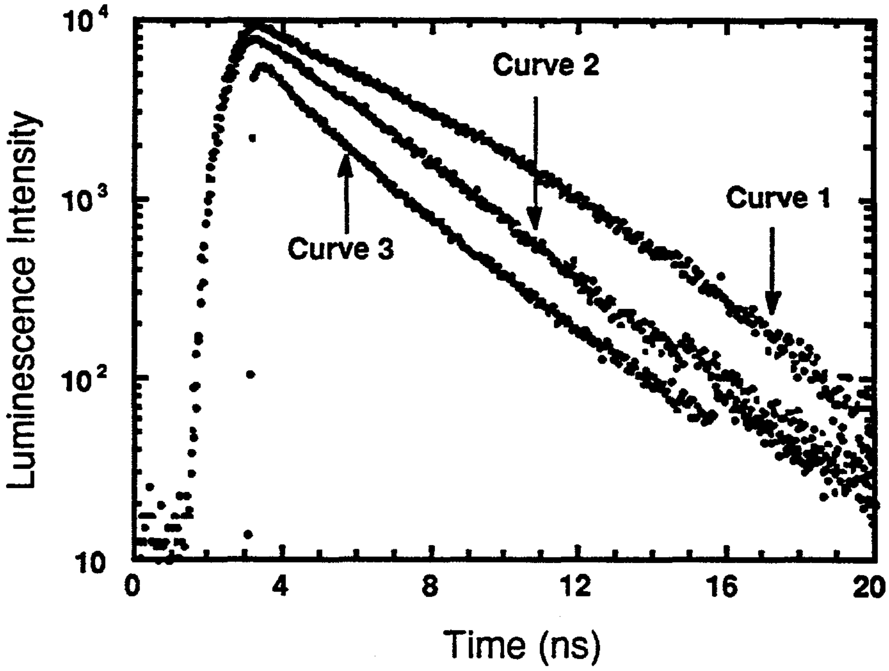

Figure 2.7 Measured PL decays for the $n_o = 3.8 \times 10^{18}$ cm^{-3}, 10 μm thick DH at three laser intensities.

intensity-dependence of the PL decays shown in curve 1 of Fig. 2.7 is caused by variations in the effective SRH lifetime due to saturation of the deep levels [40].

Under low injection conditions, the SRH recombination equation can be written as

$$R = \frac{\Delta p}{\dfrac{\Delta p}{n_o}\tau_n + \tau_p} = \frac{\Delta p}{\tau_{SRH_{eff}}} \tag{2.6}$$

where Δp is the excess carrier concentration, and $\tau_{SRH_{eff}}$ is the effective SRH lifetime. If Δp is very small, $\tau_{SRH} = \tau_p$. However, if $\Delta p \tau_n \simeq n_o \tau_p$, the deep levels become emptied and the effective SRH lifetime becomes longer than τ_p. The effective SRH lifetime becomes time dependent, and if $\tau_{SRH_{eff}}$ is sufficiently larger than τ_p, the bulk lifetime will approach the effective radiative lifetime. This can be observed experimentally under low injection conditions if $\tau_n \gg \tau_p$. Curve (1) of Fig. 2.7 shows three distinct regions of decay. The initial decay rate most closely represents the effective radiative lifetime. As the hole population decays, the SRH centers become refilled with electrons and the recombination rate increases. The increase in recombination rate at the very end of the decay is likely due to SRH centers at a lower energy level in the band gap, which become saturated at very low excitation densities. The intensity dependence of τ_{DH} is most prominent in the films with $n_o = 2.4 \times 10^{18}$ cm^{-3}, which were grown at a slower growth rate than the other DHs. This correlates with the fact that these films exhibit the smallest thickness dependence and shows that the non-radiative recombination is dominated by SRH mechanisms.

The selenium concentration was measured for each electron concentration by secondary ion mass spectrometry (SIMS) in a Cameca IMS-3f using cesium as the ionizing source. It was found that the selenium concentration was approximately equal to the electron concentration for all films except those grown at four microns per hour ($n_o = 2.4 \times 10^{18}$ cm^{-3}), for which the actual selenium concentration was $N_{Se} = 4.1 \times 10^{18}$ cm^{-3}. (For a more detailed discussion of the SIMS measurements, see Sec. 3.5.) This extra selenium or perhaps additional background impurities incorporated due to the slower growth rate could be the cause of the shorter SRH lifetime. Remember, however, that even though SRH recombination is important, τ_{DH} for EACH film is greater than the estimated radiative lifetime (See Table 2.2).

With the measurements reported here, we are unable to determine the contribution from Auger recombination. None the less, we can set an upper limit on C_n, the Auger coefficient, if we attribute all the recombination in a DH to Auger mechanisms. We find that under high intensity excitation, the decay constant of the 10 μm thick DH with $n_o = 3.8 \times 10^{18}$ cm^{-3} yields an upper limit for C_n of 1.6×10^{-29} cm^6/s, which is an order of magnitude smaller than $C_n = 1.5 \times 10^{-28}$ cm^6/s deduced by Puhlmann *et al.* Haug computed the C_n theoretically to be 0.47×10^{-29} cm^6/s in n-type GaAs [27]. Since SRH recombination is significant in our DHs at higher electron concentrations, the actual value of C_n in our material must be significantly smaller, so Haug's computation is consistent with our results.

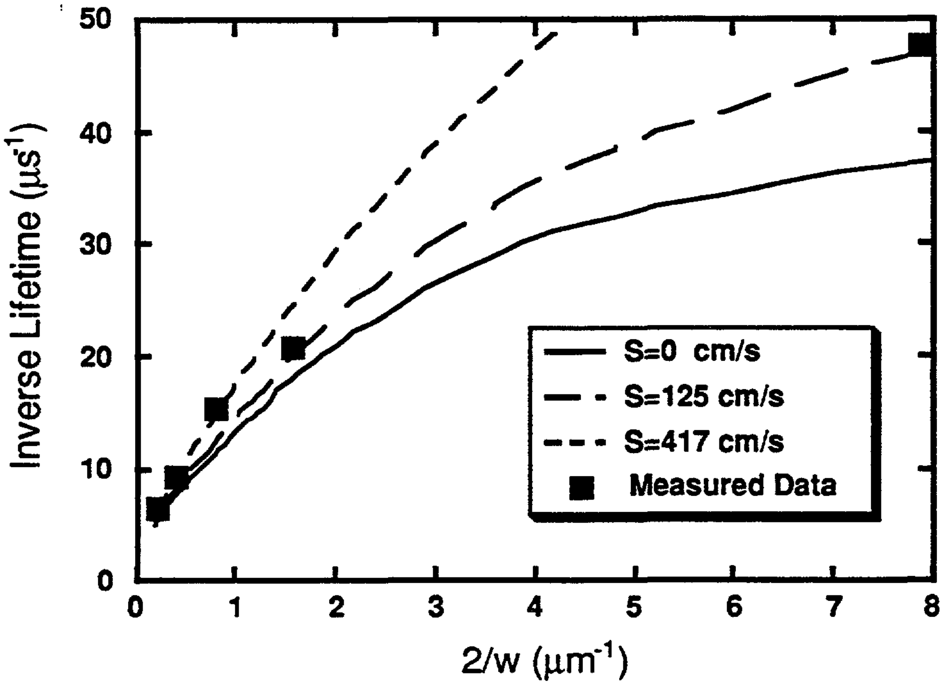

Figure 2.8 Inverse decay constant versus 2/w computed theoretically assuming that bulk recombination is dominated by radiative recombination and photon recycling, and with interface recombination as a parameter. This figure shows that curvature in plots of $1/\tau_{DH}$ vs. 2/w can be explained by photon recycling.

2.5 Further Evidence for Photon Recycling

The unusually long lifetimes observed and the curvature seen in plots of $1/\tau_{DH}$ vs. $2/w$ suggest the presence of photon recycling. To show this more convincingly, Fig. 2.8 compares a theoretical calculation of $1/\tau_{DH}$ vs. $2/w$ with the measured results for $n_o = 3.7 \times 10^{17}$ cm^{-3}. The DH decay constant, τ_{DH}, is evaluated from Eq. (2.1) assuming that $\tau_{bulk} = \phi_r \tau_r$, and the result of that is compared to the measured data. Values for ϕ_r are taken from the literature [15]. Figure 2.8 shows that the measured characteristic is well-described by photon recycling theory if $S \simeq 125$ cm/s. Figure 2.8 also shows that higher interface recombination velocities produce more linear characteristics. The smooth, nonlinear $1/\tau_{DH}$ characteristics observed indicate that the interface quality is excellent in these DH's.

In addition to increasing the observed lifetime, self-absorption should also cause a shift in the peak energy of steady-state photoluminescence (PL), due to the energy-dependence of the absorption depth of spontaneous emission [41]. The peak of the observed steady-state PL for thicker DH's should be shifted in the direction of the red relative to that of the thinner films because the high energy photons are more strongly absorbed in the thicker DH's before they can be emitted and detected. Figure 2.9 displays the steady-state PL spectra for DH films with $n_o = 1.3 \times 10^{17}$ cm^{-3}. It is clear that the peak of the observed emission for the thicker films is shifted to the red relative to the peak of the observed emission of the thinner films. This red shift is evidence of self-absorption. The amount of the red shift decreases with increasing electron concentration, indicating that n-GaAs becomes more transparent to its own emission at higher electron concentrations.

2.6 Summary and Remaining Issues

This chapter described a comprehensive study of minority carrier recombination in n-type GaAs. The characteristics of the lifetimes versus electron density can be described in terms of radiative and SRH recombination. For $n_o < 10^{18}$ cm^{-3}, the lifetime appears to be dominated by radiative recombination and photon recycling. For $n_o > 10^{18}$ cm^{-3}, SRH recombination is also observed, but radiative recombination is still important as evidenced by the curvature in plots of $1/\tau_{DH}$ vs. $2/w$. Even for the most heavily doped films, there is no evidence of Auger recombination.

When compared to previous studies of LPE-grown films, these results for high-quality MOCVD films show significantly higher minority carrier lifetimes, especially at low electron densities. The reduced non-radiative recombination, attributed to lower defect densities, allows an excellent opportunity to

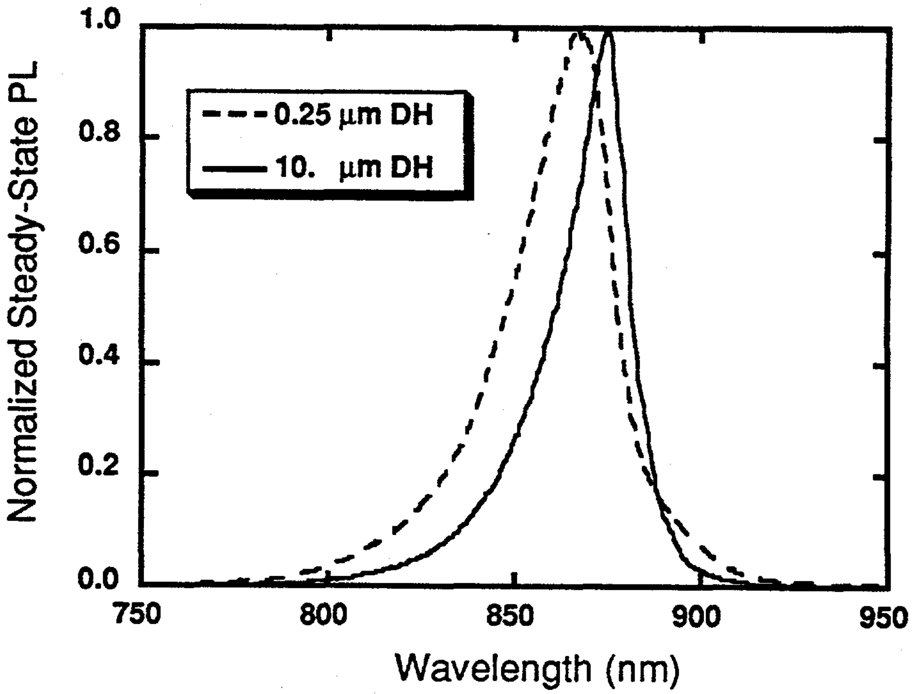

Figure 2.9 Steady-state, room-temperature PL spectra for the AlGaAs/GaAs/AlGaAs double heterostructures for two GaAs layer thicknesses. For this particular sample, the GaAs layers have $n_o = 1.3 \times 10^{17}$ cm^{-3}.

investigate intrinsic recombination processes. Nevertheless, further work is needed before the B-coefficient or the Auger coefficient can be deduced versus electron density. The recycling cofactor, ϕ_r, must be computed in order to compute B, and such a calculation requires data for the concentration-dependent absorption coefficient, $\alpha(h\nu)$. The reliability of available α data is uncertain since it may have been influenced by precipitates [25], so new measurements of the concentration-dependent α are required. The work described in this chapter is only the first step in gaining a full quantitative understanding of recombination in n-type GaAs, but it has established the importance of radiative recombination and photon recycling in MOCVD, n-type GaAs doped at the levels of interest for device applications.

CHAPTER 3

MEASUREMENT OF THE NEAR BAND-EDGE ABSORPTION COEFFICIENT

3.1 Introduction

As was mentioned briefly in Chapter 1, knowledge of the doping dependence of the near band-edge absorption coefficient versus photon energy, $\alpha(h\nu)$, is vital to the interpretation of photoluminescence measurements [7, 41, 42] in GaAs, the calculation of emission spectra for GaAs lasers [25], and to the detailed understanding of recombination in GaAs. Calculations of the effects of photon recycling in devices such as lasers, double heterostructures, and solar cells also require the concentration dependent $\alpha(h\nu)$ [15, 20, 22, 24]. The above references used the classic, comprehensive study of $\alpha(h\nu)$ by Casey *et al.* [10] for their models of photon recycling in n- and p-type GaAs. However, Casey and Stern [25] expressed concern about the results of Casey *et al.* for n-type GaAs because they were unable to theoretically model $\alpha(h\nu)$, and because the results differed from those of Hill [11] and of Hwang [7]. Another issue is that the measurements of Casey *et al.* were made on melt-grown n-GaAs, and there was concern that compensation and precipitates might influence their results [25]. These uncertainties and the fact that data is not available for n-GaAs grown by modern epitaxial techniques necessitate a new study of optical absorption in n-type GaAs.

This chapter contains the results of transmission experiments to deduce the concentration dependent absorption coefficient in n-type GaAs grown by metalorganic chemical vapor deposition (MOCVD) over the photon energy range of 1.35-1.7 eV. This study covers the same six selenium doping concentrations producing free electron concentrations in the range of $1.3 \times 10^{17} \leq n_o \leq 3.8 \times 10^{18}$ cm^{-3}. For $n_o < 10^{18}$ cm^{-3}, there is basic agreement with the data of Casey *et al.* for photon energies in the absorption tail, but these results at high energies show $\alpha(h\nu)$ to be about 20-25% larger for all donor concentrations. At the highest electron concentrations studied, the results differed from Casey's even in the band tail, and it is shown later that these differences are most likely due to compensation in their material. These comprehensive results are of interest to researchers studying band structure in heavily doped GaAs and to those modeling lasers, double heterostructures, or solar cells. They are especially important because of the effects that compensation has on the deduced $\alpha(h\nu)$.

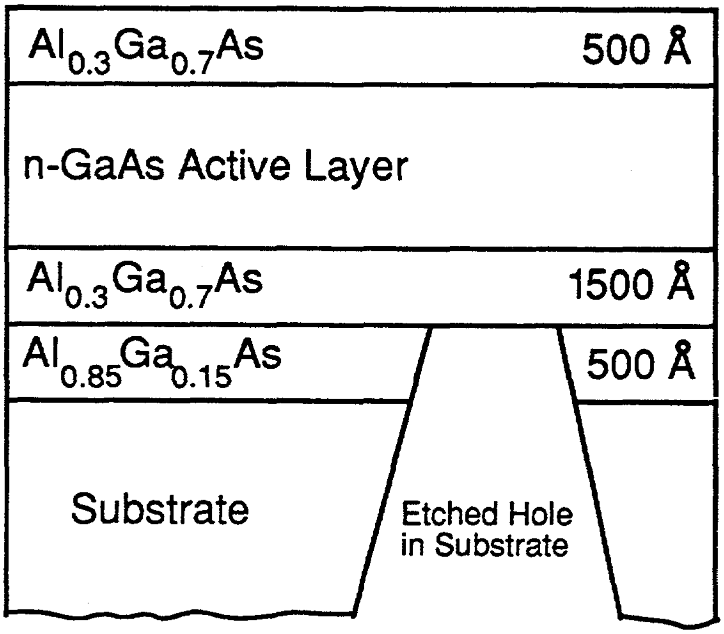

Figure 3.1 The basic structure of the double heterostructures grown for this study. The $Al_{0.85}Ga_{0.15}As$ layer acts as an etch-stop.

3.2 Experimental Procedures

The basic structure of the DH's is shown in Fig. 3.1. The cladding $Al_{0.3}Ga_{0.7}As$ layers provide carrier confinement for lifetime measurements [43] while the $Al_{0.85}Ga_{0.15}As$ acts as an etch-stop layer [44]. Table 3.1 lists the measured thickness of each of the DH's used in this study. The thicknesses were determined with a scanning electron microscope (SEM) by viewing an adjacent piece of the wafer after it had been "stained" by a 25-second dip in a solution of deionized (DI) water, hydrofluoric acid (HF), and 30% hydrogen peroxide (H_2O_2) mixed with a ratio of 10:1:1 DI:HF:H_2O_2 [45].

To prepare the samples for the transmission experiments, a hole was etched through the substrate by wet chemical etching. The samples were

Table 3.1 Measured GaAs electron densities and thicknesses for each of the double heterostructures used for this study.

Double Heterostructure Parameters			
n_o (cm^{-3})	Measured Thicknesses (μm)		
1.3×10^{17}	2.2	4.68	8.6
3.7×10^{17}	2.32	5.55	9.67
1.0×10^{18}	1.65	3.5	5.8
2.2×10^{18}	2.6	4.55	9.
2.4×10^{18}	---	2.25	9.15
3.8×10^{18}	---	2.12	8.7

placed face down in black wax melted on a glass slide. The wax covered the edges and part of the substrate, leaving an area of the substrate exposed in the middle. The mounted sample was then immersed in a room temperature solution of 50 grams of granular citric acid dissolved in 50 milliliters of DI water and 10 milliliters of H_2O_2. The typical etching time before the $Al_{0.85}Ga_{0.15}As$ layer was exposed was 36 hours. Since this mixture etches $Al_{0.85}Ga_{0.15}As$ as much as 100 times more slowly than it etches GaAs [44,46], the area of exposed $Al_{0.85}Ga_{0.15}As$ looked specular relative to the roughened substrate. Once this specular area of exposed $Al_{0.85}Ga_{0.15}As$ was large enough (2-3 millimeters in diameter), the sample was rinsed in DI and the $Al_{0.85}Ga_{0.15}As$ layer was removed by a 30-second dip in hydrogen fluoride (HF) diluted with DI to 5% by volume. HF removes high mole fraction AlGaAs much faster than it does low mole fraction AlGaAs [35]. The sample was then unmounted by soaking in trichloroethane. The thin film was still attached at the periphery to the substrate, so the sample was easily handled with tweezers. Where the substrate was removed, the thinner DH's ($w < 4$ μm) exhibited a slight bowing possibly due to the lattice mismatch of the GaAs-AlGaAs interfaces, but no evidence of strain was observed in the results.

Figure 3.2 shows a block diagram of the experimental apparatus. The output of a 1000-Watt halogen lamp was focused onto the input slit of a 1/8

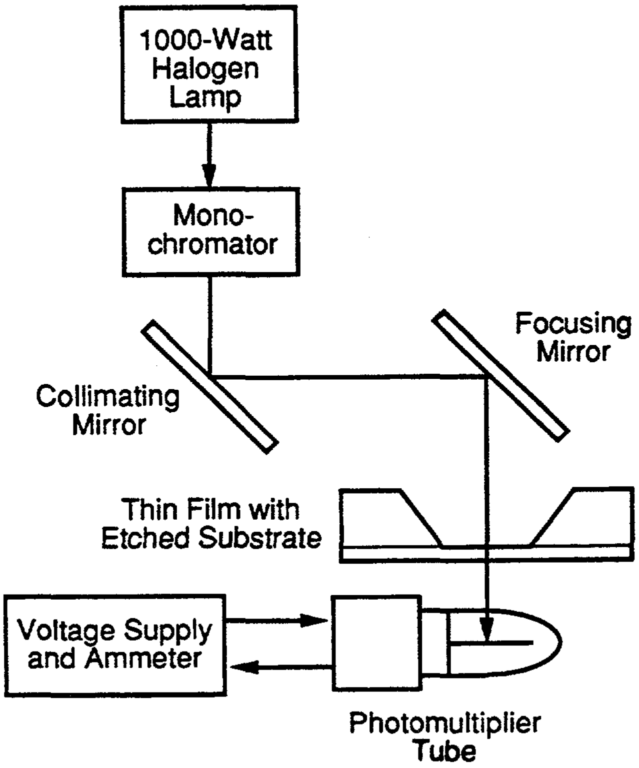

Figure 3.2 Block diagram of the experimental set-up.

meter scanning monochromator. The slit widths were set to 0.3 mm which allowed a band-pass of less than 2 nm full width at half maximum at 545 nm. (This was measured by observing the output of the monochromator illuminated with a mercury vapor lamp.) A long-pass filter with a 50% cutoff at $\lambda = 630\,\text{nm}$ was used to block higher order wavelengths transmitted through the monochromator. The output of the monochromator was collimated using a fused silica plano convex lens and an aluminum mirror with a radius of curvature of 1.0 meter. The focusing mirror had a 0.1 meter radius of curvature, narrowing the light beam to an area about 2 mm in diameter. Light detection was by an S1 photomultiplier used at room temperature. The measurements were taken while the room temperature was 18–20 °C. The output wavelength of the monochromator was varied from 700 to 1000 nm in steps of 2.0 nm. Data were taken over all wavelengths with the sample illuminated from the back side, and then data were recorded with the sample removed.

The selenium concentration was measured by secondary ion mass spectrometry (SIMS) in a Cameca IMS-3f using cesium as the ionizing source. The electron concentration, measured by the van der Pauw technique, was found to be approximately equal to the selenium concentration for all films except those grown at four microns per hour ($n_o = 2.4 \times 10^{18}$ cm^{-3}).

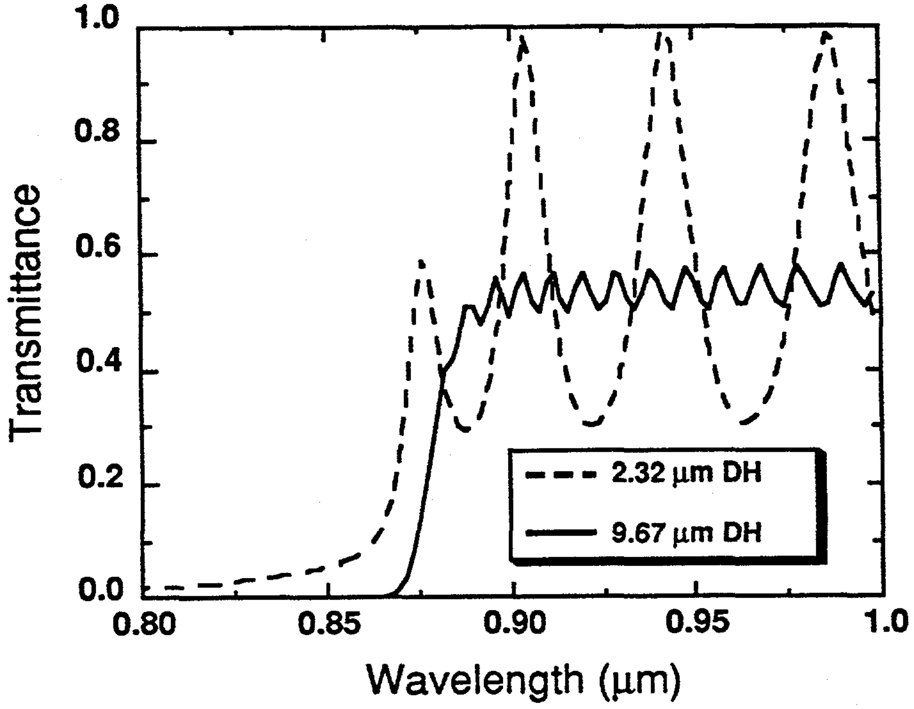

Figure 3.3 Transmittance versus photon wavelength for the 2.32 and 9.67 μm samples with $n_o = 3.7 \times 10^{17}$ cm^{-3}. The oscillations for photon energies below the bandgap energy are due to interference effects which one can model by treating the DH as a Fabry-Perot cavity.

3.3 Deducing Absorption Coefficient from Transmittance

Figure 3.3 shows the transmittance for the 2.32 and 9.67 μm samples with $n_o = 3.7 \times 10^{17}$ cm^{-3}. (Appendix C lists the transmission data for all samples studied.) The oscillations for photon energies below the bandgap energy are due to interference effects which one can model by treating the DH as a Fabry-Perot cavity. The transmittance of the 2.32 μm sample peaks near 1.0

for certain wavelengths, indicating that the surfaces are specular.

It was attempted to model the $Al_{0.3}Ga_{0.7}As/GaAs/Al_{0.3}Ga_{0.7}As$ layers completely, by retaining the phase information so that the interference effects could be modeled. This proved unsatisfactory possibly due to any of several factors. First, the thicknesses of the $Al_{0.3}Ga_{0.7}As$ layers were not known, and even if the thicknesses were measured beforehand, there would still be uncertainty because some of the back $Al_{0.3}Ga_{0.7}As$ layer could have been removed during the etches. Second, there are no data for the index of refraction, n, of $Al_{0.3}Ga_{0.7}As$ which include both energy and doping dependences so uncertainties in n could be significant. Finally, as mentioned below, the effective coherence length, as represented by the strength of the interference effects, increases with increasing n_o. We have no explanation for this dependence on n_o so we are unable to produce a model for the effective coherence length. Because of the inability to model the wave nature of the photons, light was treated as corpuscular. The absorption coefficient, $\alpha(h\nu)$, is therefore deduced directly from the measured transmittance, $T(h\nu)$, using

$$T(h\nu) = \frac{(1-R)^2 e^{-\alpha(h\nu)w}}{1 - R^2 e^{-2\alpha(h\nu)w}}\,, \tag{3.1}$$

where R is the reflectance of a single air—$Al_{0.3}Ga_{0.7}As$ interface, and w is the thickness of the GaAs active area. It is assumed that R is independent of energy for this analysis procedure. To demonstrate that this generates little uncertainty, R is computed by

$$R = \left[\frac{n-1}{n+1}\right]^2, \tag{3.2}$$

where data for n, the index of refraction of the $Al_{0.3}Ga_{0.7}As$ layers, are taken from the literature [47]. It is found that $R = 0.31 \pm 0.01$ for the photon energies of interest.

In the actual data analysis, however, R is computed directly from the transmission experiments by first determining T_{ave}, the average of $T(h\nu)$ for photon wavelengths $0.9 \le \lambda \le 1.0\ \mu m$ (where $\alpha(h\nu) \simeq 0$). By setting $\alpha(h\nu) = 0$ in Eq. (1), R can be written as,

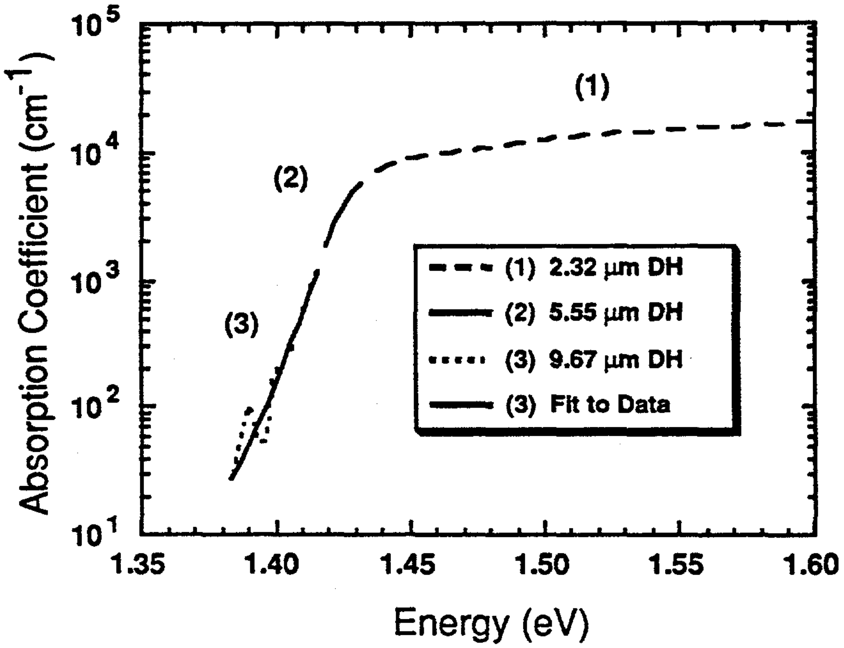

Figure 3.4 Plot showing how each double heterostructure thickness (regions (1)-(3)) contributes to determining $\alpha(h\nu)$ for $n_o = 3.7 \times 10^{17}$ cm^{-3}. The region of the curve with smallest $\alpha(h\nu)$ also shows how the interference effects seen in Fig. 3.3 can generate oscillations in the results. The line drawn through the oscillations is the result of a least-squares fit to the log of $\alpha(h\nu)$. This was done for all doping concentrations in a like manner to produce the final results.

$$R = \frac{1 - T_{ave}}{1 + T_{ave}}. \tag{3.3}$$

For all electron concentrations, T_{ave} of the thickest DH was within 0.54 ± 0.01. This gives $R = 0.30 \pm 0.01$ and yields values of 3.4 ± 0.1 for the index of refraction of the $Al_{0.3}Ga_{0.7}As$ layers. Previous authors [39,47] obtained $n \simeq 3.4$ in nominally undoped $Al_{0.3}Ga_{0.7}As$ for this range of photon energies. The dependence of $T(h\nu)$ on R is weak until the layer is sufficiently transparent to the incident radiation that the second term in the denominator of Eq. (1) becomes important [36]. Therefore, small uncertainties in R will have little observable effect on the final values of $\alpha(h\nu)$.

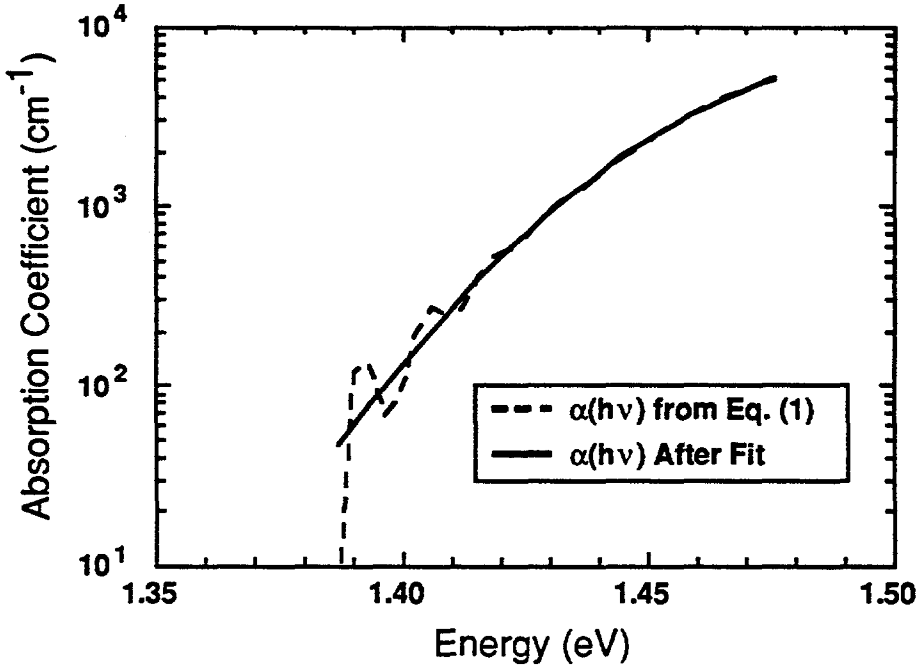

Figure 3.5 Plot comparing $\alpha(h\nu)$ before and after least-squares fit to the data deduced from Eq. (1) for the 8.7 μm DH with $n_o = 3.8 \times 10^{18}$ cm^{-3}.

Once R is determined from T_{ave}, $\alpha(h\nu)$ is deduced from Eq. (1). The greatest confidence in the deduced $\alpha(h\nu)$ is for $0.005 \leq T(h\nu) \leq 0.35$. $T(h\nu) \simeq 0.005$ is the limit of the experimental accuracy while for $T(h\nu) > 0.35$, $\alpha(h\nu)$ becomes more strongly dependent on R, so uncertainty in R can cause greater uncertainty in $\alpha(h\nu)$. Each DH thickness, therefore, contributes to a different region of the plot of $\alpha(h\nu)$, depending on the value of $T(h\nu)$. Overlap between two regions provides a check for self-consistency. An illustration of this is shown in Fig. 3.4 which plots the contribution from each of the three DH's used to deduce $\alpha(h\nu)$ for $n_o = 3.7 \times 10^{17}$ cm^{-3}. The broken and solid lines separate the contributions each DH makes to the deduced $\alpha(h\nu)$. The region of the curve with smallest $\alpha(h\nu)$ also shows how the interference effects seen in Fig. 3.3 can generate oscillations in the results. The line drawn through the oscillations is the result of a least-squares fit to the log of $\alpha(h\nu)$.

This was done for all electron concentrations in a like manner to produce the final results. Interestingly, it is found that the magnitude of the Fabry-Perot-like oscillations in T(hν) increased with increasing selenium concentration, making it increasingly difficult to deduce α(hν) for weakly absorbed light. Figure 3.5 shows α(hν) deduced from Eq. (1) for the 8.7 μm DH with $n_o = 3.8 \times 10^{18}$ cm^{-3} and also shows the final plot of α(hν) after the least-squares fit. Although the oscillations are much stronger than those depicted in Fig. 3.4, the least-squares fit describes the data nicely.

3.4 Results

Figures 3.6 and 3.7 show the results for the six electron concentrations. For $n_o \lesssim 1.0 \times 10^{18}$ cm^{-3}, the data displayed in these figures show behavior that is qualitatively similar to that of previous authors [7, 10, 11]. The data show the expected exponential absorption tail known as the Urbach tail [48]. This has been seen by many authors and those references and a review of possible causes of the Urbach tail are given by Blakemore [49]. The slope of the absorption tail decreases with increasing electron concentration as has been observed previously [7, 10, 11]; this has been attributed to tails in the density of states, caused by the impurity atoms [25, 50]. As n_o increases, the absorption tail is shifted to higher energies, which is due to the filling of electron states, known as the Burstein shift [51]. Of special note is the fact that the value of α(hν) at hν = 1.7 eV for $n_o = 3.7 \times 10^{17}$ cm^{-3} is about 9% below the corresponding values for the concentrations of $n_o = 1.3 \times 10^{17}$ cm^{-3} and $n_o = 1.0 \times 10^{18}$ cm^{-3}. This effect was also observed by Casey *et al.* for $n_o = 5.9 \times 10^{17}$ cm^{-3}.

As shown in Fig. 3.7, the slope of the absorption tail continues to decrease with increasing electron concentration for $n_o > 10^{18}$ cm^{-3}, and the magnitude of the Burstein shift continues to increase. At high energies α(hν) approaches nearly the same value for these three electron concentrations, and with the exception of $n_o = 3.7 \times 10^{17}$ cm^{-3}, the values of α(hν) at hν = 1.7 eV for all concentrations are within $2.32 \pm 0.07 \times 10^4$ cm^{-1}.

A significant aspect of these results is that α(hν) for $n_o = 2.2 \times 10^{18}$ cm^{-3} and $n_o = 2.4 \times 10^{18}$ cm^{-3} are quite dissimilar while α(hν) of 2.4 and 3.8×10^{18} cm^{-3} are nearly indistinguishable. Remember that the films with $n_o = 2.4 \times 10^{18}$ cm^{-3} were grown at a slower rate by adjusting the III-V flow ratio. In Sec. 5 the results of SIMS measurements will be discussed which show that the actual concentration of selenium in the films with the electron concentration of $n_o = 2.4 \times 10^{18}$ cm^{-3} was $N_{Se} = 4.1 \times 10^{18}$ atoms/cm^3, far greater than the free electron concentration given by the van der Pauw

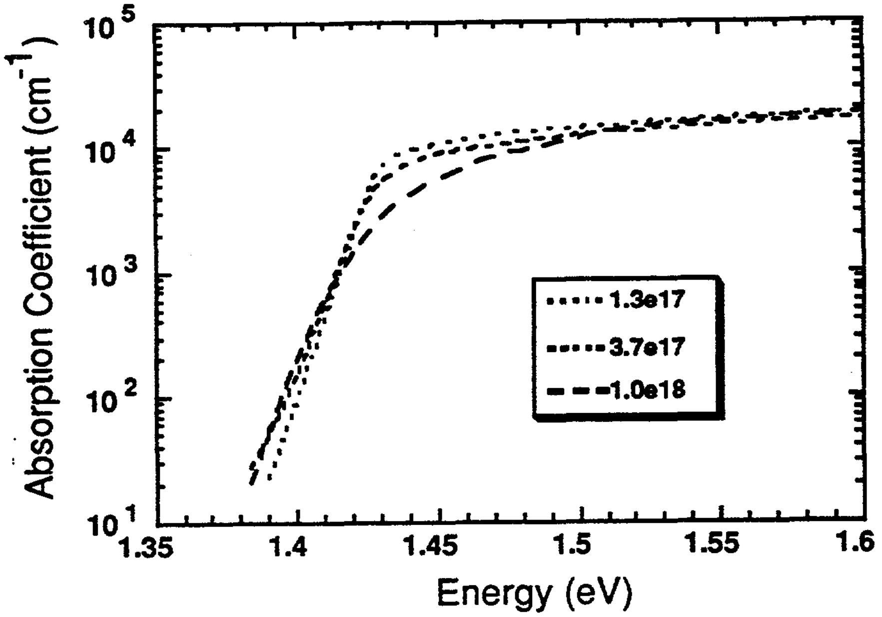

Figure 3.6 Room temperature results of $\alpha(h\nu)$ for $n_o \leq 1.0 \times 10^{18}$ cm^{-3}.

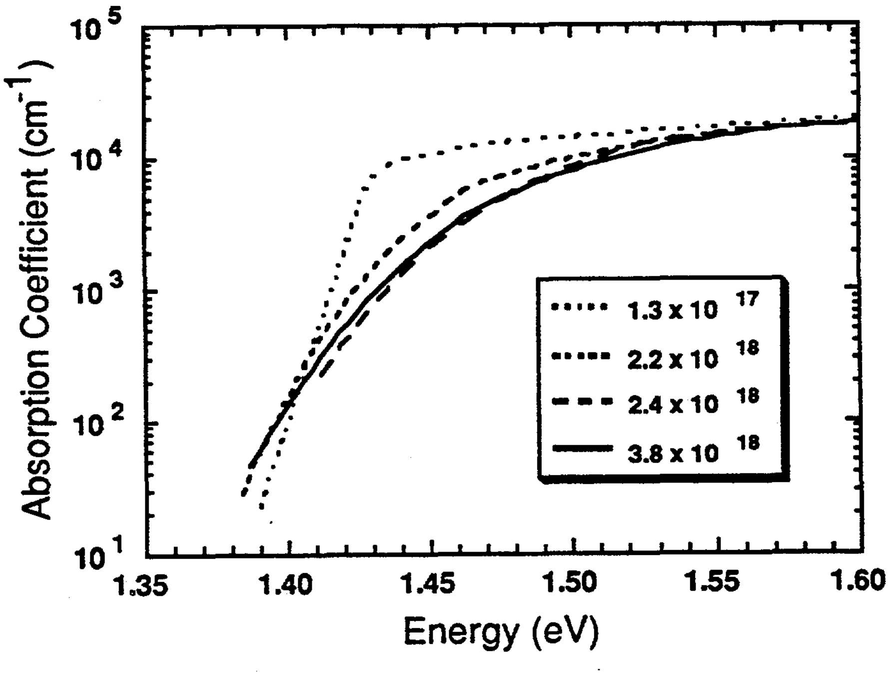

Figure 3.7 Room temperature results of $\alpha(h\nu)$ for $n_o \geq 2.2 \times 10^{18}$ cm^{-3}. Also shown is $\alpha(h\nu)$ for $n_o = 1.3 \times 10^{17}$ cm^{-3} for reference.

technique. Appendix B lists the values of $\alpha(h\nu)$ for five of the six electron concentrations; the data for $n_o = 2.4 \times 10^{18}$ cm^{-3} are omitted because they are inconsistent with the others.

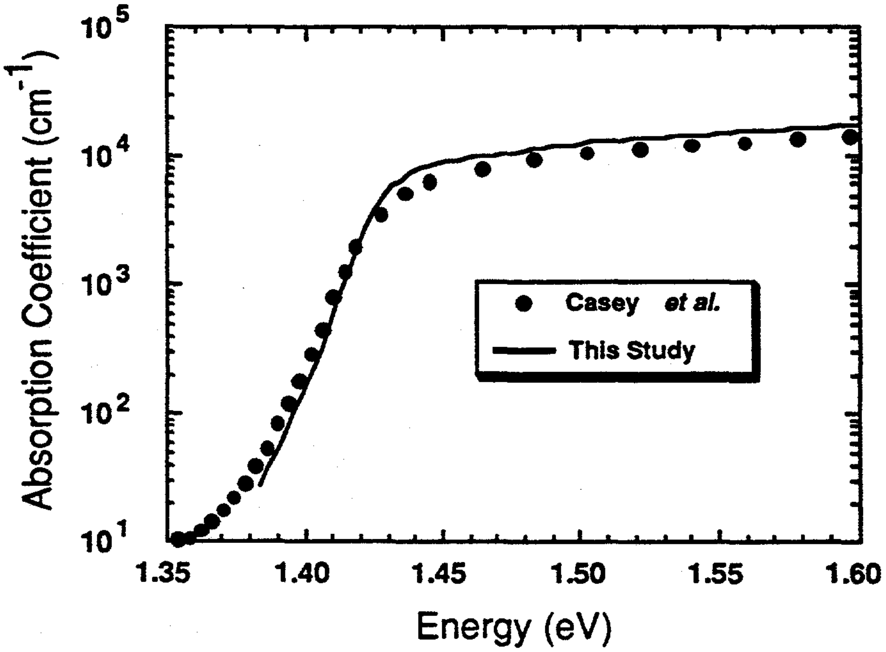

Figure 3.8 Comparison of these results for $n_o = 3.7 \times 10^{17}$ cm^{-3} to those of Casey *et al.* The "data points" of Casey *et al.* are interpolated. There is agreement at the absorption edge, but significant differences exist at photon energies greater than the bandgap.

3.5 Discussion

It is now helpful to quantitatively compare these results to the oft-cited data reported by Casey *et al.* [10], which is the most comprehensive study of $\alpha(h\nu)$ in n-type GaAs. Casey *et al.* combined transmission measurements on thick samples to determine $\alpha(h\nu)$ for values less than 10^3 cm^{-1}, and a Kramers-Kroenig [52] analysis of reflection measurements to determine higher $\alpha(h\nu)$. Since the carrier concentrations of these samples differ from those of Casey *et al.*, the "results" presented from Casey's work are actually linearly interpolated to the electron concentrations measured in these samples. Also, Casey *et al.* did not measure the absorption tail of their sample with $n_o = 5.0 \times 10^{16}$ cm^{-3}, but instead used Sturge's data [53] to complete the plot.

For the $n_o = 1.3 \times 10^{17}$ cm^{-3} samples, the absorption tail has the same slope as that found by Sturge, and the $\alpha(h\nu)$ above the bandgap for this work are larger than the data of Casey *et al.* by about 20-25%. For $n_o = 3.7 \times 10^{17}$ and 1.0×10^{18} cm^{-3}, these results agree with those of Casey *et al.*, for $\alpha(h\nu) < 3000$ cm^{-1}, as represented in Fig. 3.8 for $n_o = 3.7 \times 10^{17}$ cm^{-3}. Thus, strong quantitative agreement with Casey *et al.*, is found but only in a narrow range of electron concentration and only in the region where they relied on transmission experiments for deducing $\alpha(h\nu)$. Casey and Stern felt that the Kramers-Kroenig analysis would be less accurate on n-type GaAs than on p-type GaAs [25], so the discrepancy for high energy photons is not surprising.

At higher electron concentrations, it is found that these data differ from that of Casey's for $n_o = 2.2$ and 3.8×10^{18} cm^{-3}, but are similar at the absorption edge for $n_o = 2.4 \times 10^{18}$ cm^{-3}. This apparent anomaly is illustrated in Fig. 3.9 which compares these results for $n_o = 3.8 \times 10^{18}$ cm^{-3} to those of Casey *et al.* interpolated to $n_o = 2.4$ and 3.8×10^{18} cm^{-3}. It is clear from the plot that these results for $n_o = 3.8 \times 10^{18}$ cm^{-3} do not agree with Casey's for $n_o = 3.8 \times 10^{18}$ cm^{-3}, but the former agree quite well with Casey's $\alpha(h\nu)$ interpolated to $n_o = 2.4 \times 10^{18}$ cm^{-3}. Remembering that the $\alpha(h\nu)$ presented here for $n_o = 2.4 \times 10^{18}$ cm^{-3} and for 3.8×10^{18} cm^{-3} are quantitatively similar, it is concluded that surprisingly these $\alpha(h\nu)$ for $n_o = 2.4 \times 10^{18}$ cm^{-3} agree reasonable well with Casey's interpolated data. It is believed that this apparent inconsistency is due to compensation in Casey's Te-doped, melt-grown n-GaAs, and unionized impurities in the more slowly grown Se-doped films, for which the electron concentration was 2.4×10^{18} cm^{-3}.

Figure 3.10 shows the SIMS data for the films grown by MOCVD. Each sample was probed in several different areas and the measured dopant concentrations averaged to determine the selenium concentration in each sample. Since SIMS is more accurate when trying to find relative concentrations rather than absolute concentrations, the SIMS results were then scaled using the lowest electron concentration measured by van der Pauw to produce the data points in Fig. 3.10. The abscissa of Fig. 3.10 is the electron concentration as measured by the van der Pauw technique, the ordinate is the selenium concentration as measured by SIMS, and the line represents the expected electron concentration if all the impurities were ionized with no compensation ($n_o = N_D$). The data suggest that the impurities were fully

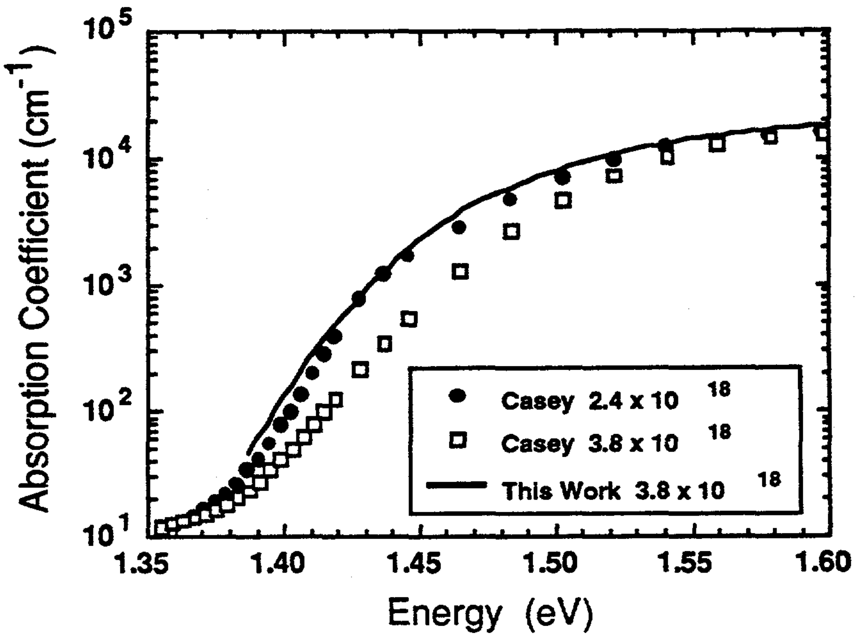

Figure 3.9 Comparison of these results for $n_o = 3.8 \times 10^{18}$ cm^{-3} to those of Casey *et al.*, interpolated for $n_o = 2.4$ and 3.8×10^{18} cm^{-3}.

ionized with no compensation in all the films with the exception of those with $n_o = 2.4 \times 10^{18}$ cm^{-3}, for which the actual selenium concentration deduced from SIMS was $N_{Se} \simeq 4.1 \times 10^{18}$ cm^{-3}. The mass spectra of the two most highly doped films (these have similar selenium concentrations) reveal no other impurities that could cause compensation. Finally, Table 3.2 shows the measured mobilities of the samples. These mobilities are consistent with data previously reported for n-GaAs [54, 55]; this includes the mobility of the sample with $n_o = 2.4 \times 10^{18}$ cm^{-3}. There is, therefore, no evidence of compensation in any of these films.

SIMS measurements showed that the actual selenium concentration was $N_{Se} \simeq 4.1 \times 10^{18}$ cm^{-3} for the reduced growth-rate films in which $n_o = 2.4 \times 10^{18}$ cm^{-3}, and that $N_{Se} \simeq 3.7 \times 10^{18}$ cm^{-3} for the films with $n_o = 3.8 \times 10^{18}$ cm^{-3}. This similarity of N_{Se} could explain the similarity in $\alpha(h\nu)$ between these two electron concentrations, which was depicted in Fig.

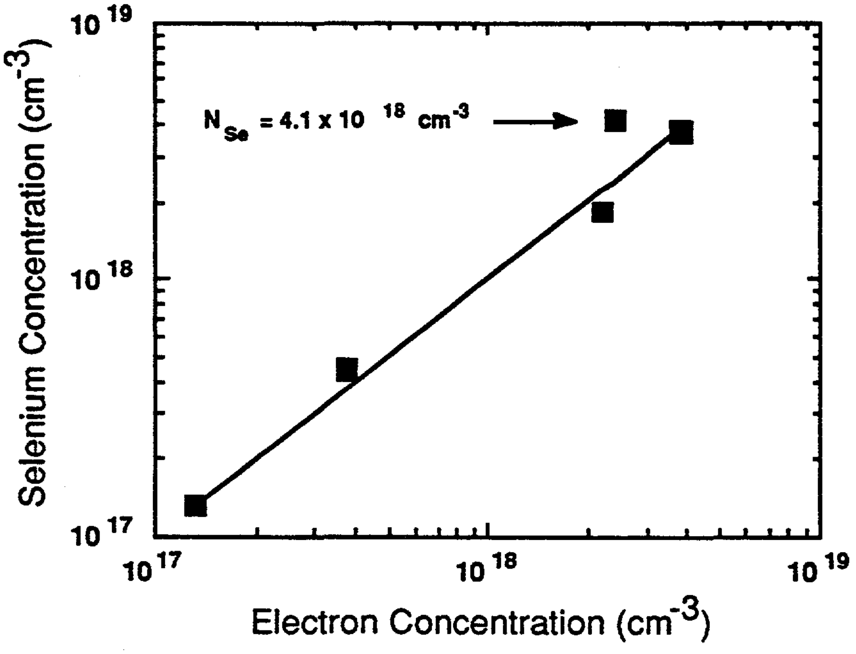

Figure 3.10 Comparison of free electron concentration and relative selenium concentration. The abscissa is the electron concentration as measured by the van der Pauw technique, the ordinate is the selenium concentration as measured by SIMS, and the line represents the expected electron concentration if all the impurities were ionized with no compensation ($n_o = N_D$). The data suggest that the impurities were fully ionized in all the films with the exception of those with $n_o = 2.4 \times 10^{18}$ cm^{-3} for which the actual selenium concentration was $N_{Se} = 4.1 \times 10^{18}$ cm^{-3}.

3.7. Note also that Casey and Stern estimated that $N_D^+/N_A^- = 5$ for the samples used by Casey *et al.* If they had had a sample with a free electron concentration of $n_o \simeq 2.4 \times 10^{18}$ cm^{-3}, the ionized impurity concentration would correspond to $N_D^+ + N_A^- \simeq 3.6 \times 10^{18}$ cm^{-3}, nearly the same concentration as the $n_o = 3.8 \times 10^{18}$ cm^{-3} from this study. Such similarity in N_{Se} could explain why these $\alpha(h\nu)$ for $n_o = 3.8 \times 10^{18}$ cm^{-3} is so similar to the results of Casey *et al.*, interpolated to $n_o = 2.4 \times 10^{18}$ cm^{-3}. As a final comparison, it is found that Casey's data interpolated to $n_o = 1.5 \times 10^{18}$ cm^{-3}, which corresponds to $N_D^+ + N_A^- \simeq 2.2 \times 10^{18}$ cm^{-3}, agrees in the absorption

Table 3.2 Mobility versus electron density measured by van der Pauw technique.

Double Heterostructure Parameters	
n_o (cm^{-3})	Mobility ($cm^2\ V^{-1}sec^{-1}$)
1.3×10^{17}	3950
3.7×10^{17}	3110
1.0×10^{18}	2500
2.2×10^{18}	1990
2.4×10^{18}	2070
3.8×10^{18}	1850

tail with these results for $n_o = 2.2 \times 10^{18}\ cm^{-3}$. The additional impurities in Casey's melt-grown material and in those with $n_o = 2.4 \times 10^{18}\ cm^{-3}$ apparently further disturbed the density of states making comparison of results as a function of free electron density difficult.

3.6 Summary and Conclusions

The absorption coefficient in the band tail in n-type GaAs was measured for a large range of electron concentration. For $\alpha(h\nu) < 3000\ cm^{-1}$ in moderately doped GaAs, these results agree with those of the classic work by Casey *et al.*, meaning that the results of these transmission experiments agree with the transmission experiments of Casey *et al.* for $n_o \leq 10^{18}\ cm^{-3}$. Casey *et al.* also noted that for n-GaAs with electron concentrations in the mid $10^{17}\ cm^{-3}$ range, $\alpha(h\nu)$ at high energies was smaller than the corresponding $\alpha(h\nu)$ of other electron concentrations. This observation is confirmed as the same occurs for these samples with $n_o = 3.7 \times 10^{17}\ cm^{-3}$, but there is as yet, no explanation for this effect. For photon energies above the bandgap energy, the results of this study as determined from transmission experiments are 20-25% greater than Casey's $\alpha(h\nu)$ which were deduced from a Kramers-Kroenig analysis. Since the $\alpha(h\nu)$ deduced here (excepting those of $n_o = 3.7 \times 10^{17}\ cm^{-3}$) approach the same value at high energies (to within

±3% at $h\nu = 1.7$ eV), and Casey's results showed similar self-agreement (±15% at $h\nu = 1.6$ eV), the relative differences at high energy between the studies are likely due to a systematic difference related to the two measurement techniques or to the two material growth methods.

For $n_o > 10^{18}$ cm^{-3}, these results for $\alpha(h\nu) < 3000$ cm^{-1} differ from the results of Casey *et al.* and this difference becomes more significant with increasing electron concentration. These differences were by compensation in Casey's melt-grown n-GaAs. Casey *et al.* expressed concern that their results did not agree with those of previous workers [7,10,11], and that those workers did not agree either, implying a sample dependence to $\alpha(h\nu)$. Although it looks as though this study may add further confusion, it is shown that compensation is likely to be responsible for many of the differences at high electron concentrations. The results of these measurements will be applied in Chapter 5 to predict spontaneous emission using the van Roosbroeck-Shockley relation before computing Einstein's B-coefficient for radiative recombination and simulating photon recycling. In addition, these comprehensive and self-consistent results should be invaluable in the analysis and simulation of opto-electronic devices such as lasers, DH's, and solar cells as well as in the more fundamental studies of band structure.

CHAPTER 4

ULTRALONG LIFETIMES IN GaAs MEMBRANES BY ENHANCED PHOTON RECYCLING

4.1 Introduction

The driving force behind our pursuit of this study has been the thin-film GaAs solar cell [56]. A thin-film GaAs solar cell is capable of achieving 35% conversion efficiency because it is detached from the substrate on which it was grown. The substrate is an absorbing layer or sink for photons emitted during radiative recombination events. The high efficiency thin-film, GaAs solar cell also requires ultralong lifetimes, $\tau_{\text{bulk}} > 1\ \mu\text{s}$, which have thus far been achieved only in nominally undoped material [15, 18, 19] unsuitable for bipolar devices. For moderately doped GaAs, however, lifetimes on the order of 1 μs are theoretically possible if photon recycling is enhanced by removing the light-absorbing substrate [57]. An ultralong lifetime is not helpful, however, if poor quality interfaces dominate recombination so it is also necessary to maintain high quality GaAs/AlGaAs interfaces as well.

This chapter reviews the observation of lifetimes greater than 1 μs in moderately doped, thin-film, n-GaAs double heterostructure membranes obtained by removing the substrate by chemical etching. The ultralong lifetimes are attributed to enhanced photon recycling [15, 20, 22, 24, 57]. Also reported is the demonstration of high-quality interfaces, with the absolute upper limit of the recombination velocity being 25 cm/s and a more accurate estimate being $S < 11$ cm/s.

4.2 Description of Experimental Techniques

Figure 4.1 shows the basic structure of the double heterostructures (DH's) grown for this study, and also shows the method of laser probing. The n—GaAs active layers were doped with selenium to a concentration of $N_D = 1.3 \times 10^{17}\ \text{cm}^{-3}$. $Al_{0.3}Ga_{0.7}As$ cladding layers, doped to $N_D = 2 \times 10^{18}\ \text{cm}^{-3}$, provide surface passivation and carrier confinement, and the $Al_{0.85}Ga_{0.15}As$ layer acts as an etch-stop [44]. An area of the substrate typically 2-3 mm in diameter was removed by wet-etching using granular citric acid dissolved in deionized water and H_2O_2 [44, 46]. (This etching process is

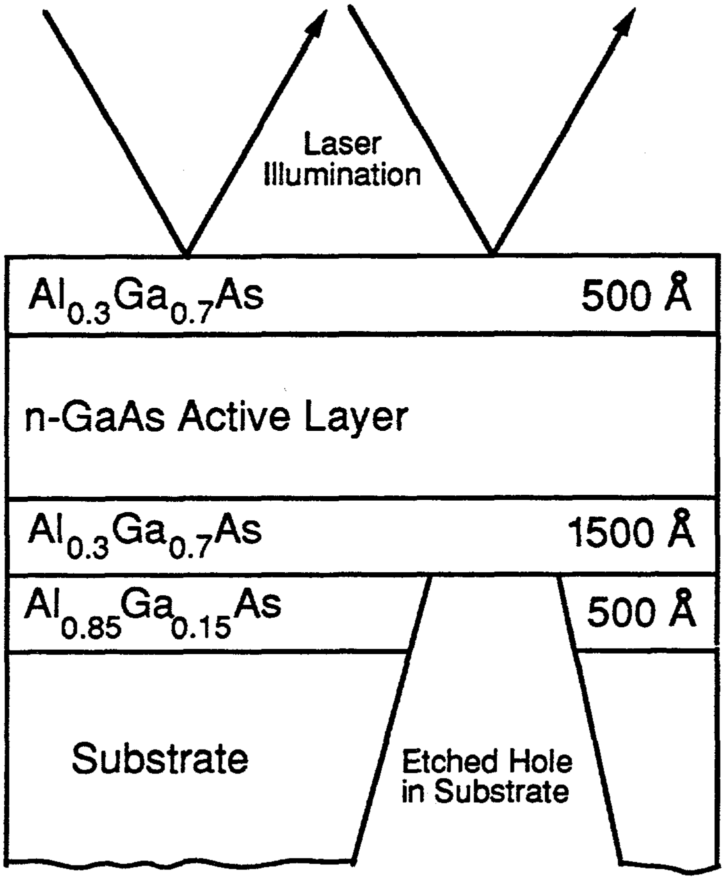

Figure 4.1 Structure of double heterostructure (DH) showing hole etched in substrate and the two locations illuminated individually by the laser.

described in greater detail in Chapter 3.) The DH membrane is therefore still attached at its periphery to the substrate which is easily handled by tweezers. As depicted in Fig. 4.1, photoluminescence (PL) decay was observed both on the membrane area and on the adjacent region where the substrate remained intact. PL decays were observed using time-correlated single-photon counting techniques described in more detail in Chapter 2. The illumination source was a 10 psec full width at half-maximum, mode-locked laser focused to a 0.8 mm diameter circle at a continuous incident power of 0.2 mW, with the exception of the 0.25 μm thick DH for which the incident power was 0.05 mW. With a repetition rate of 80 kHz, the laser generated $< 10^{16}$ carriers/cm^3, so the DH's were always in low injection. The PL spectra were observed in the same system using standard photon counting techniques.

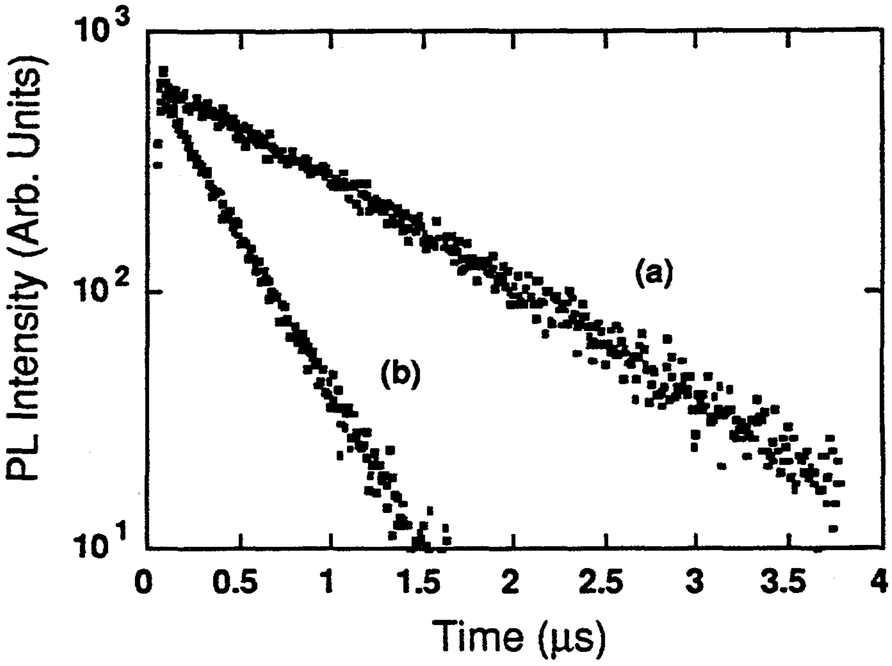

Figure 4.2 Photoluminescence decays for 5 μm DH illuminated in the two locations depicted in Fig. 4.1. Without the substrate (curve (a)), the decay constant, $\tau_{\rm DH}$, is 1.05 μs, 27 times the expected radiative lifetime. Even the DH still backed by the substrate (curve (b)) has a decay constant enhanced nearly ten times over the supposed radiative limit.

4.3 Results Showing Enhanced Lifetimes

Figure 4.2 shows the measured decays for the 5 μm DH. Without the substrate backing (curve (a)), the decay constant, $\tau_{\rm DH}$, is 1.05 μs, fully 27 times the expected radiative lifetime (38.5 ns) computed using $\tau_{\rm r} = 1/{\rm BN_D}$, where B is 2×10^{-10} cm^3/s [20, 21]. Even with the substrate intact (curve (b)), $\tau_{\rm DH}$ is 360 ns, nearly ten times the supposed radiative limit. These ultralong decay constants are due to photon recycling, the reabsorption of photons emitted during radiative recombination events [57]. Self-absorption generates new electron-hole pairs which increases the observed lifetime. The effective radiative lifetime in a DH can then be written as $\tau_{\rm eff} = \phi_{\rm r}\tau_{\rm r}$, where $\phi_{\rm r}$, Asbeck's recycling cofactor [22], is the inverse of the average probability that an isotropically emitted photon escapes the DH. Previous workers [15, 58] have

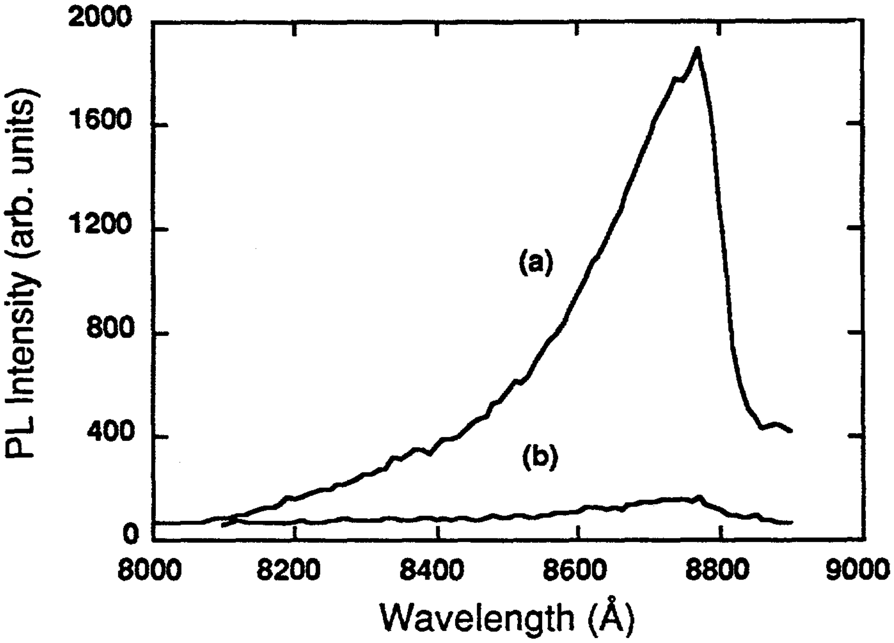

Figure 4.3 PL spectra showing the 12-fold increase in intensity exhibited by the GaAs membrane (curve (a)) over that of the region (curve (b)) still backed by the absorbing substrate.

computed $\phi_r \simeq 11$ for a 5. μm DH still attached to its substrate, which is consistent with our result, assuming that some non-radiative recombination occurs. The effective radiative lifetime of the 5 μm membrane is further enhanced over the region still attached to the substrate because the back side of the DH is now more reflective. The critical angle, Θ_{cr}, of the back interface of the DH's still attached to their substrates is about 60 °, whereas for the back of the membranes $\Theta_{cr} = 16$ ° [58]. Thus, simply removing the substrate increases ϕ_r because the isotropically emitted photons are better trapped, increasing their probability of being reabsorbed. These results demonstrate that if one is able to control non-radiative recombination, ultralong lifetimes are possible, even at this moderately high doping concentration.

4.4 Photoluminescence Spectra for 5 μm DH

Figure 4.3 shows the PL spectra for the 5 μm DH with and without the substrate intact. These spectra were observed by integrating the PL observed during several cycles of excitation and decay in the same system that the PL decay was observed. This is not a steady-state measurement. The intensity of the peak without the substrate (curve (a)) is 12 times that of the peak observed with the substrate (curve (b)). The increase in PL peak intensity is due to the decrease in Θ_{cr} for photons escaping out the back of the DH. Many photons emitted that might normally pass into the substrate are now totally internally reflected and eventually reabsorbed. The resulting electron-hole pair might later emit a photon toward the front interface during a radiative recombination event. The result of this recycling process is that there are more "opportunities" for photons to exit the front face and be detected.

4.5 Significant Enhancement of Observed Lifetimes

Figure 4.4 plots τ_{DH} versus DH thickness for all the samples, with and without substrates. There is a stronger thickness dependence to τ_{DH} for the standard DH's over τ_{DH} for the membranes because the highly reflective interfaces in the membranes trap most of the photons, so the probability of being reabsorbed is essentially independent of DH thickness. Therefore, ϕ_r is more strongly dependent on the critical angle of the interfaces than on DH thickness, w. For the standard DH's, ϕ_r is a stronger function of w because the back interface is less reflective so an average photon in a thicker DH is more likely to be reabsorbed BEFORE reaching the largely transparent back interface, as compared to a photon in a thinner DH. These considerations explain why the enhancement factor, defined as τ_{DH} without the substrate divided by τ_{DH} with the substrate for the same thickness, steadily increases with decreasing DH thickness.

Note that the decay constant for the 10 μm membrane is clearly shorter than would be expected when compared to the other data points. This sample was damaged during the etching process. As evidence note that the τ_{DH} of the 10 μm DH with the substrate (395 ns) is significantly shorter than that which was measured previously (465 ns: reported in Chapter 2.)) on a different area of the wafer. The reduced non-radiative lifetime in this sample limits the enhancement of τ_{DH}.

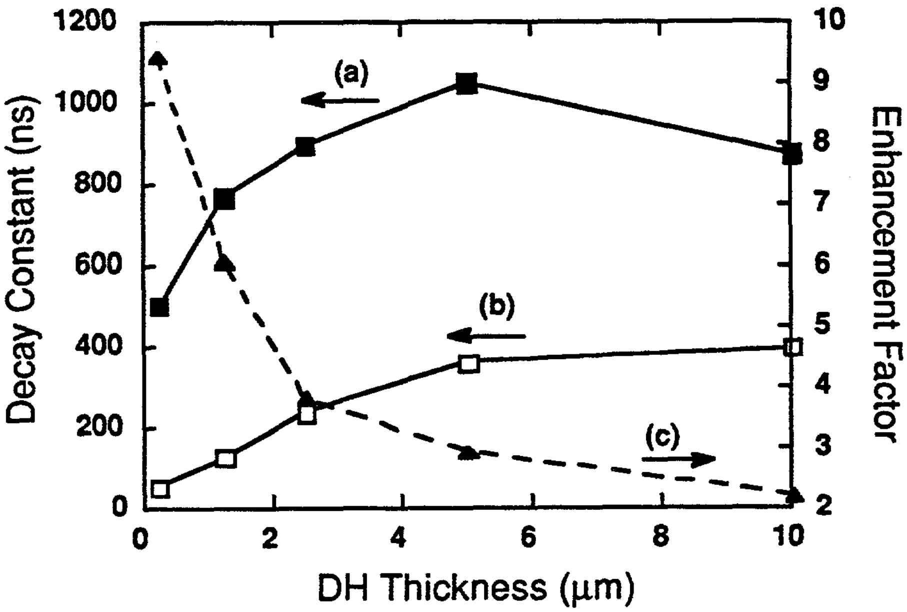

Figure 4.4 DH decay constants versus DH thickness, with (curve (b)) and without (curve (a)) the substrate. Under both circumstances, τ_{DH} increases with increasing thickness due both to stronger self-absorption in thicker DH's and to the decreasing contribution from the interfaces to the total recombination. Also shown (curve (c)) is the enhancement of τ_{DH}, defined as the thin-film decay constant divided by the decay constant observed with the substrate intact.

4.6 Very Low Interface Recombination Velocity

The long lifetimes observed in thin films make it easier to deduce the interface recombination velocity because interface recombination is more important than it was with the substrate intact. If $\mathrm{Sw/D} < 1$, where D is the minority carrier diffusivity, recombination in a DH can be described by [30, 31]

$$\frac{1}{\tau_{\mathrm{DH}}} = \frac{1}{\tau_{\mathrm{bulk}}} + \frac{2\mathrm{S}}{\mathrm{w}}, \tag{4.1}$$

where τ_{bulk} is the bulk lifetime. One can obtain an upper limit to the interface recombination velocity, S, by attributing all the recombination of the thinnest DH membrane to the interfaces. In this case $\mathrm{S} = \mathrm{w}/2\tau_{\mathrm{DH}}$, and since for the

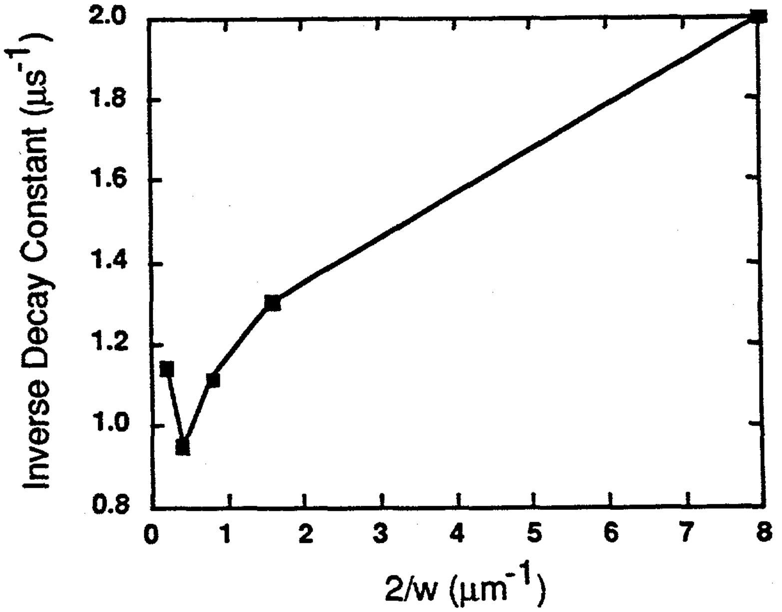

Figure 4.5 Plot of $1/\tau_{DH}$ versus 2/w for the DH's membranes. The slope of the plot yields an interface recombination velocity of less than 12 cm/s.

0.25 μm DH, $\tau_{DH} = 500$ ns, the upper limit of S is 25 cm/s. One can obtain a more accurate value of S by plotting $1/\tau_{DH}$ vs. 2/w, as shown in Fig. 4.5. Equation 1 suggests that the data in such a plot should lie on a straight line with slope S. However, τ_{bulk} changes with w due to photon recycling so plots of $1/\tau_{DH}$ vs. 2/w always display negative curvature when the material is dominated by radiative recombination and photon recycling [59]. A least-squares fit to the data points of the three thinnest DH membranes yields $S \leq 12$ cm/s, while a line drawn through the points representing the two thinnest DH membranes has a slope that yields $S \leq 11$ cm/s. These numbers are more accurate estimates for the interface recombination velocity.

4.7 Summary

In summary, lifetimes longer than 1 μs are observed in thin-film GaAs double heterostructure membranes with active regions doped to $N_D =$

1.3×10^{17} cm^{-3}. These ultralong lifetimes are possible because of a combination of enhanced photon recycling produced by the removal of the backing substrate and minimal non-radiative recombination in the bulk and at the interfaces. An absolute upper limit of $S = 25$ cm/s was deduced for the interface recombination velocity, but a more reasonable estimate is $S < 11$ cm/s. Such long lifetimes suggest that thin-film GaAs solar cells designed to enhance photon recycling may represent a viable way of achieving higher cell efficiencies.

CHAPTER 5

THE RELATIONSHIP BETWEEN ABSORPTION AND EMISSION AND THE COMPUTATION OF THE B-COEFFICIENT IN N-TYPE GaAs

5.1 Introduction

Chapters 2 and 3 presented the results of recombination and absorption experiments, respectively, and in Chapter 1 the van Roosbroeck-Shockley (vR-S) relation, which relates recombination and absorption, was derived. In this chapter we examine experimentally the validity of the vR-S relation by comparing steady-state photoluminescence (SSPL) to the spectra predicted by vR-S using the $\alpha(h\nu)$ data presented in Chapter 3. A favorable comparison is made between theory and experiment, and this justifies using Eq. (1.17) to compute the B-coefficient. A second method of computing B is to use the observed decay constants of Chapter 2 and deduce B using a computer model for photon recycling. Although at first glance the results from these two methods of computing B do not appear to be compatible, they are found to be in relative agreement, especially after accounting for possible uncertainties in the $p_o n_o$ product and in other parameters. The analysis and results of this chapter demonstrate the validity of the predicted relationship between recombination and absorption, and this should lend credibility to the values of B calculated.

5.2 Steady-state Photoluminescence and van Roosbroeck-Shockley

According to van Roosbroeck and Shockley, the normalized emission spectra for a semiconductor in low-injection can be written as [5],

$$\hat{R}_{spon}(h\nu) = \frac{\gamma_{bb}(h\nu)\alpha(h\nu)v_g(h\nu)}{R_{spon}(h\nu_{peak})}, \tag{5.1}$$

where $\hat{R}_{spon}(h\nu)$ represents the normalized photon energy dependence of spontaneous emission, $\gamma_{bb}(h\nu)$ is the black-body radiation, $\alpha(h\nu)$ is the absorption coefficient, and $v_g(h\nu)$, the group velocity, is the velocity of light for a photon of energy $h\nu$. In a weakly dispersive medium $v_g = c/n$, where c is the

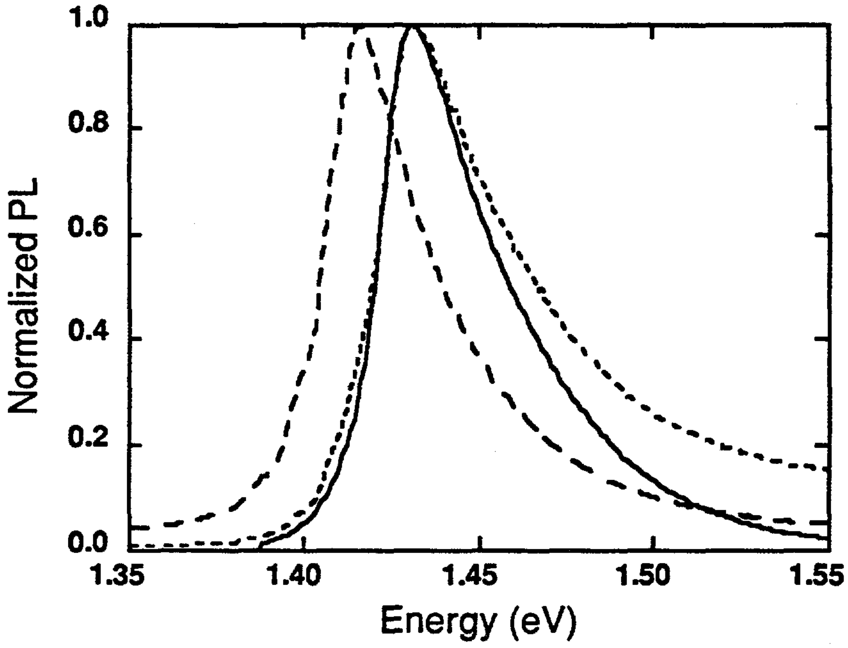

Figure 5.1 Comparison of SSPL and spontaneous emission for the 10 μm DH with $n_o = 1.3 \times 10^{17}$ cm^{-3}. The solid line is the spontaneous emission predicted by the van Roosbroeck-Shockley relation, the long-dashed line is the observed SSPL, and the short-dashed line is the deduced spontaneous emission after accounting for self-absorption. The predicted spontaneous emission matches that deduced from SSPL.

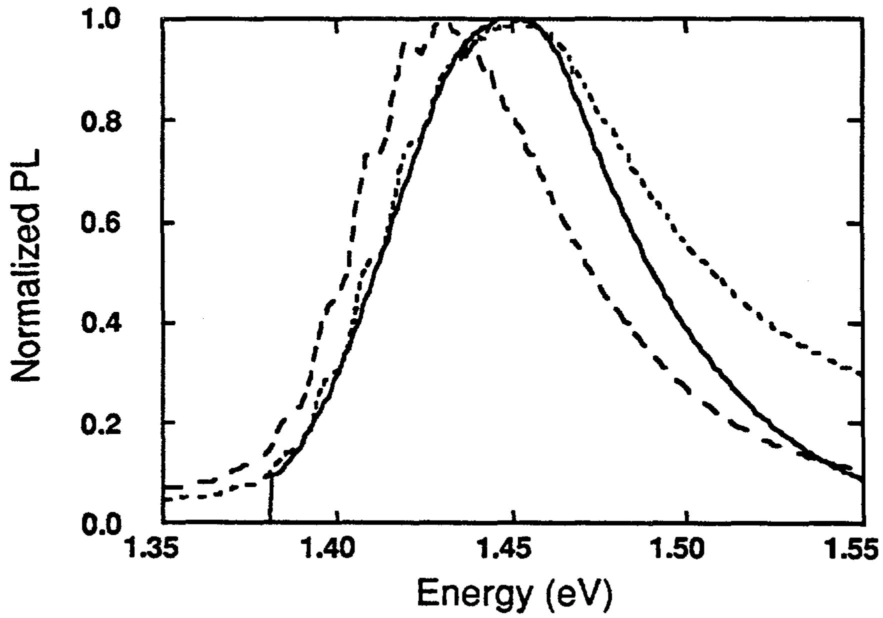

Figure 5.2 Comparison of SSPL and spontaneous emission for the 10 μm DH with $n_o = 2.2 \times 10^{18}$ cm^{-3}. The solid line is the spontaneous emission predicted by the van Roosbroeck-Shockley relation, the long-dashed line is the observed SSPL, and the short-dashed line is the deduced spontaneous emission after accounting for self-absorption. The predicted spontaneous emission matches that deduced from SSPL

speed of light in a vacuum and data for n, the index of refraction, are available for GaAs [39,60] and undoped $Al_xGa_{1-x}As$ [39,47]. (Equation (5.1) is equivalent to Eq. (1.16) which was derived in Sec. 1.3.) Equation (5.1) will not necessarily describe the observed SSPL, however, because self-absorption can distort the spectra. For a DH of thickness w, the SSPL will be proportional to,

$$\mathrm{SSPL}(h\nu) \propto \int_0^w \hat{R}_{spon}(h\nu)p(x)n(x)e^{-\alpha(h\nu)x}dx, \tag{5.2}$$

where p(x) and n(x) are the position-dependent hole and electron concentrations, respectively. (For details of how p(x) and n(x) are determined, see Appendix A.) For uniform carrier concentrations, Eq. (5.2) reduces to

$$\mathrm{SSPL}(h\nu) \propto \hat{R}_{spon}(h\nu)(1 - e^{-\alpha(h\nu)w}). \tag{5.3}$$

Low-injection SSPL was measured for 0.25 and 10 μm DH's with electron concentrations $n_o = 1.3 \times 10^{17}$ and 2.2×10^{18} cm^{-3}. Figure 5.1 shows the measured SSPL for the 10 μm DH with $n_o = 1.3 \times 10^{17}$ cm^{-3}. The $\hat{R}_{spon}(h\nu)$ as deduced from the SSPL using Eq. (5.2) to account for self-absorption and the spectrum calculated from the vR-S relation are also displayed. Figure 5.1 shows clearly the shift of the emission peak due to self-absorption. It is also clear that the $\hat{R}_{spon}$ deduced from SSPL matches very closely the $\hat{R}_{spon}$ predicted using the vR-S relation. The apparent discrepancy at high photon energies in Figs. 5.1 and 5.2 is an artifact of the experiment. There is a constant level of background noise which becomes a significant part of the observed signal for high and low energy photons where the amount of emission is low compared to the peak intensity. The background noise is amplified for high photon energies which are strongly self-absorbed. The effect is more pronounced for the 10 μm DH with $n_o = 2.2 \times 10^{18}$ cm^{-3} because the peak intensity is reduced due to a shorter lifetime and lower internal quantum efficiency.

Figure 5.2 compares the different spectra for the 10 μm DH with $n_o = 2.2 \times 10^{18}$ cm^{-3}. Again the vR-S relation is proven valid. Comparing the two figures, the magnitude of the peak shift due to self-absorption is smaller for $n_o = 2.2 \times 10^{18}$ cm^{-3} because $\alpha(h\nu)$ is smaller at the peak of the $\hat{R}_{spon}$, than is $\alpha(h\nu)$ for the corresponding peak of emission of the DH with $n_o = 1.3 \times 10^{17}$ cm^{-3}. (See Fig. 3.7 in Chapter 3). The SSPL of the 0.25 μm DH's behaves a little differently.

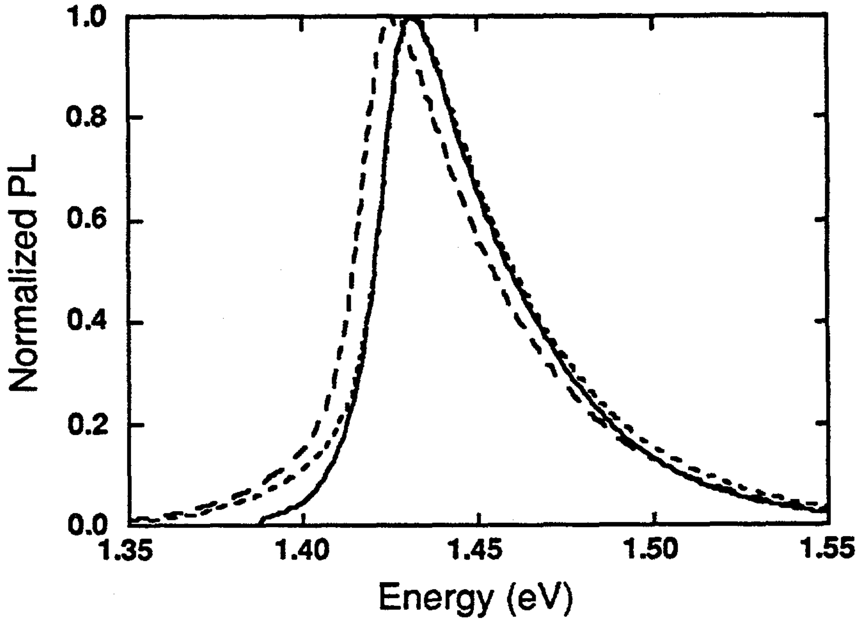

Figure 5.3 Normalized SSPL and the $\hat{R}_{\text{spon}_3}$ computed from Eq. (5.1) for the 0.25 μm DH with $n_o = 1.3 \times 10^{17}$ cm^{-3}. It is clear that the SSPL agrees with the vR-S relation, but only after a rigid shift of 6 meV toward the higher frequency photons.

Figure 5.3 shows the measured SSPL and the predicted spontaneous emission spectrum computed from Eq. (5.1) for the 0.25 μm DH with $n_o = 1.3 \times 10^{17}$ cm^{-3}. (Self-absorption is negligible in these thin DH's.) Also shown is the SSPL after a rigid shift of 6 meV toward the higher frequency photons. It is clear that the SSPL agrees with the vR-S relation, but only after this rigid shift. The shift necessary for the 0.25 μm DH with $n_o = 2.2 \times 10^{18}$ cm^{-3} is 12 meV, so we are observing a real effect which may be doping dependent.

If this rigid shift were due solely to heating of the lattice, a nearly 14 °C increase in temperature would be required. Additionally, the SSPL of the 0.25 μm DH with $n_o = 1.3 \times 10^{17}$ cm^{-3} was measured with the laser power varying from 10 μW to 10 mW, and no change in the observed spectra was observed. The intensity independence eliminates both heating and high-injection effects as possible explanations for the peak shifts. At the peak of the emission, the wavelength of the photons is nearly 0.87 μm in free space. With an index of refraction for GaAs of about 3.6, the peak-wavelength inside the DH's is about 0.24 μm, a length comparable to the thickness of the thinnest DH's. The derivation of Eq. (1.5), which represents $\gamma_{bb}(h\nu)$, assumes an infinite semiconductor when computing the optical density of modes [4]. Since the wavelengths observed are on the order of the DH thickness, one could propose that the density of modes is different in the thinnest DH's. The optical confinement of a GaAs/AlGaAs interface is rather weak, however, with $R \simeq 0.01$ and $\Theta_{cr} \simeq 60^\circ$ so the DH is not independent of the semi-infinite substrate.

The indication of a doping dependence for the magnitude of the shift suggests that this may be related to the doping dependence of the interference oscillations observed in the transmission experiments of Chapter 3. These oscillations are also observed on a smaller scale in the emission tail of the SSPL of the 10 μm DH (Fig. 5.2). More detailed studies are needed to understand these phenomena. Despite this anomaly in the 0.25 μm DH's, most of our DH's have thicknesses greater than ten times the wavelengths of the emission peaks, and Figs. 5.1 and 5.2 showed that the vR-S relation describes the emission quite well for the 10 μm DH's. It is therefore still of strong interest to use Eq. (1.17) to compute B.

5.3 Computing the B-coefficient

5.3.1 Previous Estimates of the B-coefficient

The B-coefficient is one of the most important parameters needed in the modeling of GaAs minority carrier devices such as solar cells, light-emitting diodes, and lasers. (In most cases, however, knowledge of B alone is not sufficient because photon recycling effects are strong.) Previous workers have attempted to calculate B quantum mechanically [21, 25, 61], using detailed balance arguments [5, 25, 62], and to estimate it directly from observed minority carrier lifetime measurements [16, 20, 63]. The published values of B, however, have varied over more than an order of magnitude. This previous work concentrated on p-type and nominally undoped GaAs because the material quality in n-type GaAs has made study of intrinsic recombination difficult. The present work is the most self-consistent effort for n-GaAs, because most all the parameters used were measured on a single set of wafers.

5.3.2 Detailed Balance Calculations

In Section 1.3 detailed balance arguments were used to derive Eq. (1.22) repeated here for convenience:

$$Bn_o = \frac{1}{\tau_r} = \frac{1}{p_o}\int_0^\infty \gamma_{bb}(h\nu)\alpha(h\nu)v_g(h\nu)d(h\nu) = \frac{G}{p_o}. \tag{5.4}$$

The integral on the right hand side (RHS) of Eq. (5.4), labeled G after Casey and Stern [25] is evaluated using the data for $\alpha(h\nu)$ from Chapter 3 and Sell's data for the index of refraction [60]. Since $\alpha(h\nu)$ was measured at $T = 292$ K (see Chapter 3), the band edge is shifted rigidly such that $\Delta E_g = -4$ meV. (This was also done before predicting the expected spontaneous emission in Section 5.2 as the SSPL was observed at $T = 295$ K.) The value of ΔE_g was deduced as $\simeq 0.5$ eV/K near $T = 300$ K from the temperature-dependent $\alpha(h\nu)$ measured by Sturge [53].

Table 5.1 Listing of G, n_{ie}, and B computed at T=300 K for each of the five electron concentrations studied. Note that B is nearly constant with an average value of $B = 4.4 \times 10^{-10}$ cm^3/s.

n_o (cm^{-3})	G (cm^{-4} s^{-1})	n_{ie} ($\times 10^6$) (cm^{-3})	B($\times 10^{-10}$) (cm^3/s)
1.3×10^{17}	4260	3.1	4.5
3.7×10^{17}	3670	2.9	4.4
1.0×10^{18}	2660	2.5	4.1
2.2×10^{18}	1860	2.1	4.3
3.8×10^{18}	1310	1.7	4.6

Table 5.1 lists the values of G evaluated using Eq. (5.4). It is found that G decreases significantly with increasing n_o; this decrease is due to the Burstein shift [51], the effective widening of the optical bandgap due to the filling of conduction band states. An effective widening of the bandgap suppresses absorption and, by detailed balance, recombination as well.

Finally, to compute B using Eq. (5.4), one must know the $p_o n_o$ product. Figure 5.4 shows recent data for the $n_{ie}^2 D_p$ product [66], and Fig. 5.5 plots data

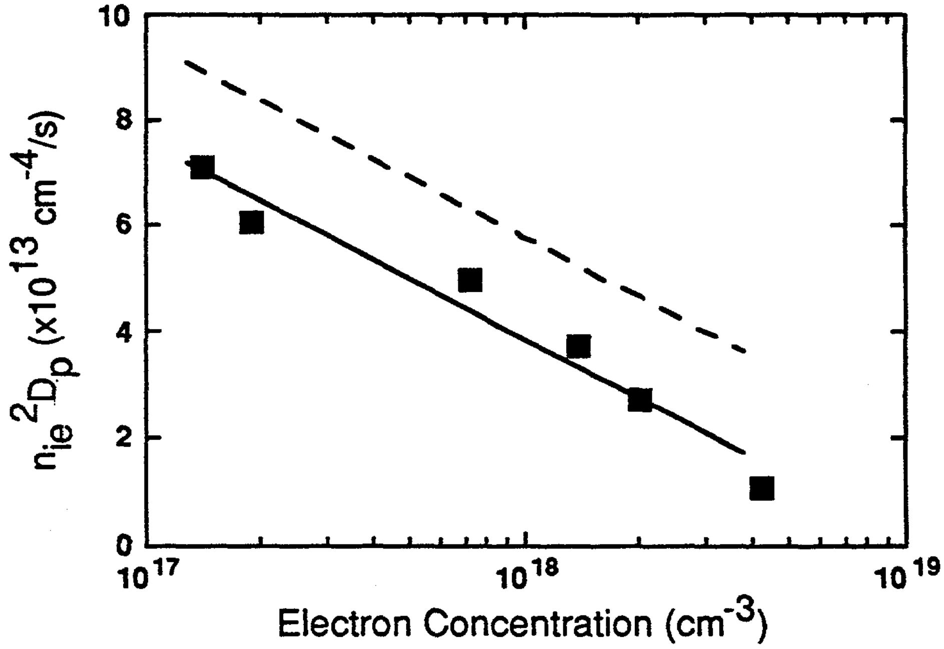

Figure 5.4 Recent data for the $n_{ie}^2D_p$ product. (The data point for the highest n_o has been changed from that reported in Ref. 65 because of a recent correction to n_o for that data point [64]). The solid line is the logarithmic least-squares fit to the data. The broken line is discussed in Section 5.3.4.

for D_p [65], where $n_{ie}^2 = p_o n_o$ and D_p is the minority carrier diffusivity. These measurements were performed in GaAs grown by MBE and doped with silicon. Because of the slight scatter in the data, a logarithmic least-squares fit to the data is done which yields the function,

$$n_{ie}^2 D_p = 7.08 \times 10^{14} - 3.72 \times 10^{13} \log(n_o) \ \ cm^{-4}/s. \qquad (5.5)$$

The solid line in Fig. 5.4 shows the fit represented by Eq. (5.5). D_p was determined by linear interpolation between the available data points.

Table 5.1 lists G, n_{ie}, and B for each of the five electron concentrations studied and indicates that B is nearly constant with an average value of $B = 4.4 \times 10^{-10}$ cm^3/s. A constant B-coefficient is somewhat surprising because previous efforts had shown B to decrease with increasing concentration in both

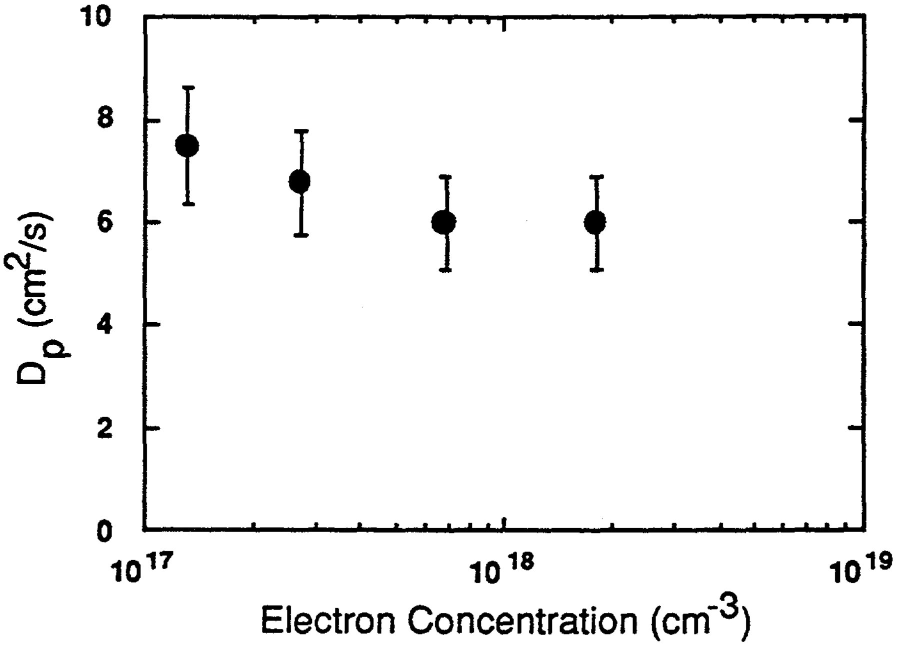

Figure 5.5 Recent data for D_p [65]. The uncertainty was estimated to be 15%.

n-type [9,14] and p-type [20,25,61] GaAs. It is possible that uncertainty in $n_{ie}^2 D_p$ has led to incorrect results for B. After the following section where B is estimated from lifetime measurements, it will be shown that reasonable uncertainty in $n_{ie}^2 D_p$ can significantly impact the behavior of B versus n_o.

5.3.3 B Estimated From Lifetime Measurements

Under easily attainable conditions, the decay constant of a DH can be written as [30,32]

$$\frac{1}{\tau_{DH}} = \frac{1}{\tau_r \phi_r} + \frac{1}{\tau_{nr}} + \frac{2S}{w} \tag{5.6}$$

where S is the interface recombination velocity, w is the DH thickness, τ_{nr} is the non-radiative lifetime, and τ_r is the radiative lifetime. Asbeck's photon recycling cofactor, ϕ_r, is the inverse of the probability that a photon escapes the active region of a DH. This is calculated using a variation of Kuriyama's formula [24], which allows photons to reflect off the interfaces up to ten times before being reabsorbed. (See Appendix A.) Kuriyama accounted for reflections off the front interface only. The lifetime data are taken from the study described in Chapter 2. Since in Chapters 2 and 3 interface recombination was found to be negligible in these DH's, the last term in Eq. (5.6) can be ignored. Equation (5.6) then suggests that plotting $1/\tau_{\mathrm{DH}}$ vs. $1/\phi_{\mathrm{r}}$ for the series of DH thicknesses will generate a line, the intercept of which is $1/\tau_{\mathrm{nr}}$ and the slope of which is $1/\tau_{\mathrm{r}}$. Since $1/\tau_{\mathrm{r}} = \mathrm{Bn_o}$, we can determine B from the slope.

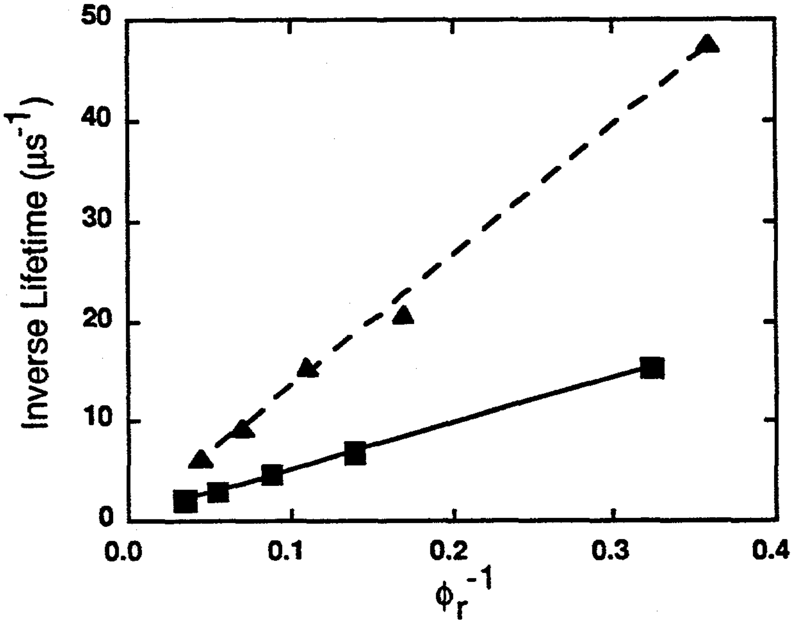

Figure 5.6 Plot of $1/\tau_{\mathrm{DH}}$ vs. $1/\phi_{\mathrm{r}}$ for the lowest two electron concentrations under low intensity excitation. These plots are both linear yielding values for B and for τ_{nr} that are listed in Table 5.2.

Figure 5.6 plots $1/\tau_{\mathrm{DH}}$ vs. $1/\phi_{\mathrm{r}}$ for the lowest two electron concentrations under low intensity excitation. The plots are nicely linear, yielding distinct values for B and τ_{nr} which are listed in Table 5.2. The extremely long τ_{nr} for $\mathrm{n_o} = 3.7 \times 10^{17}\ \mathrm{cm}^{-3}$ is thought to be due to the difficulty in determining accurately the value of such a small-valued intercept. A fit to the line formed by the four thickest DH's with $\mathrm{n_o} = 3.7 \times 10^{17}\ \mathrm{cm}^{-3}$ yields $\tau_{\mathrm{nr}} = 630$ ns.

For $\mathrm{n_o} \geq 10^{18}\ \mathrm{cm}^{-3}$, the plots become increasingly less linear because the effective τ_{nr} increases with decreasing DH thickness as shown in Fig. 5.7. The

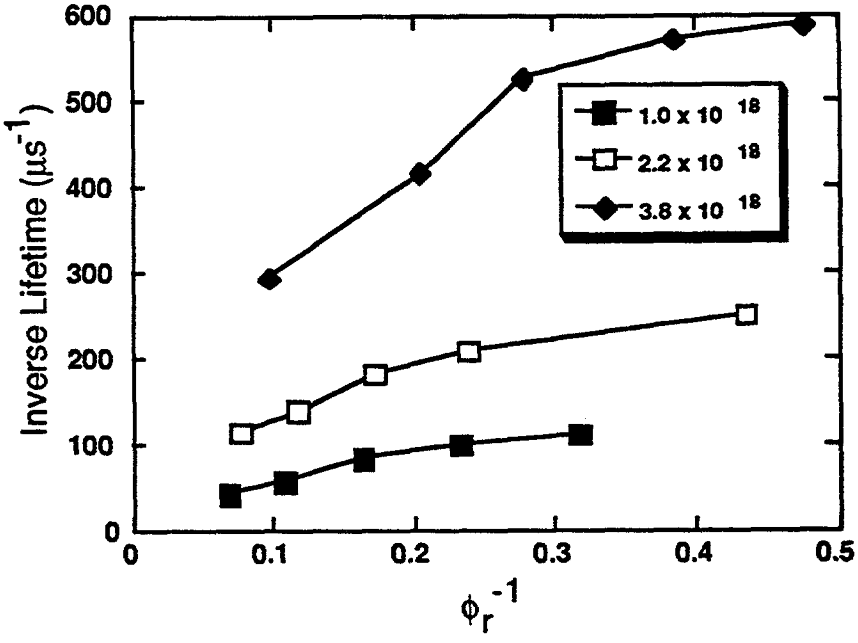

Figure 5.7 Plot of $1/\tau_{DH}$ vs. $1/\phi_r$ for $n_o > 10^{18}$ cm^{-3}, under low intensity excitation. These plots are all non-linear due to varying degrees of saturation of SRH recombination centers and so do not yield unique values of B and τ_{nr}.

increase of τ_{nr} occurs as the SRH recombination centers become more saturated with decreasing DH thickness. Equation (2.6) described the SRH recombination rate as

$$R = \frac{\Delta p}{\frac{\Delta p}{n_o}\tau_n + \tau_p} \tag{5.7}$$

where Δp is the excess carrier concentration. A given laser pulse power level will generate a higher initial average hole concentration in a thinner DH than the same power level in a thicker DH. The initial Δp is increased, so the effective τ_{nr} is increased. For the thinner DH's, the laser power was not sufficiently reduced, leading to a higher initial excess hole concentration. This analysis would be more valid, therefore, if each DH had its SRH centers fully saturated. For this reason, the decay constants under high laser excitation were used to plot $1/\tau_{DH}$ vs. $1/\phi_r$ for the DH's with $n_o \geq 10^{18}$ cm^{-3}. The high-intensity data are listed in Table 5.3.

Table 5.2 The B-coefficient and τ_{nr} for each of the five electron concentrations studied.

n_o (cm^{-3})	$B(\times 10^{-10})$ (cm^3/s)	τ_{nr} (ns)	Laser Intensity
1.3×10^{17}	3.5	1700.	Low
3.7×10^{17}	3.5	3700.	Low
1.0×10^{18}	2.6	39.	High
2.2×10^{18}	2.0	17.	High
3.8×10^{18}	1.8	5.8	High

Table 5.3 High-intensity decay constants for the DH's with $n_o \geq 10^{18}$ cm^{-3}.

n_o (cm^{-3})	[Targeted DH Thicknesses (μm)] Measured DH Decay Constants (nsec)				
1.0×10^{18}	[0.5] 10.	[1.0] 11.	[2.0] 13.	[4.0] 19.	[8.] 29.
2.2×10^{18}	[0.25] 4.0	[1.25] 5.8	[2.5] 7.0	[5.0] 9.3	[10.] 11.3
3.8×10^{18}	[0.25] 2.0	[0.5] 2.3	[1.25] 2.6	[2.5] 3.4	[10.] 4.1

Figure 5.8 shows the plots of $1/\tau_{DH}$ vs. $1/\phi_r$ under high intensity for the DH's with $n_o \geq 10^{18}$ cm^{-3}. These plots are all linear yielding values for B and for τ_{nr} that are listed in Table 5.2. Table 5.2 shows that B decreases significantly with increasing n_o, in contrast to what was found for B computed by detailed balance calculations in Section 5.3.2.

It is difficult to compare these results to previous efforts to compute B because so little has been done in n-type GaAs. Garbuzov found $B \simeq 2.0 \times 10^{-10}$ cm^3/s for $n_o \simeq 10^{18}$ cm^{-3} [14], but Hwang found that τ_r actually increased for $n_o > 2.0 \times 10^{18}$ cm^{-3} [9]. Nelson and Sobers deduced

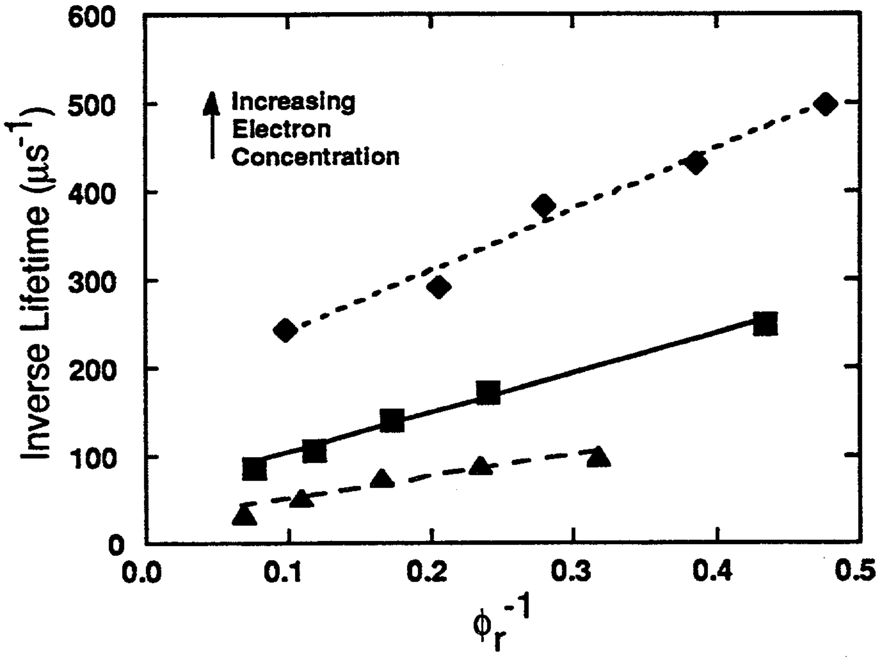

Figure 5.8 Plot of $1/\tau_{DH}$ vs. $1/\phi_r$ for the DH's with $n_o \geq 10^{18}$ cm^{-3}. These plots are all linear yielding values for B and for τ_{nr} that are listed in Table 5.2.

$B = 3.7 \times 10^{-10}$ cm^3/s for nominally undoped p-GaAs, in good agreement with the values reported here for $n_o = 1.3 \times 10^{17}$ cm^{-3} [20]. No other valid comparisons are available to author's knowledge.

5.3.4 Effects of Uncertainty in Estimating B

Since all the parameters for estimating B from the lifetime measurements and photon recycling were determined using the same set of wafers, more confidence should be placed in those results. The uncertainty in B calculated from lifetime measurements is estimated at <20% by combining the possible errors propagating from measuring n_o (< 10%), w (10%), α ($\simeq$ 5%), and τ_{DH} (10%).

Estimating the uncertainty in B as calculated from the vR-S relation is more difficult. The $n_{ie}^2 D_p$ product is deduced from the measured collector current, I_C, versus emitter-base voltage, V_{EB}, characteristic of a p-n-p homojunction transistor [66]. A line is fit to the I_C—V_{EB} semi-log plot in the region where the ideality factor of the characteristic is 1; this is typically in the range $0.7 \leq V_{EB} \leq 0.9$ volt. The intercept of the fit, I_o, is written as

$$I_o = q A_E \frac{n_{ie}^2 D_p}{n_o W_B} \quad \text{Amps}, \tag{5.7}$$

where q is the electronic charge, A_E is the area of the emitter, and W_B is the width of the base. The electron concentration is found from Hall measurements. The first source of uncertainty is in mathematically determining the intercept. It is clear that the intercept decreases with increasing n_o; this decrease is made more significant since it was found that $n_{ie}^2 D_p$ decreased nearly seven-fold over the range of n_o studied [66]. Any uncertainty inherent in mathematically determining the intercept, therefore, will increase with increasing n_o. An illustration of the potential for such uncertainty is found in Section 5.3.3 where the deduced value of τ_{nr} for $n_o = 3.7 \times 10^{17}$ cm^{-3} varied by a factor of six after changing the number of data points used for a least-squares fit to $1/\tau_{DH}$ vs. $1/\phi_r$. Uncertainty in determining the intercept would come mainly from uncertainty in the temperature. Patkar *et al.* experimentally deduced temperatures within 0.5 K of the thermocouple reading for most devices [66]. Using the values of $I_C = 10^{-8}$ Amp and $V_{EB} = 0.85$ volt for the sample with the highest n_o (Fig. 2 in Ref. 65), an uncertainty of $\Delta T = 0.5$ K yields 5% uncertainty in I_o. The sensitivity increases exponentially, however, and the uncertainty would be 30% if $\Delta T = \pm 1$ K.

Once the intercept is obtained, uncertainty in W_B (10%) and D_p (15%) [65] can lead to error in deducing n_{ie}^2. Uncertainty in n_o as determined by Hall measurements doubly affects the plot of $n_{ie}^2 D_p$ vs. n_o because both the abscissa (n_o) and the ordinate ($n_{ie}^2 D_p$) are proportional to n_o. For instance if 10% uncertainty in n_o is assumed, which is the minimum expected for Hall measurements, the corresponding uncertainty in $n_{ie}^2 D_p$ would be about 12% for $n_o \simeq 10^{17}$ cm^{-3} and 20% for $n_o \simeq 4 \times 10^{18}$ cm^{-3}. Again, the uncertainty increases with increasing n_o.

Finally, in Ref 65 the data for $n_{ie}^2 D_p$ were scaled to 300 K for each n_o, using the expected temperature dependence of n_i in intrinsic GaAs. Although the necessary temperature shifts were small, the $n_{ie}^2 D_p$ product is exponentially dependent on temperature so even a small temperature shift is significant. One would expect this uncertainty to again increase with increasing n_o since a higher doping concentration is even less like intrinsic GaAs.

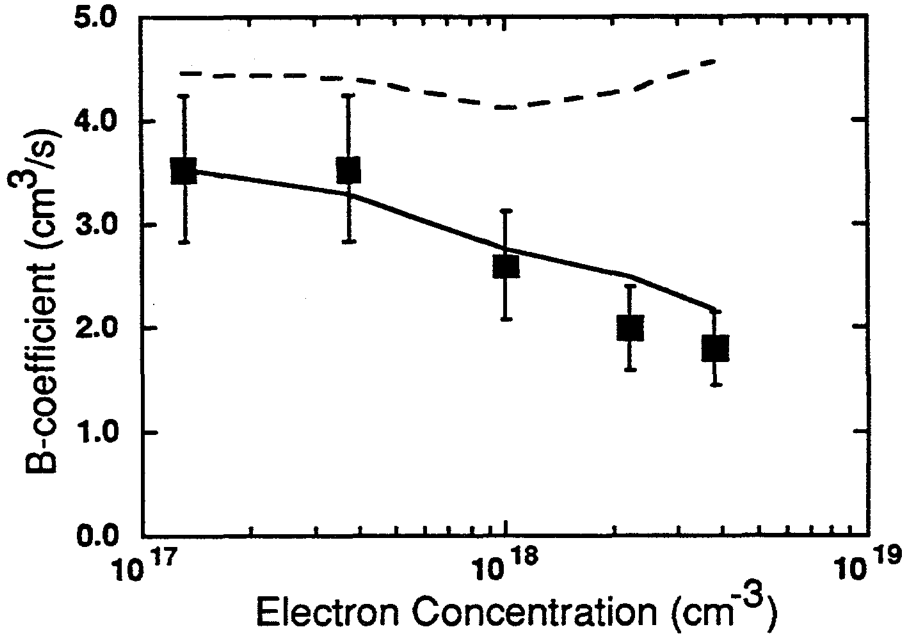

Figure 5.9 Comparison of B as computed by all three methods at T=300 K. The broken line is B as computed by detailed balance in Section 5.3.2, the square data points represent B as computed from lifetime measurements, and the solid line is B calculated in this section. The uncertainty in B calculated from lifetime measurements is estimated at ≃ 20%.

To get an idea of how this uncertainty can affect the observed behavior of B vs. n_o, Eq. (5.5) is altered keeping the same coefficient of the logarithm, but changing the intercept constant to 7.27×10^{14} cm^{-4}/s. (This specific value was chosen in order that B calculated by the two methods would be equal for $n_o = 1.3 \times 10^{17}$ cm^{-3}.) This small change in Eq. (5.5) is represented by the broken line in Fig. 5.4. Figure 5.9 compares the values of B computed by all three methods. The broken line is B as computed by detailed balance in Section 5.3.2, the square data points represent B as computed from lifetime measurements, and solid line is B calculated in this section.

Clearly the observed behavior of B changes significantly, and it decreases with increasing n_o, mirroring the trend observed from the lifetime measurements. For this exercise, the value of $n_{ie}^2 D_p$ changes by 25% for $n_o = 1.3 \times 10^{17}$ cm^{-3} and by a factor of two for $n_o = 3.8 \times 10^{18}$ cm^{-3}. It is hard to assess whether 100% error is likely, but we have established a minimum uncertainty of 30% for the highest n_0.

5.4 Summary and Conclusions

It was shown that the SSPL in thick samples of GaAs is well-modeled using the vR-S relation for a wide range of degenerately doped n-GaAs, verifying the theoretically developed relationship between absorption and recombination. However, an anomalous rigid shift in the SSPL of the thinnest DH's suggests that further studies of these DH's are needed. The radiative B-coefficient was then estimated using the vR-S relation and directly from lifetime measurements on n-type GaAs with $1.3 \times 10^{17} \leq n_o \leq 3.8 \times 10^{18}$ cm^{-3}. The two methods produced different trends of B vs. n_o and values that differed by as much as a factor of two. We showed, however, that the direct evaluation of B from the vR-S relation is subject to large uncertainty in the value of n_{ie}, while we believe that B as calculated from lifetime measurements is accurate to within 20%. Indeed, given that previous estimates for B vary by more than an order of magnitude, it is surprising that our estimates, obtained by two different methods, agree to within 50% or less. These results should be of great interest to those working in the characterization and modeling of opto-electronic GaAs devices.

CHAPTER 6

CONCLUSIONS AND PATHS OF FUTURE WORK

6.1 Summary and Conclusions

The results from this comprehensive study of n-type GaAs fills what had been a void of understanding of recombination and absorption in high-quality crystals. It is concluded that radiative recombination is much more important in MOCVD material, while SRH recombination dominated for most concentrations in LPE- and melt-grown n-GaAs. The absorption studies showed qualitative similarities to the oft-cited work of Casey *et al.* [10] and quantitative similarities in the Urbach tails at low n_o. But differences in the absorption tails increased with increasing n_o, and these differences were attributed to compensation in the material of Casey *et al.* Recombination and absorption were shown experimentally to be directly related, as the van Roosbroeck-Shockley relation (using the α reported herein) predicted the lineshape of PL spectra. This allowed computation of the B-coefficient by two methods yielding comparable results.

The motivation behind this work is the pursuit of a thin-film GaAs solar cell [56], though the knowledge gained is shared with all areas of GaAs minority-carrier device modeling. The success of the thin-film cell depends primarily on the ability to grown high-quality crystals that do not suffer from significant non-intrinsic recombination. The ultra-long lifetimes discussed in Chapter 4 demonstrate that enhanced photon recycling can lead to >1 μs lifetimes even in moderately doped GaAs. Interface recombination was also found to be well-controlled as the $S \leq 11$ cm/s observed is extraordinarily low for an AlGaAs/GaAs interface. These results support the viability of the thin-film solar cell. Also, the proven validity of the van Roosbroeck-Shockley relation allows a numerical model of photon recycling, which is needed to predict and characterize solar cell performance.

This is the first comprehensive effort on high-quality GaAs wherein all optical and recombination measurements were performed on the same wafers. The self-consistency of the results should instill great confidence in their applicability to the work of device modelers and semiconductor physicists.

6.2 Future Work

6.2.1 Recombination in p-type GaAs or other compound materials

The most obvious area of future work is to conduct a similar comprehensive study in high-quality p-type GaAs, or in another compound semiconductor such as InP or InGaAs. Although recombination and absorption in p-type GaAs are believed to be well-understood, some results from this study suggest otherwise. The α data reported here for n-type GaAs differs significantly from that of Casey *et al.*, especially in the regime where compensation was important. Casey's p-GaAs was similarly compensated so it should be expected that a study of MOCVD p-GaAs will reveal significant differences in α. Previous detailed-balance calculations of B in p-type GaAs [25] are therefore suspect, as are calculations of ϕ_r, both of which are based on α. Consistent experimental data show that the minority carrier lifetime in p-GaAs can be predicted [17], but a comprehensive study in p-GaAs would complete our understanding of recombination, emission, and absorption in GaAs.

InP and InGaAs are also important compound semiconductors in the fields of laser-optics and solar cells [Refs]. The recombination and absorption parameters of these materials are not well understood so a comprehensive study would provide much-needed understanding in rapidly growing fields.

6.2.2 Theoretical band-structure calculations

These results for absorption and emission make it appropriate to update models for quantum mechanical calculations of α and for B. Combined with recently reported data for the minority carrier mobility [65] and the intrinsic carrier concentration [66], the data are now available to develop and verify a complete band structure model for n-type GaAs. Studies combining α, PL, and bandgap narrowing have been done in n-type silicon [67, 68], but similar work in n-GaAs [69-71] have been incomplete without self-consistent absorption and emission data. A more complete analysis is now possible.

REFERENCES

REFERENCES

1. R. N. Hall, "Electron-Hole Recombination in Germanium," *Phys. Rev.*, vol. 87 (5), p. 387, 1 September 1952.
2. W. Shockley and W. T. Read, Jr., "Statistics of the Recombination of Holes and Electrons," *Phys. Rev.*, vol. 87 (5), p. 835, 1 September 1952.
3. R. N. Hall, "Recombination Processes in Semiconductors," *Proc. IEE*, vol. 106B, p. 923, March 1960.
4. H. C. Casey, Jr. and M. B. Panish, *Heterostructure Lasers,* Academic Press, New York, 1978.
5. W. van Roosbroeck and W. Shockley, "Photon-Radiative Recombination of Electrons and Holes in Germanium," *Phys. Rev.*, vol. 94 (6), p. 1558, 15 June 1954.
6. S. Wang, *Fundamentals of Semiconductor Theory and Device Physics,* p. 597, Prentice Hall, Englewood Cliffs, NJ, 1989.
7. C. J. Hwang, "Optical Properties of n-Type GaAs. I. Determination of Hole Diffusion Length from Optical Absorption and Photoluminescence Measurements," *J. Appl. Phys.*, vol. 40 (9), p. 3731, August 1969.
8. C. J. Hwang, "Doping Dependence of Hole Lifetime in n-type GaAs," *J. Appl. Phys.*, vol. 42 (11), p. 4408, October 1971.
9. C. J. Hwang, "Quantum Efficiency and Radiative Lifetime of the Band-to-Band Recombination in Heavily Doped n-type GaAs," *Phys. Rev. B*, vol. 6 (4), p. 1355, 15 August 1972.
10. H. C. Casey, Jr., D. D. Sell, and K. W. Wecht, "Concentration Dependence of the Absorption Coefficient for n-type and p-type GaAs Between 1.3 and 1.6 eV," *J. Appl. Phys.*, vol. 46 (1), p. 250, January 1975.
11. D. E. Hill, "Infrared Transmission and Fluorescence of Doped Gallium Arsenide," *Phys. Rev.*, vol. 133 (3A), p. A866, 3 February 1964.
12. H. C. Casey, Jr., B. I. Miller, and E. Pinkas, "Variation of Minority-Carrier Diffusion Length with Carrier Concentration in GaAs Liquid-Phase Epitaxial Layers," *J. Appl. Phys.*, vol. 44 (3), p. 1281, March 1973.
13. N. Puhlmann, G. Oelgart, V. Gottschalch, and R. Nemitz, "Minority Carrier recombination and internal quantum yield in GaAs:Sn by means of EBIC and CL," *Semiconductor Science and Technology,* vol. 6, p. 181, 1991.
14. D. Z. Garbuzov, *Semiconductor Optoelectronics,* pp. 305-343, Wiley, New York, 1980. Marian A. Herman (Ed.)

15. R. K. Ahrenkiel, D. J. Dunlavy, Brian Keyes, S. M. Vernon, T. M. Dixon, S. P. Tobin, K. L. Miller, and R. E. Hayes, "Ultralong Minority-carrier Lifetime in Epitaxial GaAs by Photon Recycling," *Appl. Phys. Letters*, vol. 55(11), p. 1088, 11 September 1989.

16. D. Z. Garbuzov, "Reemission, Quantum Efficiency and Lifetimes of Radiative Recombination in A_3B_5 Semiconductors and Heterostructures," *Semiconductor Physics*, pp. 53-86, Consultants Bureau, New York, 1986. Eds: M. M. Tuchkevich and V. Y. Frenkel

17. G. W. 't Hooft, C. Van Opdorp, H. Veenvliet, and A. T. Vink, "Minority Carrier Lifetime and Luminescence in MOVPE-grown (AlGa)As Epilayers and DH Lasers," *J. Cryst. Growth*, vol. 55, pp. 173-182, 1981.

18. D. J. Wolford, G. D. Gilliland, T. F. Kuech, L. M. Smith, J. Martinsen, J. A. Bradley, C. F. Tsang, R. Venkatasubramanian, S. K. Ghandi, and H. P. Hjalmarson, "Intrinsic recombination and interface characterization in "surface-free" GaAs structures," *J. Vac. Sci. Technol. B*, vol. 9 (4), p. 2369, Jul/Aug 1991.

19. J. M. Olson, R. K. Ahrenkiel, D. J. Dunlavy, Brian Keyes, and A. E. Kibbler, "Ultralow Recombination Velocity at $Ga_{0.5}In_{0.5}P/GaAs$ Heterointerfaces," *Appl. Phys. Lett.*, vol. 55 (12), p. 1208, 18 September 1989.

20. R. J. Nelson and R. G. Sobers, "Minority-carrier Lifetime and Internal Quantum Efficiency of Surface-free GaAs," *J. Appl. Phys.*, vol. 49 (12), p. 6103, December 1978.

21. Gordon Lasher and Frank Stern, "Spontaneous and Stimulated Recombination Radiation in Semiconductors," *Phys. Rev.*, vol. 133, No. 2A, p. A553, 20 January 1964.

22. P. Asbeck, "Self-absorption Effects on the Radiative Lifetime in GaAs-GaAlAs Double Heterostructures," *J. Appl. Phys.*, vol. 48 (2), p. 820, February 1977.

23. O. von Roos, "Influence of Radiative Recombination on the Minority-carrier transport in Direct Bandgap Semiconductors," *J. Appl. Phys.*, vol. 54 (3), p. 1390, March 1983.

24. Toshide Kuriyama, Takeshi Kamiya, and Hisayoshi Yanai, "Effect of Photon Recycling on Diffusion Length and Internal Quantum Efficiency in $Al_xGa_{1-x}As$—GaAs Heterostructures," *Jap. J. Appl. Phys.*, vol. 16 (3), p. 465, March 1977.

25. H. C. Casey, Jr. and Frank Stern, "Concentration-Dependent Absorption and Spontaneous Emission of Heavily Doped GaAs," *J. Appl. Phys.*, vol. 47 (2), p. 631, February 1976.

26. Masumi Takeshima, "Effect of Auger Recombination on Laser Operation in $Ga_{1-x}Al_xAs$," *J. Appl. Phys.*, vol. 58 (10), p. 3846, 15 November 1985.

27. A. Haug, "Auger Recombination in Direct-gap Semiconductors: Band-Structure Effects," *J. Phys C.*, vol. 16, pp. 4159-4172, 1983.

28. L. R. Weisberg, "Auger Recombination in GaAs," *J. Appl. Phys.*, vol. 39 (13), p. 6096, December 1968.

29. L. Jastrzebski, J. Lagowski, H. C. Gatos, and W. Walukiewicz, "Minority Carrier Lifetime in GaAs at Elevated Temperatures: Implications for Solar Cell Performance," *Gallium Arsenide and Related Compounds*, p. 437, Institute of Physics, London, 1979.
30. R.K. Ahrenkiel, *Solid State Electronics*, 1992. (Special Edition: Semiconductor Measurement Techniques. In press.)
31. R. J. Nelson, "Interfacial Recombination in GaAlAs-GaAs Heterostructures," *J. Vac. Sci. Technol.*, vol. 15 (4), p. 1475, July/Aug 1978.
32. A. Many, Y. Goldstein, and N. B. Grover, *Semiconductor Surfaces,* John Wiley and Sons, New York, 1965.
33. R. K. Ahrenkiel, D. J. Dunlavy, B. M. Keyes, S. M. Vernon, S. P. Tobin, and T. M. Dixon, "Design of High Efficiency Solar Cells By Photoluminescence Studies," *Conf. Rec., 21st IEEE Photovoltaic Specialists Conf.*, IEEE, New York, 1990.
34. H. F. MacMillan, H. C. Hamaker, N. R. Kaminar, M. S. Kuryla, M. Ladle Ristow, D. D. Liu, G. F. Virshup, and J. M. Gee, "28% Efficient GaAs Concentrator Solar Cells," *Conf. Rec., 20st IEEE Photovoltaic Specialists Conf.*, p. 462, IEEE, New York, 1988.
35. Eli Yablanovitch, T. Gmitter, J. P. Harbison, and R. Bhat, "Extreme Selectivity in the Lift-off of Epitaxial GaAs Films," *Appl. Phys. Lett.*, vol. 51 (26), p. 2222, 28 December 1987.
36. D. D. Sell and H. C. Casey, Jr., "Optical Absorption and Photoluminescence Studies of thin GaAs Layers in GaAs—$Al_xGa_{1-x}As$ Double Heterostructures," *J. Appl. Phys.*, vol. 45 (2), p. 800, February 1974.
37. R.Z. Bachrach, *Rev. Scientific Instruments*, vol. 43, p. 734, 1972.
38. R. K. Ahrenkiel, D. J. Dunlavy, and T. Hanak, "Minority-carrier lifetime in ITO/InP heterojunctions," *J. Appl. Phys.*, vol. 64 (4), p. 1916, 15 August 1988.
39. D. E. Aspnes, S. M. Kelso, R. A. Logan, and R. Bhat, "Optical Properties of $Al_xGa_{1-x}As$," *J. Appl. Phys.*, vol. 60, p. 754, 1986.
40. R. K. Ahrenkiel, B. M. Keyes, and D. J. Dunlavy, "Intensity-Dependent Minority-Carrier Lifetime in III-V Semiconductors Due To Saturation of Recombination Centers," *J. Appl. Phys.*, vol. 70 (1), p. 225, 1 July 1991.
41. R. K. Ahrenkiel, B. M. Keyes, G. B. Lush, M. R. Melloch, M. S. Lundstrom, and H. F. MacMillan, "Minority-Carrier Lifetime and Photon Recycling in N-GaAs," *J. Vac. Sci. Technol.*, July/August 1992. (In Press)
42. H. B. Bebb and E. W. Williams, *Photoluminescence I: Theory in Semiconductors and Semimetals,* 8, p. 219, Academic Press, New York, 1972.
43. G. B. Lush, H. F. MacMillan, B. M. Keyes, D. H. Levi, R. K. Ahrenkiel, M. R. Melloch, and M. S. Lundstrom, "A Study of Minority Carrier Lifetime versus Doping Concentration in N-type GaAs Grown by Metalorganic Chemical Vapor Deposition," *Submitted to J. of Appl. Phys.*, 1992.

44. M. Tong, D. Ballegeer, A. Ketterson, E.J. Roan, I. Adesida, and K.Y. Cheng, "A Comparative Study of Wet and Dry Selective Etching Processes for GaAs/AlGaAs/InGaAs Pseudomorphic MODFETs," *J. Electonic Mat.*, Jan 1992.
45. H. F. MacMillan, Personal Communication, 1991.
46. C. Juang, K. J. Kuhn, and R. B. Darling, "Selective etching of GaAs and $Al_{0.3}Ga_{0.7}As$ with citric acid/hydrogen peroxide solutions," *J. Vac. Sci. Technol. B*, vol. 8 (5), p. 1122, Sept/Oct 1990.
47. H. C. Casey, Jr., D. D. Sell, and M. B. Panish, "Refractive Index of $Al_xGa_{1-x}As$ between 1.2 and 1.8 eV," *Appl. Phys. Lett.*, vol. 24 (2), p. 63, 15 January 1974.
48. F. Urbach, *Phys. Rev.*, vol. 92, p. 1324, 1953.
49. J. S. Blakemore, "Semiconducting and other major properties of gallium arsenide," *J. Appl. Phys.*, vol. 53(10), p. R149, October 1982.
50. J. I. Pankove, "Absorption Edge of Impure Gallium Arsenide," *Phys. Rev.*, vol. 140 (6A), p. A2059, 1965.
51. E. Burstein, "Anomalous Optical Absorption Limit in InSb," *Phys. Rev.*, vol. 93, p. 632, 1954.
52. F. Stern, *Solid State Physics*, vol. 15, p. 300, Academic, New York, 1963. Ed: F. Seitz and D. Turnbull
53. M. D. Sturge, "Optical Absorption of Gallium Arsenide between 0.6 and 2.75 eV," *Phys. Rev.*, vol. 127 (3), p. 768, August 1, 1962.
54. D.A. Anderson, N. Apsley, P. Davies, and P.L. Giles, "Compensation in heavily doped n-type InP and GaAs," *J. Appl. Phys.*, vol. 58 (8), p. 3059, 15 Oct. 1985.
55. D.M. Szmyd, M.C. Hanna, and A. Majerfeld, "Heavily doped GaAs:Se. II. Electron mobility," *J. Appl. Phys.*, vol. 68 (5), p. 2376, 1 Sept. 1990.
56. Greg Lush and Mark Lundstrom, "Thin film approaches for high-efficiency III-V cells," *Solar Cells*, vol. 30, p. 337, 1991.
57. D. Z. Garbuzov, A. N. Ermakova, V. D. Rumyantsev, M. K. Trukan, and V. B. Khalfin, "Multipass Heterostructures. III. Effective Lifetime of Nonequilibrium Carriers," *Sov. Phys. Semicond.*, vol. 11 (4), p. 419, April 1977.
58. K. L. Miller, "Analysis of Transient Photoluminescence From $Al_xGa_{1-x}As/GaAs$ Double Heterostructure Samples," , M.S.E.E. Thesis, University of Colorado, at Boulder, 1989.
59. G. B. Lush, H. F. MacMillan, B. M. Keyes, R. K. Ahrenkiel, M. R. Melloch, and M. S. Lundstrom, "Determination of Minority Carrier Lifetimes in N-type GaAs and Their Implications for Solar Cells," *Conf. Rec., 22nd IEEE Photovoltaic Specialists Conf.*, IEEE, New York, 1991.
60. D. D. Sell, H. C. Casey, Jr., and K. W. Wecht, "Concentration dependence of the refractive index for n- and p-type GaAs between 1.2 and 1.8 eV," *J. Appl. Phys.*, vol. 45 (6), p. 2650, June 1974.

61. Frank Stern, "Calculated Spectral Dependence of Gain In Excited GaAs," *J. Appl. Phys.*, vol. 47 No. 12, p. 5382, December 1976.
62. E. Yablanovitch, T. J. Gmitter, and R. Bhat, "Inhibited and Enhanced Spontaneous Emission from Optically Thin AlGaAs/GaAs Double Heterostructures," *Phys. Rev. Lett.*, vol. 6 (22), p. 2546, 28 November 1988.
63. G. W. 't Hooft, "The radiative recombination coefficient of GaAs from laser delay measurements and effective nonradiative carrier lifetimes," *Appl. Phys. Lett.*, vol. 39 (5), p. 389, 1981.
64. M. P. Patkar, 1992. Private Communication.
65. M. L. Lovejoy, M. R. Melloch, B. M. Keyes, R. K. Ahrenkiel, and M. S. Lundstrom, "Minority Carrier Hole Mobility Measurements in n^+—GaAs," *18th International Symposium on Gallium Arsenide and Related Compounds*, Seattle Washington, USA, 1991.
66. M. P. Patkar, M. R. Melloch, and M. S. Lundstrom, *Appl. Phys. Lett.*, vol. 59 (15), Oct. 7 1991.
67. J. Wagner, "Heavily doped silicon studied by luminescence and selective absorption," *Solid-State Electronics*, vol. 28, p. 25, 1985.
68. S. T. Pantelides, A. Selloni, and R. Car, "Energy-gap reduction in heavily doped silicon: causes and consequences," *Solid-State Electronics*, vol. 28, p. 17, 1985.
69. H. S. Bennett and J. R. Lowney, "Models for Heavy Doping Effects in Gallium Arsenide," *J. Appl. Phys.*, vol. 62 (2), p. 521, July 1987.
70. S. C. Jain, J. M. McGregor, and D. J. Roulston, "Band-gap narrowing in novel III-V semiconductors," *J. Appl. Phys.*, vol. 68 (7), p. 3747, 1990.
71. B. E. Sernelius, "Band-gap shifts in heavily doped n-type GaAs," *Phys. Rev. B*, vol. 33 (12), p. 8582, 1986.

APPENDICES

Appendix A

The double heterostructures (DH's) were simulated using a finite difference solution to the one-dimensional diffusion equation,

$$\frac{\partial \Delta p}{\partial t} = G - R + D_p \frac{\partial^2 \Delta p}{\partial x^2}, \tag{A.1}$$

where Δp is the excess hole concentration, x is the position in the DH, t is time, and D_p is the hole diffusivity. The electron concentration, n, is defined as $N_D + \Delta p$. The recombination rate for the bulk is described by Eq. (1.1), and the generation rate, G, results from a combination of external excitation and photon recycling, G_{rec}. G_{rec} is described by Kuriyama, was expanded for up to three reflections by Miller, and has been extended further to allow any number of reflections in this work.

The recycling cofactor, ϕ_r, was computed by making all non-radiative recombination negligible and setting τ_r to some finite value. A laser pulse is simulated by a uniform initial distribution of holes. The "luminescence" is observed at the peak of the emission spectrum by

$$PL(t) = K\int_0^w \Delta p(x,t)n(x,t)e^{-\alpha_{peak}x}dx, \tag{A.2}$$

where K is a normalization factor and α_{peak} is the absorption coefficient at the peak of the PL spectra. The DH lifetime, τ_{DH}, is deduced from the rate of decay of PL(t). For these simulations with the non-radiative mechanisms turned off, $\tau_{DH} = \phi_r \tau_r$. By this method, ϕ_r was computed for all the DH's studied (except for those with $n_o = 2.4 \times 10^{18}$ cm^{-3} because of questions about α) and these are listed in Table A.1.

To obtain n(x) and p(x) for use in Eq. (5.2) to model steady-state photoluminescence, the bulk lifetime was set to the value of τ_{DH} found experimentally, and photon recycling was not used. Steady-state laser generation was simulated using Beer's Law exponential with the absorption coefficient of the incident photons chosen appropriately from Aspnes' data for a wavelength of 600 nanometers.

Table A.1 Computed values of ϕ_r for each of the DH samples. The targeted thicknesses are given in brackets for clarity.

n_o (cm^{-3})	[Targeted DH Thicknesses (μm)] Computed values of ϕ_r				
1.3×10^{17}	[0.25] 3.1	[1.25] 7.2	[2.5] 11.4	[5.0] 18.3	[10.] 28.9
3.7×10^{17}	[0.25] 2.8	[1.25] 5.9	[2.5] 9.1	[5.0] 14.3	[10.] 22.7
1.0×10^{18}	[0.5] 3.15	[1.0] 4.3	[2.0] 6.1	[4.0] 9.2	[8.] 14.6
2.2×10^{18}	[0.25] 2.3	[1.25] 4.2	[2.5] 5.8	[5.0] 8.5	[10.] 13.0
3.8×10^{18}	[0.25] 2.1	[0.5] 2.6	[1.25] 3.6	[2.5] 4.9	[10.] 10.3

Appendix B

Table B.1 Absorption coefficient versus electron concentration and photon energy or wavelength.

		Absorption Coefficient versus Electron Concentration				
λ (μm)	Energy (eV)	1.3×10^{17} (cm^{-1})	3.7×10^{17} (cm^{-1})	1.0×10^{18} (cm^{-1})	2.2×10^{18} (cm^{-1})	3.8×10^{18} (cm^{-1})
0.896	1.384	--	27.6	20.9	27.9	--
0.894	1.387	--	37.0	33.8	39.6	45.5
0.892	1.390	22.8	50.5	53.8	55.5	59.2
0.890	1.393	35.7	70.2	83.7	77.2	76.7
0.888	1.396	56.2	99.4	127.4	106.0	98.4
0.886	1.400	88.9	143.4	189.8	143.9	125.6
0.884	1.403	141.4	210.5	276.3	192.9	159.2
0.882	1.406	226.8	315.4	394.6	256.1	200.7
0.880	1.409	365.1	480.8	549.8	335.8	251.1
0.878	1.412	591.6	747.5	750.7	435.2	312.0
0.876	1.416	965.0	1185.1	1002.3	557.9	385.4
0.874	1.419	1579.8	1814.3	1306.8	705.7	472.4
0.872	1.422	2607.5	2785.9	1667.9	883.2	575.1
0.870	1.425	4326.1	3742.1	2080.2	1091.7	695.9
0.868	1.429	6257.9	4798.6	2534.0	1332.8	835.8
0.866	1.432	7788.4	5729.0	3019.8	1608.0	997.2
0.864	1.435	8650.6	6492.4	3514.8	1917.4	1181.0
0.862	1.439	9266.1	7210.4	3993.2	2256.9	1388.6
0.860	1.442	9736.3	7847.3	4433.3	2623.9	1621.7

Table B.1 (cont.)

		Absorption Coefficient versus Electron Concentration				
λ (μm)	Energy (eV)	1.3×10^{17} (cm^{-1})	3.7×10^{17} (cm^{-1})	1.0×10^{18} (cm^{-1})	2.2×10^{18} (cm^{-1})	3.8×10^{18} (cm^{-1})
0.858	1.445	10020.6	8303.2	4916.6	3013.0	1880.1
0.856	1.449	10333.0	8653.6	5303.1	3467.4	2163.7
0.854	1.452	10658.9	9042.8	5781.7	3926.2	2472.1
0.852	1.455	11020.6	9300.4	6285.6	4461.2	2805.4
0.850	1.459	11413.9	9574.6	6762.2	5030.4	3158.7
0.848	1.462	11745.1	9764.8	7298.4	5539.7	3528.6
0.846	1.466	12102.5	9981.5	7790.1	6083.6	3915.4
0.844	1.469	12490.6	10200.3	8198.8	6494.4	4310.4
0.842	1.473	12774.2	10431.0	8675.9	6902.1	4710.8
0.840	1.476	12930.8	10685.2	9013.8	7298.5	5050.1
0.838	1.480	13227.2	10944.2	9397.2	7643.6	5391.2
0.836	1.483	13400.7	11219.9	9804.8	8053.3	5800.0
0.834	1.487	13581.0	11527.3	10042.0	8383.0	6225.7
0.832	1.490	13768.8	11696.1	10476.2	8756.3	6656.4
0.830	1.494	13807.2	12026.7	10951.9	9209.2	7105.0
0.828	1.498	14004.8	12216.8	11468.9	9584.9	7562.4
0.826	1.501	14211.4	12591.7	11947.8	9837.9	8022.3
0.824	1.505	14427.8	12809.3	12449.8	10337.8	8490.9
0.822	1.509	14655.1	13038.5	12895.7	10790.5	8966.8
0.820	1.512	14919.0	13074.8	13366.6	11288.6	9453.4
0.818	1.516	14943.7	13318.9	13771.6	11655.1	9927.2
0.816	1.520	15225.4	13557.3	14181.0	12078.8	10413.0
0.814	1.523	15469.7	13619.0	14487.5	12513.1	10898.2
0.812	1.527	15757.4	13875.1	14810.4	12794.8	11367.5
0.810	1.531	15817.2	13941.5	15151.6	13298.7	11843.7
0.808	1.535	16096.5	14218.2	15375.1	13619.3	12312.1
0.806	1.538	16161.0	14266.0	15591.3	13938.8	12777.5
0.804	1.542	16462.9	14314.4	15832.0	14287.2	13223.2
0.802	1.546	16823.9	14617.0	16048.7	14670.3	13661.5

Table B.1 (cont.)

		Absorption Coefficient versus Electron Concentration				
λ (μm)	Energy (eV)	1.3×10^{17} (cm^{-1})	3.7×10^{17} (cm^{-1})	1.0×10^{18} (cm^{-1})	2.2×10^{18} (cm^{-1})	3.8×10^{18} (cm^{-1})
0.800	1.550	16861.6	14942.4	16134.0	15096.0	14098.4
0.798	1.554	16938.0	14999.1	16361.9	15145.4	14508.5
0.796	1.558	17298.6	15325.1	16598.8	15602.5	14922.0
0.794	1.562	17340.5	15387.1	16673.5	16094.8	15295.7
0.792	1.566	17382.7	15745.1	16903.5	16153.6	15678.8
0.790	1.570	17768.2	15779.2	17163.0	16207.8	16035.3
0.788	1.574	17819.3	15848.1	17391.7	16771.7	16372.4
0.786	1.578	18219.9	16210.5	17476.9	16816.2	16707.1
0.784	1.582	18276.4	16248.5	17718.0	16854.8	17021.1
0.782	1.586	18693.1	16325.4	17992.3	17500.8	17057.7
0.780	1.590	18755.9	16732.4	18230.9	17547.0	17401.6
0.778	1.594	18802.1	16775.2	18504.6	17593.7	17772.6
0.776	1.598	18854.6	16822.9	18791.3	17641.0	17815.6
0.774	1.602	19298.5	16862.3	19036.5	18391.7	18222.1
0.772	1.606	19350.5	17282.4	19120.4	18450.0	18283.8
0.770	1.610	19841.1	17331.1	19408.9	18489.3	18677.3
0.768	1.615	19885.1	17385.4	19712.0	18529.1	18729.5
0.766	1.619	19936.9	17840.6	19774.4	19437.6	19158.1
0.764	1.623	20465.8	17890.6	20063.8	19475.7	19210.2
0.762	1.627	20516.3	18387.1	20130.1	19488.5	19256.9
0.760	1.632	20567.4	18437.5	20197.0	19527.2	19719.4
0.758	1.636	21160.9	18482.1	20472.5	19566.2	19758.4
0.756	1.640	21200.1	19034.8	20543.3	19645.5	20261.2
0.754	1.645	21239.6	19078.7	20873.0	19685.8	20312.4
0.752	1.649	21279.5	19123.1	20910.7	20823.9	20848.7
0.750	1.653	21935.3	19152.9	21261.5	20860.4	20898.4
0.748	1.658	21981.8	19771.5	21549.2	20878.7	20948.5

Table B.1 (cont.)

λ (μm)	Energy (eV)	Absorption Coefficient versus Electron Concentration				
		1.3×10^{17} (cm^{-1})	3.7×10^{17} (cm^{-1})	1.0×10^{18} (cm^{-1})	2.2×10^{18} (cm^{-1})	3.8×10^{18} (cm^{-1})
0.746	1.662	22028.8	19814.9	21633.9	20934.3	20990.8
0.744	1.667	22757.1	19849.9	21940.2	20953.0	21596.4
0.742	1.671	22784.9	19876.4	22310.5	20990.7	21635.2
0.740	1.676	22826.9	20576.4	22310.4	21009.7	21664.5
0.738	1.680	22855.2	20607.7	22704.7	21048.0	21703.7
0.736	1.685	22883.6	20639.3	22704.7	22646.1	22370.4
0.734	1.689	23743.8	20692.4	23126.5	22675.4	22404.6
0.732	1.694	23901.4	21501.9	23126.5	22704.9	22439.1
0.730	1.699	23795.7	21540.8	23521.2	22704.9	22473.8
0.728	1.703	23830.7	21566.9	23579.8	22734.6	23228.1

Appendix C

Table C.1 Transmittance data versus wavelength for $n_o = 1.3 \times 10^{17}$ cm^{-3}.

Wavelength λ (μm)	Targeted Thicknesses 2.5 μm	5.0 μm	10 μm
0.700	0.00097	0.00071	0.00069
0.702	0.00098	0.00071	0.00069
0.704	0.00098	0.00071	0.00069
0.706	0.00099	0.00071	0.00069
0.708	0.00148	0.00071	0.00069
0.710	0.00149	0.00071	0.00069
0.712	0.00149	0.00071	0.00069
0.714	0.00150	0.00071	0.00069
0.716	0.00201	0.00071	0.00069
0.718	0.00202	0.00071	0.00069
0.720	0.00202	0.00071	0.00069
0.722	0.00204	0.00071	0.00069
0.724	0.00205	0.00071	0.00069
0.726	0.00206	0.00071	0.00069
0.728	0.00259	0.00071	0.00069
0.730	0.00261	0.00071	0.00069
0.732	0.00255	0.00071	0.00069
0.734	0.00264	0.00071	0.00069
0.736	0.00319	0.00071	0.00069
0.738	0.00321	0.00071	0.00069

Table C.1 (cont.)

Wavelength λ (μm)	Targeted Thicknesses 2.5 μm	5.0 μm	10 μm
0.740	0.00323	0.00071	0.00069
0.742	0.00326	0.00071	0.00069
0.744	0.00328	0.00071	0.00069
0.746	0.00385	0.00071	0.00069
0.748	0.00389	0.00071	0.00069
0.750	0.00393	0.00071	0.00069
0.752	0.00454	0.00071	0.00069
0.754	0.00458	0.00071	0.00069
0.756	0.00462	0.00071	0.00069
0.758	0.00466	0.00071	0.00069
0.760	0.00531	0.00071	0.00069
0.762	0.00537	0.00071	0.00069
0.764	0.00543	0.00071	0.00069
0.766	0.00610	0.00071	0.00069
0.768	0.00617	0.00071	0.00069
0.770	0.00623	0.00071	0.00069
0.772	0.00694	0.00071	0.00069
0.774	0.00702	0.00071	0.00069
0.776	0.00774	0.00071	0.00069
0.778	0.00783	0.00071	0.00069
0.780	0.00791	0.00071	0.00069
0.782	0.00802	0.00071	0.00069
0.784	0.00879	0.00071	0.00069
0.786	0.00890	0.00071	0.00069
0.788	0.00972	0.00071	0.00069
0.790	0.00983	0.00071	0.00069
0.792	0.01070	0.00071	0.00069
0.794	0.01080	0.00071	0.00069
0.796	0.01090	0.00071	0.00069
0.798	0.01180	0.00071	0.00069

Table C.1 (cont.)

Wavelength	Targeted Thicknesses		
λ (μm)	2.5 μm	5.0 μm	10 μm
0.800	0.01200	0.00071	0.00069
0.802	0.01210	0.00071	0.00069
0.804	0.01310	0.00071	0.00069
0.806	0.01400	0.00071	0.00069
0.808	0.01420	0.00071	0.00069
0.810	0.01510	0.00071	0.00069
0.812	0.01530	0.00071	0.00069
0.814	0.01630	0.00071	0.00069
0.816	0.01720	0.00071	0.00069
0.818	0.01830	0.00071	0.00069
0.820	0.01840	0.00071	0.00069
0.822	0.01950	0.00071	0.00069
0.824	0.02050	0.00071	0.00069
0.826	0.02150	0.00071	0.00069
0.828	0.02250	0.00071	0.00069
0.830	0.02350	0.00071	0.00069
0.832	0.02370	0.00071	0.00069
0.834	0.02470	0.00071	0.00069
0.836	0.02570	0.00071	0.00069
0.838	0.02670	0.00071	0.00069
0.840	0.02850	0.00071	0.00069
0.842	0.02950	0.00071	0.00069
0.844	0.03140	0.00071	0.00069
0.846	0.03420	0.00071	0.00069
0.848	0.03700	0.00143	0.00069
0.850	0.03980	0.00143	0.00069
0.852	0.04340	0.00214	0.00069
0.854	0.04700	0.00286	0.00069
0.856	0.05050	0.00357	0.00069
0.858	0.05410	0.00428	0.00139

Table C.1 (cont.)

Wavelength	Targeted Thicknesses		
λ (μm)	2.5 μm	5.0 μm	10 μm
0.860	0.05760	0.00499	0.00139
0.862	0.06210	0.00641	0.00138
0.864	0.06720	0.00855	0.00138
0.866	0.07870	0.01280	0.00207
0.868	0.10700	0.02620	0.00324
0.870	0.16000	0.06630	0.01170
0.872	0.20800	0.14900	0.04327
0.874	0.23800	0.21600	0.12140
0.876	0.26400	0.26300	0.22808
0.878	0.31200	0.38400	0.31604
0.880	0.40100	0.56200	0.38352
0.882	0.53900	0.63600	0.44014
0.884	0.70200	0.54800	0.46739
0.886	0.83000	0.40700	0.48100
0.888	0.86100	0.34400	0.49830
0.890	0.78100	0.38100	0.52375
0.892	0.65000	0.51200	0.52639
0.894	0.51500	0.66500	0.51859
0.896	0.41700	0.74000	0.52197
0.898	0.35000	0.67200	0.54087
0.900	0.31400	0.51100	0.54323
0.902	0.30100	0.36600	0.53202
0.904	0.30800	0.34700	0.52664
0.906	0.33700	0.40900	0.53725
0.908	0.38800	0.54800	0.55326
0.910	0.46400	0.69100	0.54345
0.912	0.57000	0.75400	0.53010
0.914	0.69900	0.69500	0.52953
0.916	0.82100	0.55800	0.54615
0.918	0.89600	0.42500	0.55727

Table C.1 (cont.)

Wavelength λ (μm)	Targeted Thicknesses 2.5 μm	5.0 μm	10 μm
0.920	0.87400	0.35300	0.53949
0.922	0.77400	0.35900	0.52920
0.924	0.65200	0.44500	0.53047
0.926	0.53200	0.57600	0.54657
0.928	0.44600	0.70700	0.56018
0.930	0.38700	0.76100	0.55081
0.932	0.34500	0.72300	0.53046
0.934	0.31900	0.60900	0.52588
0.936	0.30600	0.47300	0.53409
0.938	0.30600	0.38200	0.55632
0.940	0.31700	0.34500	0.56289
0.942	0.34300	0.37000	0.54403
0.944	0.39300	0.45700	0.52951
0.946	0.44500	0.58400	0.52704
0.948	0.52800	0.61200	0.54262
0.950	0.63200	0.76700	0.56489
0.952	0.75100	0.72900	0.56382
0.954	0.85500	0.60700	0.53959
0.956	0.90900	0.47300	0.52360
0.958	0.89400	0.37600	0.53078
0.960	0.81100	0.34300	0.55839
0.962	0.69600	0.36900	0.57249
0.964	0.58400	0.45000	0.55893
0.966	0.49500	0.57100	0.53398
0.968	0.42600	0.69500	0.52381
0.970	0.37500	0.76700	0.53043
0.972	0.34100	0.75600	0.55775
0.974	0.32100	0.66600	0.57524
0.976	0.31000	0.53800	0.55908
0.978	0.30900	0.42400	0.53491

Table C.1 (cont.)

Wavelength	Targeted Thicknesses		
λ (μm)	2.5 μm	5.0 μm	10 μm
0.980	0.32000	0.35900	0.52254
0.982	0.34100	0.34200	0.52725
0.984	0.37000	0.36900	0.54933
0.986	0.41400	0.43200	0.57322
0.988	0.47000	0.53700	0.57658
0.990	0.54600	0.65500	0.55585
0.992	0.63600	0.74900	0.52885
0.994	0.73800	0.78100	0.52057
0.996	0.86300	0.73700	0.53226
0.998	0.89700	0.62600	0.59325

Table C.2 Transmittance data versus wavelength for $n_o = 3.7 \times 10^{17}$ cm^{-3}.

Wavelength	Targeted Thicknesses		
λ (μm)	2.5 μm	5.0 μm	10 μm
0.700	0.00125	0.00060	0.00094
0.702	0.00125	0.00060	0.00094
0.704	0.00125	0.00061	0.00094
0.706	0.00188	0.00061	0.00094
0.708	0.00189	0.00061	0.00094
0.710	0.00189	0.00062	0.00094
0.712	0.00190	0.00062	0.00094
0.714	0.00254	0.00062	0.00094
0.716	0.00256	0.00062	0.00094
0.718	0.00257	0.00063	0.00094
0.720	0.00258	0.00063	0.00094
0.722	0.00259	0.00063	0.00094
0.724	0.00326	0.00064	0.00094
0.726	0.00328	0.00064	0.00094
0.728	0.00329	0.00065	0.00094
0.730	0.00331	0.00065	0.00094
0.732	0.00334	0.00065	0.00094
0.734	0.00403	0.00066	0.00094
0.736	0.00408	0.00066	0.00094
0.738	0.00411	0.00067	0.00094
0.740	0.00414	0.00067	0.00094
0.742	0.00487	0.00068	0.00094
0.744	0.00490	0.00068	0.00094
0.746	0.00494	0.00069	0.00094
0.748	0.00499	0.00070	0.00094
0.750	0.00576	0.00070	0.00094
0.752	0.00580	0.00071	0.00094
0.754	0.00586	0.00072	0.00094
0.756	0.00592	0.00072	0.00094
0.758	0.00673	0.00073	0.00094

Table C.2 (cont.)

Wavelength	Targeted Thicknesses		
λ (μm)	2.5 μm	5.0 μm	10 μm
0.760	0.00680	0.00074	0.00094
0.762	0.00688	0.00075	0.00094
0.764	0.00772	0.00075	0.00094
0.766	0.00781	0.00076	0.00094
0.768	0.00868	0.00077	0.00094
0.770	0.00879	0.00078	0.00094
0.772	0.00889	0.00079	0.00094
0.774	0.00980	0.00080	0.00094
0.776	0.00989	0.00081	0.00094
0.778	0.01000	0.00082	0.00094
0.780	0.01010	0.00083	0.00094
0.782	0.01110	0.00084	0.00094
0.784	0.01130	0.00085	0.00094
0.786	0.01140	0.00086	0.00094
0.788	0.01240	0.00087	0.00094
0.790	0.01260	0.00088	0.00094
0.792	0.01270	0.00089	0.00094
0.794	0.01380	0.00090	0.00094
0.796	0.01400	0.00091	0.00094
0.798	0.01510	0.00092	0.00094
0.800	0.01530	0.00094	0.00094
0.802	0.01650	0.00095	0.00094
0.804	0.01770	0.00096	0.00094
0.806	0.01790	0.00097	0.00095
0.808	0.01810	0.00098	0.00096
0.810	0.01930	0.00100	0.00097
0.812	0.01960	0.00101	0.00098
0.814	0.02080	0.00102	0.00099
0.816	0.02110	0.00103	0.00101
0.818	0.02230	0.00104	0.00102

Table C.2 (cont.)

Wavelength λ (μm)	Targeted Thicknesses 2.5 μm	 5.0 μm	 10 μm
0.820	0.02360	0.00105	0.00103
0.822	0.02380	0.00107	0.00104
0.824	0.02510	0.00108	0.00105
0.826	0.02640	0.00108	0.00105
0.828	0.02880	0.00109	0.00106
0.830	0.03010	0.00110	0.00107
0.832	0.03250	0.00111	0.00108
0.834	0.03380	0.00111	0.00108
0.836	0.03630	0.00112	0.00109
0.838	0.03870	0.00112	0.00109
0.840	0.04110	0.00113	0.00110
0.842	0.04360	0.00113	0.00110
0.844	0.04600	0.00113	0.00111
0.846	0.04840	0.00114	0.00111
0.848	0.05090	0.00114	0.00111
0.850	0.05320	0.00114	0.00111
0.852	0.05670	0.00114	0.00112
0.854	0.06020	0.00115	0.00112
0.856	0.06590	0.00115	0.00111
0.858	0.07150	0.00115	0.00111
0.860	0.07950	0.00115	0.00111
0.862	0.09220	0.00458	0.00111
0.864	0.10900	0.00914	0.00111
0.866	0.13600	0.01824	0.00222
0.868	0.18000	0.03417	0.00444
0.870	0.25200	0.06143	0.01330
0.872	0.36200	0.10454	0.03429
0.874	0.50400	0.17975	0.08177
0.876	0.58800	0.30909	0.15929
0.878	0.55000	0.41903	0.23407

Table C.2 (cont.)

Wavelength	Targeted Thicknesses		
λ (μm)	2.5 μm	5.0 μm	10 μm
0.880	0.45400	0.41196	0.31798
0.882	0.37300	0.34386	0.39869
0.884	0.32400	0.32770	0.41466
0.886	0.29900	0.42004	0.44031
0.888	0.29200	0.57930	0.50601
0.890	0.29900	0.67753	0.50762
0.892	0.32300	0.63371	0.47873
0.894	0.36900	0.49326	0.50709
0.896	0.44300	0.37191	0.55458
0.898	0.55400	0.35208	0.51913
0.900	0.71800	0.44769	0.49180
0.902	0.88900	0.61261	0.53888
0.904	0.98200	0.70960	0.56388
0.906	0.92800	0.67950	0.51762
0.908	0.78300	0.55215	0.49835
0.910	0.63200	0.41183	0.54545
0.912	0.51100	0.34629	0.56570
0.914	0.42500	0.37615	0.52121
0.916	0.36600	0.50116	0.49776
0.918	0.32700	0.64385	0.54063
0.920	0.30600	0.72112	0.56689
0.922	0.30000	0.68551	0.52908
0.924	0.30600	0.56702	0.50230
0.926	0.32400	0.44019	0.51740
0.928	0.35300	0.35542	0.56624
0.930	0.39600	0.34915	0.55844
0.932	0.45900	0.41472	0.51909
0.934	0.54500	0.54771	0.50302
0.936	0.65300	0.67459	0.52927
0.938	0.78500	0.72911	0.57003

Table C.2 (cont.)

Wavelength	Targeted Thicknesses		
λ (μm)	2.5 μm	5.0 μm	10 μm
0.940	0.91400	0.69103	0.55112
0.942	0.99200	0.57867	0.51641
0.944	0.96700	0.45575	0.50256
0.946	0.87000	0.36765	0.53299
0.948	0.73800	0.34193	0.57540
0.950	0.61500	0.38843	0.55140
0.952	0.51200	0.50698	0.51490
0.954	0.43700	0.65242	0.50484
0.956	0.37900	0.73150	0.55085
0.958	0.34000	0.71154	0.57493
0.960	0.31800	0.60633	0.54265
0.962	0.30700	0.48000	0.51274
0.964	0.30500	0.38148	0.50995
0.966	0.31200	0.33760	0.54914
0.968	0.32900	0.35458	0.57828
0.970	0.35400	0.43121	0.54486
0.972	0.39300	0.56873	0.51591
0.974	0.44600	0.69136	0.50687
0.976	0.52100	0.73913	0.54321
0.978	0.61700	0.70260	0.57609
0.980	0.72100	0.60115	0.55493
0.982	0.83600	0.48828	0.52772
0.984	0.93100	0.39437	0.50781
0.986	0.98200	0.34025	0.51411
0.988	0.97000	0.33547	0.55602
0.990	0.89200	0.38411	0.57602
0.992	0.79100	0.48747	0.54867
0.994	0.68000	0.61647	0.52523
0.996	0.57900	0.70702	0.50948
0.998	0.49600	0.73618	0.52941

Table C.3 Transmittance data versus wavelength for $n_o = 1.0 \times 10^{18}$ cm^{-3}.

Wavelength	Targeted Thicknesses		
λ (μm)	2.0 μm	4.0 μm	8. μm
0.700	0.00512	0.00207	0.00050
0.702	0.00514	0.00207	0.00050
0.704	0.00574	0.00207	0.00050
0.706	0.00633	0.00207	0.00050
0.708	0.00635	0.00207	0.00050
0.710	0.00696	0.00207	0.00050
0.712	0.00698	0.00207	0.00050
0.714	0.00761	0.00207	0.00050
0.716	0.00823	0.00207	0.00050
0.718	0.00827	0.00207	0.00050
0.720	0.00891	0.00207	0.00050
0.722	0.00894	0.00207	0.00050
0.724	0.00959	0.00207	0.00050
0.726	0.00966	0.00207	0.00050
0.728	0.01030	0.00207	0.00050
0.730	0.01040	0.00207	0.00050
0.732	0.01110	0.00207	0.00050
0.734	0.01110	0.00207	0.00050
0.736	0.01190	0.00207	0.00050
0.738	0.01190	0.00207	0.00050
0.740	0.01270	0.00207	0.00050
0.742	0.01270	0.00207	0.00050
0.744	0.01350	0.00207	0.00050
0.746	0.01420	0.00207	0.00050
0.748	0.01440	0.00207	0.00050
0.750	0.01510	0.00207	0.00050
0.752	0.01600	0.00207	0.00050
0.754	0.01610	0.00207	0.00050
0.756	0.01700	0.00207	0.00050
0.758	0.01720	0.00207	0.00050

Table C.3 (cont.)

Wavelength λ (μm)	Targeted Thicknesses 2.0 μm	 4.0 μm	 8. μm
0.760	0.01800	0.00207	0.00050
0.762	0.01820	0.00207	0.00050
0.764	0.01840	0.00207	0.00050
0.766	0.01930	0.00207	0.00050
0.768	0.01950	0.00207	0.00050
0.770	0.02050	0.00207	0.00050
0.772	0.02150	0.00207	0.00050
0.774	0.02180	0.00207	0.00050
0.776	0.02270	0.00207	0.00050
0.778	0.02380	0.00275	0.00050
0.780	0.02490	0.00275	0.00050
0.782	0.02590	0.00275	0.00050
0.784	0.02710	0.00275	0.00050
0.786	0.02820	0.00275	0.00050
0.788	0.02860	0.00275	0.00050
0.790	0.02970	0.00275	0.00050
0.792	0.03100	0.00275	0.00050
0.794	0.03220	0.00275	0.00050
0.796	0.03260	0.00349	0.00050
0.798	0.03390	0.00352	0.00050
0.800	0.03520	0.00358	0.00050
0.802	0.03570	0.00363	0.00050
0.804	0.03700	0.00368	0.00050
0.806	0.03850	0.00447	0.00050
0.808	0.03990	0.00453	0.00050
0.810	0.04140	0.00458	0.00050
0.812	0.04380	0.00542	0.00050
0.814	0.04620	0.00547	0.00050
0.816	0.04860	0.00631	0.00050
0.818	0.05200	0.00639	0.00050

Table C.3 (cont.)

Wavelength λ (μm)	Targeted Thicknesses 2.0 μm	 4.0 μm	 8. μm
0.820	0.05560	0.00725	0.00050
0.822	0.06010	0.00731	0.00050
0.824	0.06470	0.00818	0.00050
0.826	0.07030	0.00906	0.00050
0.828	0.07610	0.01080	0.00101
0.830	0.08290	0.01170	0.00102
0.832	0.08970	0.01270	0.00103
0.834	0.09640	0.01450	0.00103
0.836	0.10200	0.01630	0.00104
0.838	0.10800	0.01880	0.00156
0.840	0.11400	0.02150	0.00210
0.842	0.11900	0.02420	0.00264
0.844	0.12500	0.02860	0.00316
0.846	0.13000	0.03300	0.00370
0.848	0.13500	0.03920	0.00530
0.850	0.14200	0.04730	0.00743
0.852	0.14900	0.05590	0.01010
0.854	0.15800	0.06670	0.01380
0.856	0.17000	0.07890	0.01910
0.858	0.18600	0.09360	0.02660
0.860	0.20700	0.11200	0.03620
0.862	0.23700	0.13500	0.04950
0.864	0.27800	0.16500	0.06700
0.866	0.33200	0.20100	0.08930
0.868	0.41100	0.24100	0.11800
0.870	0.51600	0.28100	0.15700
0.872	0.62200	0.31000	0.20200
0.874	0.70800	0.32700	0.24900
0.876	0.73600	0.33900	0.29100
0.878	0.70100	0.36000	0.33200

Table C.3 (cont.)

Wavelength	Targeted Thicknesses		
λ (μm)	2.0 μm	4.0 μm	8. μm
0.880	0.62700	0.40400	0.37600
0.882	0.54300	0.46700	0.42400
0.884	0.46600	0.53000	0.46800
0.886	0.40700	0.57600	0.48400
0.888	0.36200	0.60200	0.48700
0.890	0.33400	0.59500	0.50100
0.892	0.31500	0.56300	0.51800
0.894	0.30600	0.51800	0.53900
0.896	0.30600	0.46900	0.55400
0.898	0.31400	0.43900	0.54100
0.900	0.33200	0.44400	0.52500
0.902	0.35900	0.48800	0.52800
0.904	0.40000	0.54900	0.53600
0.906	0.46200	0.60100	0.54800
0.908	0.54300	0.63200	0.55900
0.910	0.64200	0.63900	0.54700
0.912	0.75400	0.62600	0.52800
0.914	0.86400	0.59200	0.53200
0.916	0.95700	0.54800	0.54100
0.918	0.98300	0.49400	0.54800
0.920	0.94300	0.44800	0.55700
0.922	0.85900	0.42900	0.56000
0.924	0.75000	0.44700	0.54100
0.926	0.64400	0.49300	0.53000
0.928	0.55300	0.55000	0.53700
0.930	0.48300	0.59500	0.54400
0.932	0.42800	0.62900	0.54800
0.934	0.38700	0.64700	0.55500
0.936	0.35700	0.65000	0.55700
0.938	0.33500	0.63500	0.54700

Table C.3 (cont.)

Wavelength λ (μm)	Targeted Thicknesses 2.0 μm	4.0 μm	8. μm
0.940	0.32000	0.60700	0.53300
0.942	0.31000	0.56400	0.53000
0.944	0.30600	0.51400	0.54200
0.946	0.30800	0.46300	0.55000
0.948	0.31600	0.43000	0.55300
0.950	0.32900	0.42400	0.55900
0.952	0.35000	0.45000	0.55200
0.954	0.38100	0.50100	0.53600
0.956	0.42000	0.55600	0.52800
0.958	0.47000	0.60700	0.53900
0.960	0.53100	0.64100	0.55100
0.962	0.60800	0.65900	0.55600
0.964	0.69900	0.66000	0.55900
0.966	0.79500	0.64200	0.55700
0.968	0.88800	0.60800	0.54800
0.970	0.95800	0.56100	0.53000
0.972	0.98900	0.51000	0.53100
0.974	0.96700	0.45900	0.54400
0.976	0.90900	0.42600	0.55500
0.978	0.82900	0.41200	0.55800
0.980	0.74400	0.42800	0.56000
0.982	0.66100	0.46200	0.55700
0.984	0.58600	0.50800	0.55000
0.986	0.51700	0.56100	0.53900
0.988	0.46400	0.60900	0.52900
0.990	0.42000	0.64400	0.53700
0.992	0.38800	0.66300	0.55500
0.994	0.36300	0.67300	0.56500
0.996	0.34200	0.66200	0.56300
0.998	0.32500	0.63800	0.55700

Table C.4 Transmittance data versus wavelength for $n_o = 2.2 \times 10^{18}$ cm^{-3}.

Wavelength	Targeted Thicknesses		
λ (μm)	2.5 μm	5.0 μm	10 μm
0.700	0.00060	0.00303	0.00104
0.702	0.00060	0.00303	0.00104
0.704	0.00061	0.00303	0.00104
0.706	0.00061	0.00303	0.00104
0.708	0.00122	0.00303	0.00104
0.710	0.00123	0.00303	0.00104
0.712	0.00123	0.00303	0.00104
0.714	0.00124	0.00303	0.00104
0.716	0.00124	0.00303	0.00104
0.718	0.00125	0.00303	0.00104
0.720	0.00126	0.00303	0.00104
0.722	0.00126	0.00303	0.00104
0.724	0.00127	0.00303	0.00104
0.726	0.00128	0.00303	0.00104
0.728	0.00129	0.00253	0.00104
0.730	0.00130	0.00253	0.00104
0.732	0.00130	0.00253	0.00104
0.734	0.00131	0.00253	0.00104
0.736	0.00132	0.00253	0.00104
0.738	0.00200	0.00253	0.00104
0.740	0.00202	0.00253	0.00104
0.742	0.00203	0.00253	0.00104
0.744	0.00205	0.00253	0.00104
0.746	0.00206	0.00253	0.00104
0.748	0.00209	0.00253	0.00104
0.750	0.00210	0.00255	0.00104
0.752	0.00212	0.00258	0.00104
0.754	0.00285	0.00260	0.00104
0.756	0.00288	0.00263	0.00104
0.758	0.00294	0.00266	0.00104

Table C.4 (cont.)

Wavelength λ (μm)	Targeted Thicknesses 2.5 μm	 5.0 μm	 10 μm
0.760	0.00297	0.00268	0.00104
0.762	0.00300	0.00271	0.00104
0.764	0.00301	0.00274	0.00104
0.766	0.00304	0.00277	0.00104
0.768	0.00385	0.00280	0.00104
0.770	0.00389	0.00283	0.00104
0.772	0.00393	0.00287	0.00104
0.774	0.00399	0.00291	0.00104
0.776	0.00485	0.00294	0.00104
0.778	0.00491	0.00298	0.00104
0.780	0.00497	0.00301	0.00104
0.782	0.00503	0.00305	0.00104
0.784	0.00595	0.00309	0.00104
0.786	0.00601	0.00312	0.00104
0.788	0.00608	0.00316	0.00104
0.790	0.00704	0.00320	0.00104
0.792	0.00714	0.00324	0.00104
0.794	0.00725	0.00328	0.00104
0.796	0.00824	0.00332	0.00104
0.798	0.00928	0.00337	0.00104
0.800	0.00940	0.00342	0.00104
0.802	0.01050	0.00346	0.00104
0.804	0.01160	0.00351	0.00104
0.806	0.01270	0.00356	0.00104
0.808	0.01380	0.00359	0.00104
0.810	0.01500	0.00363	0.00104
0.812	0.01710	0.00368	0.00104
0.814	0.01840	0.00372	0.00104
0.816	0.02060	0.00376	0.00104
0.818	0.02300	0.00455	0.00104

Table C.4 (cont.)

Wavelength	Targeted Thicknesses		
λ (μm)	2.5 μm	5.0 μm	10 μm
0.820	0.02530	0.00461	0.00104
0.822	0.02880	0.00465	0.00104
0.824	0.03240	0.00547	0.00104
0.826	0.03690	0.00631	0.00104
0.828	0.04140	0.00636	0.00104
0.830	0.04820	0.00721	0.00104
0.832	0.05520	0.00886	0.00104
0.834	0.06350	0.01050	0.00104
0.836	0.07290	0.01220	0.00104
0.838	0.08110	0.01470	0.00156
0.840	0.08920	0.01720	0.00158
0.842	0.09640	0.02060	0.00211
0.844	0.10300	0.02480	0.00264
0.846	0.11100	0.02990	0.00371
0.848	0.12400	0.03830	0.00531
0.850	0.14300	0.04830	0.00797
0.852	0.17100	0.06260	0.01170
0.854	0.21500	0.07680	0.01760
0.856	0.27100	0.08930	0.02550
0.858	0.33400	0.10000	0.03570
0.860	0.37400	0.11800	0.04880
0.862	0.37500	0.14900	0.06570
0.864	0.34300	0.19600	0.08780
0.866	0.30400	0.24400	0.11300
0.868	0.27600	0.26600	0.14200
0.870	0.26300	0.25000	0.17900
0.872	0.26900	0.23000	0.22100
0.874	0.29900	0.24800	0.25300
0.876	0.36200	0.32800	0.28600
0.878	0.46600	0.45200	0.33200

Table C.4 (cont.)

Wavelength	Targeted Thicknesses		
λ (μm)	2.5 μm	5.0 μm	10 μm
0.880	0.61100	0.54400	0.37300
0.882	0.76500	0.53200	0.38700
0.884	0.83900	0.43700	0.40600
0.886	0.80900	0.33800	0.44800
0.888	0.68600	0.29800	0.48400
0.890	0.54700	0.33100	0.47300
0.892	0.43200	0.44800	0.47000
0.894	0.35800	0.61300	0.50400
0.896	0.31600	0.69600	0.53400
0.898	0.30000	0.63600	0.51200
0.900	0.30800	0.47800	0.48900
0.902	0.34000	0.35200	0.51300
0.904	0.40500	0.30800	0.55000
0.906	0.50600	0.34100	0.53400
0.908	0.64800	0.45700	0.49400
0.910	0.79800	0.61900	0.50900
0.912	0.90100	0.71700	0.55000
0.914	0.89100	0.67700	0.55400
0.916	0.78200	0.53700	0.51100
0.918	0.62300	0.39100	0.49400
0.920	0.49000	0.31800	0.53000
0.922	0.40400	0.31500	0.56500
0.924	0.34700	0.37200	0.54900
0.926	0.31500	0.49700	0.50000
0.928	0.30300	0.64400	0.49700
0.930	0.30500	0.72500	0.53800
0.932	0.32100	0.69900	0.56900
0.934	0.35800	0.57900	0.54800
0.936	0.41600	0.44300	0.50000
0.938	0.50600	0.34800	0.48900

Table C.4 (cont.)

Wavelength	Targeted Thicknesses		
λ (μm)	2.5 μm	5.0 μm	10 μm
0.940	0.62300	0.31100	0.52800
0.942	0.75400	0.32500	0.56700
0.944	0.87000	0.38800	0.56800
0.946	0.92000	0.50700	0.51900
0.948	0.88200	0.65200	0.48500
0.950	0.77400	0.73800	0.52200
0.952	0.63400	0.70200	0.56900
0.954	0.51400	0.57300	0.57300
0.956	0.41900	0.42900	0.52000
0.958	0.35700	0.34100	0.48300
0.960	0.32500	0.31200	0.51700
0.962	0.30700	0.33200	0.56500
0.964	0.30500	0.40100	0.58400
0.966	0.31400	0.52100	0.54100
0.968	0.33700	0.66000	0.48500
0.970	0.38000	0.74500	0.49500
0.972	0.44500	0.71900	0.54900
0.974	0.53500	0.60500	0.58300
0.976	0.65800	0.46500	0.56600
0.978	0.78100	0.36800	0.50900
0.980	0.88500	0.32400	0.47400
0.982	0.92400	0.31600	0.50300
0.984	0.90100	0.34400	0.55800
0.986	0.82700	0.41100	0.59100
0.988	0.71300	0.52500	0.57500
0.990	0.60000	0.65900	0.51700
0.992	0.50200	0.74800	0.47400
0.994	0.42600	0.74800	0.50500
0.996	0.36800	0.66100	0.56000
0.998	0.33500	0.53000	0.59300

Table C.5 Transmittance data versus wavelength for $n_o = 2.4 \times 10^{18}$ cm^{-3}.

Wavelength λ (μm)	Targeted Thicknesses 2.5 μm	10 μm
0.700	0.00150	0.00064
0.702	0.00200	0.00064
0.704	0.00200	0.00064
0.706	0.00200	0.00064
0.708	0.00200	0.00064
0.710	0.00200	0.00064
0.712	0.00200	0.00064
0.714	0.00250	0.00064
0.716	0.00250	0.00064
0.718	0.00250	0.00064
0.720	0.00251	0.00064
0.722	0.00252	0.00064
0.724	0.00254	0.00064
0.726	0.00306	0.00064
0.728	0.00308	0.00064
0.730	0.00310	0.00064
0.732	0.00312	0.00064
0.734	0.00313	0.00064
0.736	0.00369	0.00064
0.738	0.00371	0.00064
0.740	0.00374	0.00064
0.742	0.00377	0.00064
0.744	0.00380	0.00064
0.746	0.00437	0.00064
0.748	0.00441	0.00064
0.750	0.00445	0.00064
0.752	0.00449	0.00064
0.754	0.00511	0.00064
0.756	0.00516	0.00064
0.758	0.00522	0.00064

Table C.5 (cont.)

Wavelength λ (μm)	Targeted Thicknesses 2.5 μm	10 μm
0.760	0.00585	0.00064
0.762	0.00592	0.00064
0.764	0.00657	0.00064
0.766	0.00665	0.00064
0.768	0.00672	0.00064
0.770	0.00740	0.00064
0.772	0.00750	0.00064
0.774	0.00823	0.00064
0.776	0.00832	0.00064
0.778	0.00908	0.00064
0.780	0.00919	0.00064
0.782	0.00996	0.00064
0.784	0.01010	0.00064
0.786	0.01090	0.00064
0.788	0.01170	0.00064
0.790	0.01250	0.00064
0.792	0.01340	0.00064
0.794	0.01430	0.00064
0.796	0.01450	0.00064
0.798	0.01610	0.00064
0.800	0.01710	0.00064
0.802	0.01810	0.00064
0.804	0.01980	0.00064
0.806	0.02160	0.00064
0.808	0.02340	0.00064
0.810	0.02530	0.00064
0.812	0.02800	0.00064
0.814	0.03160	0.00064
0.816	0.03600	0.00064
0.818	0.04060	0.00064

Table C.5 (cont.)

Wavelength	Targeted Thicknesses	
λ (μm)	2.5 μm	10 μm
0.820	0.04510	0.00064
0.822	0.05070	0.00065
0.824	0.05620	0.00065
0.826	0.06190	0.00132
0.828	0.06760	0.00133
0.830	0.07320	0.00134
0.832	0.07890	0.00202
0.834	0.08480	0.00272
0.836	0.09240	0.00341
0.838	0.10200	0.00480
0.840	0.11500	0.00759
0.842	0.13100	0.01039
0.844	0.15400	0.01391
0.846	0.18600	0.02025
0.848	0.22800	0.02729
0.850	0.27300	0.03564
0.852	0.30800	0.05060
0.854	0.31900	0.07073
0.856	0.30500	0.08473
0.858	0.28000	0.10014
0.860	0.25700	0.14356
0.862	0.24200	0.18628
0.864	0.24000	0.17622
0.866	0.25000	0.18423
0.868	0.27900	0.27964
0.870	0.33200	0.36490
0.872	0.42000	0.28144
0.874	0.54600	0.25312
0.876	0.68300	0.40777
0.878	0.78700	0.57400

Table C.5 (cont.)

Wavelength λ (μm)	Targeted Thicknesses 2.5 μm	 10 μm
0.880	0.80300	0.39517
0.882	0.73000	0.28926
0.884	0.61100	0.38583
0.886	0.49600	0.67308
0.888	0.40600	0.66324
0.890	0.34600	0.38383
0.892	0.30900	0.31391
0.894	0.29100	0.50343
0.896	0.29200	0.80041
0.898	0.30800	0.56593
0.900	0.34200	0.32898
0.902	0.39900	0.35994
0.904	0.48800	0.66345
0.906	0.61600	0.79945
0.908	0.76300	0.47920
0.910	0.88300	0.31667
0.912	0.91800	0.38842
0.914	0.85100	0.69958
0.916	0.72600	0.79507
0.918	0.59100	0.47829
0.920	0.48100	0.31838
0.922	0.40300	0.37904
0.924	0.35000	0.66908
0.926	0.31700	0.83479
0.928	0.30100	0.55720
0.930	0.29600	0.34199
0.932	0.30300	0.32432
0.934	0.32000	0.48558
0.936	0.35000	0.79339
0.938	0.39800	0.77054

Table C.5 (cont.)

Wavelength λ (μm)	Targeted Thicknesses 2.5 μm	10 μm
0.940	0.46500	0.45490
0.942	0.55500	0.31952
0.944	0.66700	0.35507
0.946	0.79000	0.57143
0.948	0.89400	0.84367
0.950	0.93100	0.67785
0.952	0.88600	0.39676
0.954	0.77900	0.31506
0.956	0.65100	0.40973
0.958	0.53700	0.71159
0.960	0.45500	0.83824
0.962	0.39300	0.54690
0.964	0.35000	0.34833
0.966	0.32200	0.31831
0.968	0.30600	0.42700
0.970	0.30000	0.70757
0.972	0.30600	0.84382
0.974	0.32000	0.57204
0.976	0.34700	0.35991
0.978	0.38400	0.31818
0.980	0.43600	0.41211
0.982	0.50000	0.64397
0.984	0.58800	0.86135
0.986	0.68900	0.71159
0.988	0.79700	0.44948
0.990	0.89000	0.32708
0.992	0.94000	0.33011
0.994	0.92500	0.47151
0.996	0.85600	0.73894
0.998	0.76900	0.84839

Table C.6 Transmittance data versus wavelength for $n_o = 3.8 \times 10^{18}$ cm^{-3}.

Wavelength λ (μm)	Targeted Thicknesses 2.5 μm	10 μm
0.700	0.00216	0.00100
0.702	0.00217	0.00100
0.704	0.00218	0.00100
0.706	0.00219	0.00100
0.708	0.00220	0.00100
0.710	0.00275	0.00100
0.712	0.00277	0.00100
0.714	0.00278	0.00100
0.716	0.00279	0.00100
0.718	0.00280	0.00100
0.720	0.00338	0.00100
0.722	0.00341	0.00100
0.724	0.00342	0.00100
0.726	0.00344	0.00100
0.728	0.00346	0.00100
0.730	0.00406	0.00100
0.732	0.00409	0.00100
0.734	0.00412	0.00100
0.736	0.00415	0.00100
0.738	0.00478	0.00100
0.740	0.00482	0.00100
0.742	0.00485	0.00100
0.744	0.00489	0.00100
0.746	0.00556	0.00100
0.748	0.00561	0.00100
0.750	0.00567	0.00100
0.752	0.00573	0.00100
0.754	0.00642	0.00100
0.756	0.00649	0.00100
0.758	0.00722	0.00100

Table C.6 (cont.)

Wavelength λ (μm)	Targeted Thicknesses 2.5 μm	 10 μm
0.760	0.00728	0.00100
0.762	0.00803	0.00100
0.764	0.00811	0.00100
0.766	0.00820	0.00100
0.768	0.00898	0.00100
0.770	0.00908	0.00100
0.772	0.00987	0.00100
0.774	0.01000	0.00100
0.776	0.01090	0.00100
0.778	0.01100	0.00100
0.780	0.01190	0.00100
0.782	0.01280	0.00100
0.784	0.01290	0.00100
0.786	0.01380	0.00100
0.788	0.01480	0.00100
0.790	0.01580	0.00100
0.792	0.01680	0.00100
0.794	0.01780	0.00100
0.796	0.01960	0.00100
0.798	0.02070	0.00100
0.800	0.02270	0.00100
0.802	0.02470	0.00100
0.804	0.02680	0.00100
0.806	0.02890	0.00100
0.808	0.03100	0.00100
0.810	0.03400	0.00100
0.812	0.03720	0.00100
0.814	0.04120	0.00100
0.816	0.04550	0.00100
0.818	0.05150	0.00100

Table C.6 (cont.)

Wavelength λ (μm)	Targeted Thicknesses 2.5 μm	 10 μm
0.820	0.05870	0.00100
0.822	0.06690	0.00100
0.824	0.07610	0.00100
0.826	0.08630	0.00100
0.828	0.09880	0.00100
0.830	0.11100	0.00100
0.832	0.12100	0.00150
0.834	0.13000	0.00200
0.836	0.13800	0.00250
0.838	0.14300	0.00402
0.840	0.14800	0.00556
0.842	0.15300	0.00761
0.844	0.16300	0.01070
0.846	0.17800	0.01530
0.848	0.20300	0.02150
0.850	0.24000	0.03070
0.852	0.29600	0.04210
0.854	0.36900	0.05750
0.856	0.44700	0.07650
0.858	0.49600	0.09550
0.860	0.49800	0.11800
0.862	0.45500	0.14600
0.864	0.39700	0.17600
0.866	0.34600	0.19800
0.868	0.30900	0.22900
0.870	0.29500	0.27400
0.872	0.28800	0.30100
0.874	0.30300	0.31400
0.876	0.33400	0.35300
0.878	0.38300	0.40000

Table C.6 (cont.)

Wavelength λ (μm)	Targeted Thicknesses 2.5 μm	 10 μm
0.880	0.45600	0.41000
0.882	0.55600	0.40100
0.884	0.67600	0.43000
0.886	0.79600	0.48200
0.888	0.86700	0.49100
0.890	0.84900	0.45700
0.892	0.74900	0.46700
0.894	0.61700	0.52300
0.896	0.50100	0.53900
0.898	0.41800	0.49200
0.900	0.36100	0.47600
0.902	0.32900	0.52300
0.904	0.31500	0.55900
0.906	0.31400	0.51500
0.908	0.32700	0.47700
0.910	0.35500	0.51500
0.912	0.40100	0.56600
0.914	0.46700	0.54600
0.916	0.55800	0.48800
0.918	0.67500	0.48500
0.920	0.79800	0.54200
0.922	0.88500	0.57400
0.924	0.90400	0.53200
0.926	0.84500	0.47800
0.928	0.74100	0.49500
0.930	0.62500	0.55400
0.932	0.52400	0.57800
0.934	0.44400	0.53400
0.936	0.39000	0.48000
0.938	0.35300	0.48300

Table C.6 (cont.)

Wavelength λ (μm)	Targeted Thicknesses 2.5 μm	10 μm
0.940	0.33000	0.53900
0.942	0.31600	0.58100
0.944	0.31400	0.55800
0.946	0.32000	0.49400
0.948	0.33700	0.47500
0.950	0.36600	0.52700
0.952	0.41100	0.58400
0.954	0.47300	0.56800
0.956	0.55600	0.49600
0.958	0.66000	0.47100
0.960	0.76900	0.51900
0.962	0.85700	0.57800
0.964	0.90600	0.58300
0.966	0.89800	0.53400
0.968	0.83000	0.46800
0.970	0.72200	0.49200
0.972	0.60900	0.56000
0.974	0.51700	0.59500
0.976	0.44600	0.55400
0.978	0.39500	0.48600
0.980	0.36400	0.46600
0.982	0.33900	0.50500
0.984	0.32600	0.56900
0.986	0.31900	0.59900
0.988	0.31900	0.56500
0.990	0.32700	0.49000
0.992	0.34100	0.46400
0.994	0.36600	0.50500
0.996	0.39800	0.57200
0.998	0.44200	0.60400

Document Control Page	1. NREL Report No. NREL/TP-451-5355	2. NTIS Accession No. DE93000097	3. Recipient's Accession No.

4. Title and Subtitle

New III-V Cell Design Approaches for Very High Efficiency

5. Publication Date

April 1993

6.

7. Author(s)

M.S. Lundstrom, M.R. Melloch, G.B. Lush, M.P. Patkar, M.P. Young

8. Performing Organization Rept. No.

9. Performing Organization Name and Address

Purdue University
School of Electrical Engineering
1285 Electrical Engineering Building
West Lafayette, Indiana 47907

10. Project/Task/Work Unit No.
PV321101

11. Contract (C) or Grant (G) No.

(C) XM-0-19142-1

(G)

12. Sponsoring Organization Name and Address
National Renewable Energy Laboratory
1617 Cole Blvd.
Golden, CO 80401-3393

13. Type of Report & Period Covered

Technical Report
1 August 1991 - 31 July 1992

14.

15. Supplementary Notes
NREL technical monitor: J. Benner

16. Abstract (Limit: 200 words)

This report describes research to examine new solar cell design approaches for achieving very high conversion efficiencies. The program consists of two elements. The first centers on exploring new thin-film approaches specifically designed for III-V semiconductors. Substantial efficiency gains may be possible by employing light trapping techniques to confine the incident photons, as well as the photons emitted by radiative recombination. The thin-film approach is a promising route for achieving substantial performance improvements in the already high-efficiency, single-junction, III-V cell. The second element of the research involves exploring design approaches for achieving high conversion efficiencies without requiring extremely high-quality material. This work has applications to multiple-junction cells, for which the selection of a component cell often involves a compromise between optimum band gap and optimum material quality. It could also be a benefit in a manufacturing environment by making the cell's efficiency less dependent on material quality.

17. Document Analysis
a. Descriptors
photovoltaics ; solar cells

b. Identifiers/Open-Ended Terms

c. UC Categories
270

18. Availability Statement
National Technical Information Service
U.S. Department of Commerce
5285 Port Royal Road
Springfield, VA 22161

19. No. of Pages

124

20. Price

A06

Form No. 0069E (6-30-87)